Multilayer Flat Optics

By

You Zhou

Dissertation
Submitted to the Faculty of the
Graduate School of Vanderbilt University
in partial fulfillment of the requirements
for the degree of

DOCTOR OF PHILOSOPHY
in

Interdisciplinary Materials Science
August, 7, 2020
Nashville, Tennessee

Approved:

Jason G. Valentine, Ph.D.

Josh Caldwell, Ph.D.

Sharon M. Weiss, Ph.D.

Richard F. Haglund Jr., Ph.D.

Justus Ndukaife, Ph.D.

To my beloved mom and dad.

ACKNOWLEDGEMENTS

Vanderbilt has been a special place for me as it provides me with everything one can ever ask for an ideal graduate experience. Looking back on the past five years of fun and hard work, my journey towards the Ph.D. degree has probably been the most rewarding part of my life. I'm grateful for the academic freedom and healthy work-life balance, but more importantly, the unwavering support from many people.

First and foremost, I want to express my deepest gratitude to my advisor Prof. Jason Valentine. Prof. Valentine offered me the opportunity to come to Vanderbilt, and since then I'm fortunate to conduct research not only with a great mentor but also a visionary scientist. Coming from an optics background with little experimental experience, Prof. Valentine placed me with great trust and patiently guided me into the word of nanophotonics, helping me develop not only my technical skills but also the attitude as an experimentalist. Prof. Valentine has always been open to new ideas, and I benefit greatly from our individual meeting where I can learn directly from his critical thinking and scientific approach for tackling frontier challenges. It is his insightful and constructive suggestions during many of the discussions that eventually lead to the projects presented in this thesis. Beyond my research, Prof. Valentine is also extremely supportive in my academic career. He sends me to numerous major conferences, which allows me to interact with peers and establish a network in a broader optics community. Prof. Valentine's mentorship and support is the most important reason for the continuation of my academic endeavor. I have learnt a lot from him both scientifically and personally, and for this I express my tremendous gratitude.

I would also like to thank Prof. Josh Caldwell, Prof. Sharon Weiss, Prof. Richard Haglund and Prof. Justus Ndukaife for not only serving on my committee, but also the valuable feedback

on my research and soft skills, which help steer my graduate development in the right direction. I have also learned a lot from their classes, not only the knowledges that are extremely helpful for my research, but also the friendly atmosphere where I could freely interact with my classmates. Some of them turn out to be long-term buddies throughout my graduate school. I would also like to thank Prof. Caldwell and Prof. Weiss for their generous help and support on my career development.

I also want to thank all my labmates in Prof. Valentine's group, both past and present. The great atmosphere of comfort, friendship and mutual encouragement have made my experience not only productive, but also fun. In particular, I would like to thank Dr. Yuanmu Yang and Dr. Wei Li, whose success have always stood out as the role models that motivate and guide me through difficult times. Special thanks to Dr. Zack Coppens for helping me out both inside and outside labs. The times we work, discuss and hang out together have always been the most valuable memories. Special thanks to Chibuzor Fabian Ugwu and Austin Howes for the continuous encouragement. The moments we chat and joke have made the office hours full of happiness. I also like to thank Hanyu Zheng. We have worked together on many great projects and successfully got through many critical times of program review. It is his extreme of hard work that enables us to tackle frontier challenges and open new possible areas.

I would also like to thank Myrtle Daniels, Jean Miller and Chris Lindsey for their exceptional administrative support, ranging from placing purchase orders to filling online forms. Special thanks to Kurt Heinrich, Alice Leach, Anthony Hmelo, William Martinez and Dmitry Koktysh at Vinse for their training and assistance with all kinds of tools in the cleanroom. Furthermore, I would like to thank all the other external collaborators who work together on various projects during my Ph.D. This includes but not limited to Ivan Kravchenko, Hao Wang,

Prof. Gong Gu, Prof. Anthony Grbic, Brian Raeker, and Brian Slovick. Special thanks to Ivan Kravchenko for constantly providing tremendous help for our group and kindly hosting me during my CNMS trips. Special thanks to Dr. Hao Wang and Prof. Gong Gu for providing the systems that are critical to my projects.

Furthermore, I want to thank to all the friends made in Nashville. Special thanks to Jirong Long and Mingrong You's family for always making me feel at home in Nashville. Specially thanks to Jiawei Han for being an almost perfect roommate. I also want to thank Tengfei Cao, Hengqing Wang, Andrew Westover, Haozhu Wang, Lin Yang, Xin Zhang and Francis Afzal, for bringing unforgettable happy moments in my graduate school life.

Apart from the people at Vanderbilt, I would like to thank my undergraduate advisor Prof. Jianwen Dong and his senior graduate students Dr. Xiaodong Chen and Dr. Xintao He, who introduced me into the world of nanophotonics and metamaterials, and patiently guided me through when I barely knew anything about research. This period of training turned out to be extremely helpful in my later years of graduate development.

Finally, I wish to express my deepest gratitude to my family and girlfriend for their unconditional love, support and encouragement. Thanks for sending me to the US and allowing me to pursue my dreams. To my mom, thanks for standing behind and constantly offering me comfort and encouragement. To my dad, your success has always been my role model and I wish you feel proud of your son's efforts to go that far.

TABLE OF CONTENTS

Page

LIST OF FIGURES

Figure Page

LIST OF ABBREVIATIONS

Al_2O_3	Aluminum Oxide
BIC	Bound state in the continuum
CCD	Charge-coupled Device
CMOS	Complementary Metal Oxide Semiconductor
CNN	Convolution Neural Network
DUV	Deep Ultraviolet
EBL	Electron Beam Lithography
FDTD	Finite Difference Time Domain
FOV	Field of View
FOM	Figure of Merit
FWHM	Full Width at Half Maximum
Ge	Germanium
GS	Gerchberg-Saxton
GaP	Gallium Phosphide
HCTAs	High-contrast Transmit Arrays
IPA	Isopropyl Alcohol
LPCVD	Low Pressure Chemical Vapor Deposition
MEMS	Micro-electromechanical system
MIBK	Methyl Isobutyl Ketone
NA	Numerical Aperture
OCT	Optical Coherence Tomography
PB	Pancharatnam-Berry
PECVD	Plasma Enhanced Chemical Vapor Deposition
PDMS	Poly(dimethylsiloxane)

PMMA	Poly(Methyl Methacrylate)
Q-factor	Quality Factor
RIE	Reactive Ion Etching
Si	Silicon
SiO_2	Silicon Dioxide
Si_3N_4	Silicon Nitride
SLM	Spatial Light Modulator
SRRs	Split-ring Resonators
TiO_2	Titanium Oxide
TE	Transverse Electric
TM	Transverse Magnetic
VINSE	Vanderbilt Institute of Nanoscale Science and Engineering

LIST OF PUBLICATIONS

Parts of this dissertation have been drawn from the following publications:

1. **Y. Zhou**, H. Zheng, I. Kracvhcenko, J. Valentine. "Flat Optics for Image Differentiation", ***Nature Photonics,*** 1-8, 14 (2020).

2. **Y. Zhou**, I. Kracvhcenko, H. Wang, H. Zheng, G. Gu, J. Valentine. "Multilayer Noninteracting Dielectric Metasurfaces for Multiwavelength Metaoptics", ***Light: Science & Applications***, 8, 80 (2019).

3. **Y. Zhou**, I. Kracvhcenko, H. Wang, J. Ryan Nolen, G. Gu, J. Valentine. "Multilayer Noninteracting Dielectric Metasurfaces for Multiwavelength Metaoptics", ***Nano Letters***, 18, 7529 (2018).

4. B. Slovick, **Y. Zhou**, Z. Yu, I. Kravchenckou, D. Briggs, P. Moitra, S. Krishnamurthy, J. Valentine. "Metasurface polarization splitter", ***Philos. Trans. R. Soc. A***, 2090, 20160072 (2017).

Chapter 1

Introduction

1.1 What is metasurface?

The control of phase, amplitude, and polarization enables complete shaping of monochromatic light. In free-space optics, conventional devices including lenses, prisms, and polarization-sensitive elements are readily available to modulate various optical properties with high performance. However, the bulky form factor and fabrication constraints limit their functionality and compatibility with integration into electronics. With an increasing demand for high-performance portable and wearable optoelectronic devices, planar optics have become promising due to their broad functionality and ease of integration in compact systems.

Recently, optical metasurfaces have emerged as an attractive platform for manipulating the wavefront of light through a thin layer of flat optics. A metasurface is a type of planar optical element made of nanostructured building blocks. The design of size, shape, and orientation of each building block provides great flexibility to locally engineer the properties of light with high resolution in an ultrathin form factor. In order to create the composite of the building blocks that are free of unwanted diffractive orders, the unit cell size generally needs to be smaller than the wavelength of light. Fortunately, the advances in nanofabrication technology enable us to realize those artificial building blocks with high fidelity, so as to precisely implement any desirable optical functionalities with high performance. With the rapid advance in metasurface research over the past decade, various designs of metasurfaces have been realized to deflect[1], focus[2]–[4], and manipulate the polarization of light[5]–[7].

The first metasurface concept was proposed to impart an abrupt phase change to light after propagation through a thin layer of metallic resonators[1]. The principle of wavefront shaping is conceptually similar to reflectarray and transmitarray antennas in the microwave regime but through the use of planar metallic interface[1]. By introducing spatially varying phase across the interface, the interference between adjacent antennas can produce a desirable radiation pattern. As a result, generalized Snell's law was derived by incorporating phase discontinuity from Fermat's principle, leading to the generalized law of refraction (Fig. 1.1a)

$$\sin(\theta_t)\, n_t - \sin(\theta_i)\, n_i = \frac{\lambda_0}{2\pi}\frac{d\varphi}{dx} \tag{1}$$

where n_t and n_i are the refractive indices of the two media; λ_0 is the free-space wavelength and $\frac{d\varphi}{dx}$ is the gradient of phase discontinuity introduced along the interface. The phase control mechanism was based on the excitation of two resonant modes in V-shape nano-antennas, resulting in a 2π phases coverage for the mid-infrared light. By properly engineering the geometries of each individual antenna, spatially varying phase delays can be introduced to transform an impinging wavefront into anomalous refraction (Fig. 1.1b) and vortex beam generalization. Apart from phase-only modulation, plasmonic structures such as C-shape resonators[8] were also proposed for complex wavefront modulation including independent phase and amplitude control. However, the key issue with the use of metallic components is the Ohmic loss at optical frequencies, which can be substantially amplified in the presence of resonances. Such loss results in reduced efficiency as well as function degradation which limit their applications for realizing state-of-art optical devices and systems. Furthermore, metallic resonators generally do not possess an isotropic response and normally require complex structural geometries to overlap magnetic and electric resonances. This can impose technical challenges to precisely define the structures at the scale of submicron and

nanometer. In the following part, I will mainly focus on optical metasurfaces based on low-loss dielectrics, and briefly review their applications for high-efficiency free-space optics.

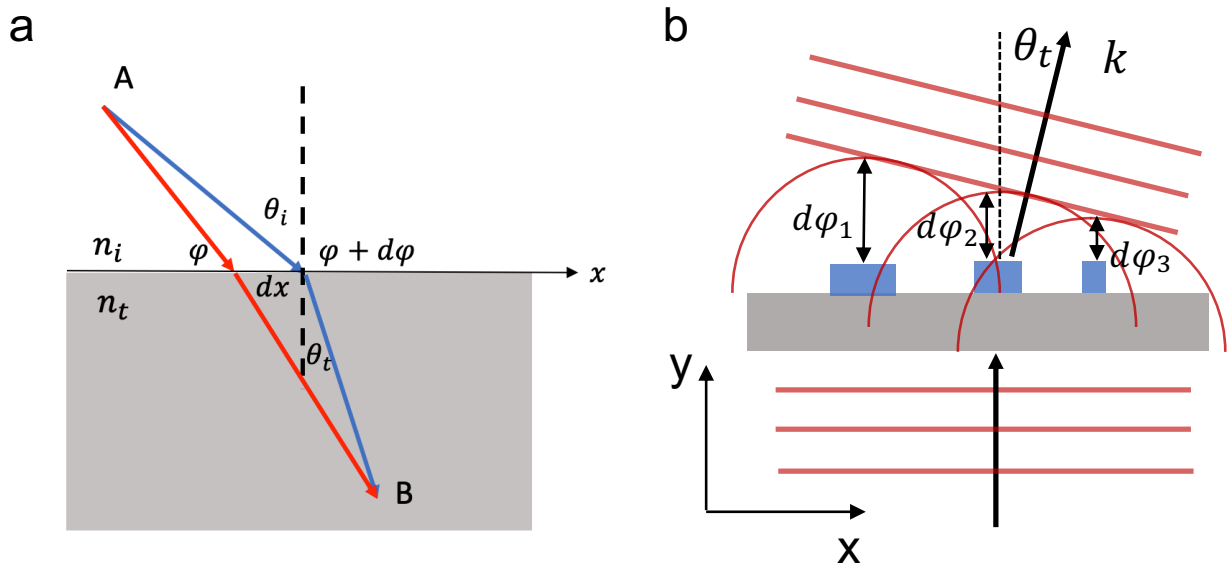

Figure 1.1. Generalized Snell's law and metasurfaces for abrupt wavefront control. (a) A schematic of the model to derive the generalized Snell's law. A phase gradient ($d\Phi$) is introduced along the interface between medium 1 (n_i) and medium 2 (n_t). The same optical phase length is prescribed based on Fermat's principle between the two paths denoted by red and blue lines. (b) Metasurface for wavefront control. The interface consists of spatially varying nano-antennas.

1.2 Dielectric metasurfaces for flat optics

Given the above limitations in metals, it is reasonable to consider switching the material platform to low-loss dielectrics. In particular, high-contrast dielectrics supporting Mie resonances have become an ideal solution for highly efficient wavefront modulation at optical frequencies. As opposed to current flow in metals, the dielectric Mie resonances are excited in the high-index medium via the oscillations of displacement current. Isotropic response can be supported by employing simple resonator geometries such as sphere, cylinder and cube, and the spectral locations and mode orders can be easily tuned through local geometry modifications. With recent advances, high-index transparent materials such as silicon (Si)[4], [9]–[11], titanium oxide

(TiO_2)[3], [12], [13], silicon nitride (Si_3N_4)[14], [15] have been widely adopted as the metasurface constituents in different optical regimes. By properly adjusting one or more geometrical parameters of each element in the metasurface plane while employing a simple geometry, the wavefront can be spatially tailored with low intensity attenuation and subwavelength spatial resolution, opening the door to planar and ultrathin optics with high efficiency that can be potentially mass fabricated at low costs using standard micro- and nano-fabrication processes.

Ideally, a full 360° (2π) phase coverage should be produced by the chosen resonator to achieve a complete cycle of phase modulation. To date, various dielectric nanostructures have been proposed for realizing a 2π phase coverage while maintaining a near-unity transmission. In particular, Huygens surface was extensively explored to support overlapped electric and magnetic dipole resonances[16], [17]. At the resonant frequency, the presence of two fundamental modes with an identical strength lead to the complete cancelling of backscattering along with a 2π phase coverage. Several groups have investigated such platform for beam steering[18], holograms[19] and reconfigurable metasurfaces[20], [21]. However, Huygens surface exhibits several limitations for practical applications due to their high sensitivity to angle of incidence and fabrication imperfection. In addition, the coupling between adjacent resonators is significant and can degrade the device efficiency for large angle deflection due to the rapid varying phase profiles. Recently, high-contrast transmit-arrays (HCTAs) composed of nanoposts have been widely adopted by several groups as an alternative building block that can outperform other classes of metasurfaces for certain applications. The HCTAs, which have a higher aspect ratio, are conceptually similar to the truncated waveguide proposed by Prof. Lalanne in 1998 [22]–[24]. However, compared to Huygens surface, the HCTAs possess several advantages due to their localized resonance, small angular sensitivity, and high transmission efficiency over a relatively broadband [4]. Given the

fact that the design of spatially varying metasurfaces are generally based on local approximation, the absence of coupling is crucial for defining the global function of metasurfaces by directly applying the physical knowledges that have already been well-established in conventional optics. As a result, the HCTAs prove to be a versatile platform for realizing metasurfaces that can mimic the functionalities of conventional optics through rapid and ease of design mechanisms.

With recent advances, various dielectric metasurface devices have been demonstrated with efficiencies comparable to the state-of-art commercially available counterparts. One of the landmarks that spurs the dielectric metasurface research is the rapid development of metasurface lens, which is commonly referred to as metalens (Fig. 1.2b). Being recognized as one of the top ten breakthroughs of the year by *Science*[3], metalens has proved to be a classical example that manifests the advantages enabled by several unique capabilities provided by metasurfaces. First, to realize a lens with a large numerical aperture (NA), a proper sampling resolution, Λ, has to be achieved based on the following Nyquist criterion[25]

$$\Lambda < \frac{\lambda}{n + NA} \tag{2}$$

where λ is the free space wavelength, and n is the background index. At optical frequencies, Λ is set to be on the order of submicron if one wants to realize a high NA lens, which is challenging to define using conventional machining techniques such molding and polishing. Second, the conventional refractive lenses generally have a concave or convex shape, and such bulky form factor is not compatible if one wants to explore their integration into ultracompact optoelectronic systems. In the context of metasurface, however, the sampling resolution and fabrication constraint can be addressed in conjunction with industrial micron- and nano-fabrication processes. Furthermore, the ultrathin form factor and material compatibility also allow for ease of vertical integration with electronic systems using the same manufacturing techniques, resulting in a

monolithic optoelectronic system at a potentially lower cost. With recent development in advanced material processing, researchers have experimentally demonstrated visible metalenses consisting of well-defined titanium oxide (TiO_2) nanopillars with a reported focusing efficiency approaching 86%[3]. Owing to the large NA (~0.8) enabled by the subwavelength phase sampling, the metalenses have also shown subwavelength focusing and high imaging resolution comparable to a 100X state-of-art objective.

Similar to conventional refractive and diffractive lenses, however, metalens still suffers from several types of aberrations, mainly due to distorted phase profiles at oblique incident angles, as well as resonant dispersion and phase discontinuity at zone boundaries[26]. Since then, extensive efforts have been devoted to addressing the issues of coma[27][28] and chromatic aberrations[13], [29]–[31] for far-field, multiwavelength and white light imaging. In combination with the conventional microscopy systems, a plethora of compact meta-systems were also investigated aiming at reducing the overall system footprint but enhancing the functionalities of their conventional counterparts, and various groups have demonstrated their associated applications for two-photon microscopy[32], quantitative phase mapping[33] and optical coherence tomography (OCT)[34]. Apart from the static lens with a determined focal length, extensive efforts have also be made to develop tunable metalenses by employing various tuning mechanisms such as mechanical[25], electric[35] and micro-electromechanical system (MEMS)[36]. While the majority of the metalenses – mostly at the academic phase – were defined using the point-by-point lithography techniques such as electron beam lithography (EBL), initial efforts have been made to pave the path towards rapid, low-cost and high-volume manufacturing compatible with the standard industrial micro- and nano-fabrication processes. With recent advances, large-scale metalenses have been mass fabricated on a wafer level using i-line

stepper[37] and deep-ultraviolet (DUV) projection lithography[38], and decent focusing performance free of spherical and astigmation aberrations have also been experimentally demonstrated.

The wavefront shaping capability enabled by metasurfaces also possess great advantages for realizing arbitrary and complex functionalities beyond the parabolic phase profiles of lens. One important application is to explore aspherical freeform surfaces for 3D projection, a technique commonly known as holography (Fig. 1.2c). Unlike photography or volumetric display, holography is a technique that contains true 3D information with accurate depth cues and wide viewing angles. In traditional holography, commercially available systems such as spatial light modulator (SLM) or diffractive microrelief have been widely used, but their large pixel sizes ($> 5\ \mu m$) impose limits for achieving high-efficiency diffraction, which is necessary for realizing high-quality hologram with large field of views (FOVs) free of unwanted diffractive orders. Furthermore, the phase modulation in the microrelief grating generally relies on the multi-level surfaces etched with controllable depths, and such required phase steps are technically challenging to define at submicron resolution. To overcome the above limitations, metasurfaces turn out to be an ideal platform, as they can provide easy access to continuous and well-defined phase and amplitude profiles by laterally defining the meta-atoms using advanced micro- and nano-fabrication. With recent advance, several groups have demonstrated metasurface holograms with supreme figure of merits such as a reported FOV approaching 40°[39] and a diffraction efficiency as high as 99%[40].

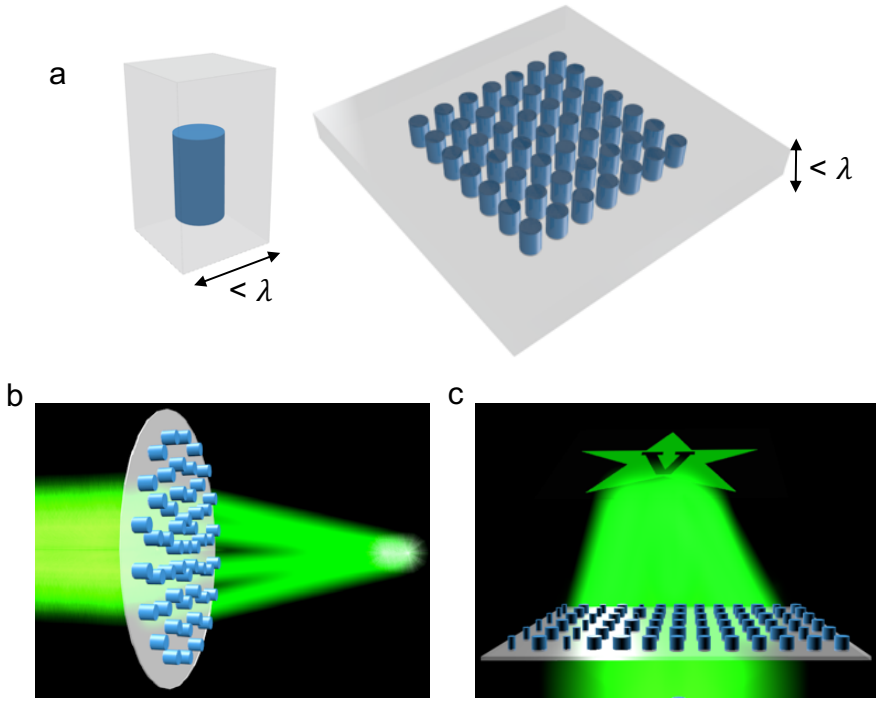

Figure 1.2. Flat optics based on dielectric metasurfaces. (a) A schematic of a metasurface consisting of subwavelength dielectric building blocks. (b-c) A schematic of a flat lens (b) and a hologram (c) based on metasurfaces.

Metasurfaces have also emerged as a versatile platform for polarization control enabled by independent phase modulation for two orthogonal polarizations[41][11], which generally can only be achieved by a combination of multiple conventional optical components. The ability to engineer the local birefringence leads to various applications such as vector beam generation[6], chiral imaging[42] and full-stokes polarization camera[43], [44]. In addition, metasurfaces also exhibit unique capabilities for realizing disorder-engineered diffusers that can outperform conventional random media in terms of NA and angular correlation range[45]. Due to the defined randomness encoded as a priori, input-output characteristics can be quickly determined without exhaustive and time-consuming measurements, leading to high-NA (>0.5) focusing for high-resolution fluorescent imaging with large addressable points and a wide field of view (~8mm). Furthermore, through spatial multiplexing of multiple resonators in a single unit cell, metasurface can

simultaneously encode multiple functionalities for different wavelengths[46], [47], [56], [48]–[55], angles[9] and propagation distances[57], with the applications being demonstrated for multilevel information storage, full-color holograms and optical counterfeiting[58]–[60]. In addition to wavefront shaping, dielectric metasurfaces have also proved to be a superior platform for molecular sensing with ultrahigh sensitivity. Based on the strong field enhancement induced by the quasi bound state in the continuum (BIC), detection sensitivity as high as ~2000 molecules per μm^2 can be achieved[61], [62], which surpass their plasmonic counterparts by an order of magnitude for certain applications.

1.3 Inverse design of metasurfaces

Metasurfaces combined with conventional design templates based on physical intuition and a small set of parameter sweep enable ease and rapid design of various types of free-space optical elements. However, with an increasing complexity in functionalities, system architectures, and the demand for the state of art performance, the convention design methods begin to show limitations for providing the proper knowledge basis as the guidance to design the required functionality with a desirable efficiency. For example, the metasurface gratings and lenses have been reported with high efficiencies but only for a limited deflection angle and NA, due to the fact the number of resonators that can be fitted within each grating or zone period is largely limited. One can increase the compactness of each unit cell by decreasing their pixel size, but the coupling between the adjacent scatters can modify their overall scattering properties, resulting in a severely distorted wavefront and reduced efficiency. Besides, the large number of additional sets of tuning parameters lead to exhaustive search that are not feasible for designing large-scale multifunctional metasurface systems.

For this reason, significant efforts have been devoted to employing inverse design that can overcome the limitations of conventional methods in terms of efficiencies and functionalities[63], [64], [73], [74], [65]–[72]. Broadly, the inverse design ignores the underlying physical phenomena that occur within the systems, while only feeding the input, output and certain constraints as the primary conditions into the solvers for the purpose of reaching an optimal figure of merits (FOMs). By incorporating a specific feedback mechanism that aims to gradually increase the FOMs in an iterative manner, the device parameters can be modified in each iteration and the FOMs can eventually reach either a global or local maxima.

Several inverse design techniques have been developed such as full-parameter search[75]–[77], adjoint-based optimization[63], [65], [67] and machine learning[66], and they have been used to produce on-chip devices for efficient mode conversion and splitting[74] with a small footprint and robustness to fabrication errors and temperature shift. Inverse design for free-space nanophotonics including metasurfaces have also been explored for large-angle beam deflection[63], and high-NA focusing[68], as well as cascaded meta-systems with multifunctional capabilities[67], [78]. Despite their success for small-scale applications, inverse design is generally computationally intensive and requires iteratively full wave simulations to reach a certain optima. This issue can be a critical limitation to design large-scale complex metasurface systems, as the full wave simulation over a large 3D volume containing tens of thousands of nano-elements is computationally demanding. So far, adjoint-based optimization turns out to be one of the most efficient inverse design techniques, as it can simultaneously map out the permittivity gradients throughout the entire optimized region only through two full wave simulations: forward and adjoint[65], [71]. The electric fields excited from the two simulations can then be used to determine the local permittivity gradient that serves to gradually increase the total FOMs. While the full-

wave simulation is still required for mapping out the whole design space, by properly sampling the modeling areas and stitching the individually optimized regions together, large-scale metasurfaces can be designed in a computationally efficient manner[68]. Beyond the application aspects stated above, inverse design also provides new perspectives for exploring novel fundamental phenomena in the fields of nonlinear[79], [80], nonreciprocal[81], topological[82], [83], 3D photonic band gap[84] and near-field[85]–[88] optics.

1.4 Non-local flat optics

To date, the majority of the metasurface research are focused on their capability for wavefront manipulation in the *spatial* domain (Fig. 1.3a). The optical response in the *momentum* space, also referred to as nonlocality, is far less investigated due to their seemingly limited applications. In fact, angularly dependent response ideally should be mitigated to avoid performance degradation arising from additional mode excitation and unwanted diffractive behaviors. However, the modulation of signals in momentum space could potentially be used to enhance signals that are not easy to observe in real space. In biological imaging, for instance, the boundaries of the transparent cells, represented as the scattered light in the form of high-$\boldsymbol{k}$, are generally hard to distinguish due to the fact that most of the detectors are only sensitive to light intensity. However, the edges can be locally revealed if one could selectively filter out the unscattered low-$\boldsymbol{k}$ signals while allowing the high-$\boldsymbol{k}$ information to pass through, leading to a better visual perception for cell inspection and detection. In addition to high-pass filtering, $\boldsymbol{k}$-space control could also enable other applications for image processing such as noise reduction, period extraction, as well as mathematical operations including derivative and integration[89]. Compared

to digital signal processing, optical analog computing can be potentially faster and more energy efficient, which are desirable for today's demand for big data applications.

So far, the most common way to modulate optical signal in momentum space is based on Fourier optics, which involves the use of multiple lenses and filters along the optical pathway. The concatenated systems, however, are generally not compatible with ultracompact systems due to their bulky form factor and additional alignment complexity. Alternatively, nonlocal flat optics, with the ability to support in-plane guided mode (Fig. 1.3b), can directly engineer the light in momentum space without Fourier transform, allowing us to significantly reduce the system footprint and complexity. With recent progress, researchers have explored various types of nonlocal optics based on the mechanisms such as surface plasmon[90], phase shifting grating[91] and guided resonance [92], [93].

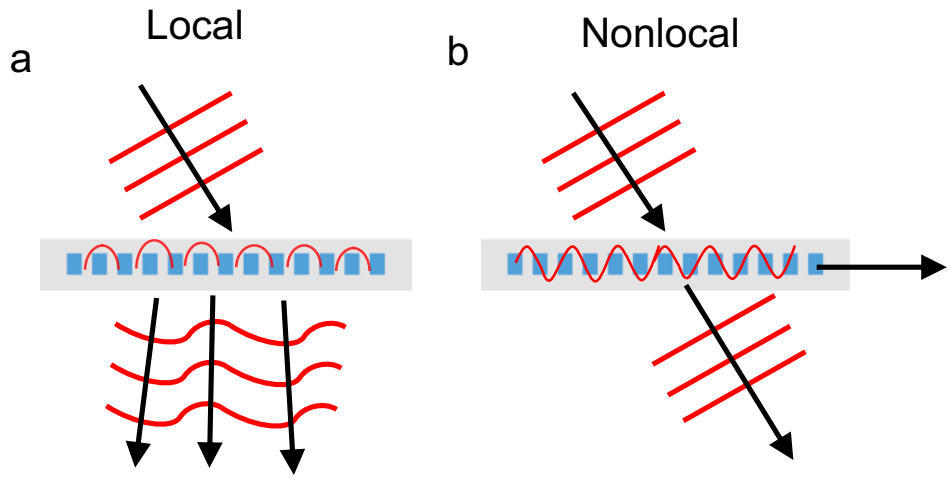

Figure 1.3. Nonlocal flat optics. (a) Schematic of a local metasurface. Each meta-atom serves to impart a local modulation on the incident wavefront. (b) Schematic of a nonlocal metasurface. The neighboring meta-atoms interact collectively, leading to an in-plane guided resonance supported within the slab. The Fano interference between the direct transmission and the guided resonance can lead to near-unity back reflection or transmission.

1.5 Multilayer dielectric metasurfaces

Despite the versatile design freedoms provided by metasurfaces, the functionalities that can be encoded on a single layer substrate are still largely limited. This is due to the fact that the meta-atoms are already densely packed in a subwavelength manner, and it is hard to integrate additional functions without affecting each separate performance and efficiency. This can lead to critical issues such as limited operation bandwidths and functionalities, as well as constrained design flexibilities. To realize multifunctional metasurfaces that can operate at multiple or continuous band, spatial multiplexing or interleaving methods were employed[48]–[50], [94], but they suffer from either low spatial filling fraction or field crosstalk, both of which can result in distorted phase front and low efficiency. Ultimately, it is necessary to explore the third dimension if one wants to increase the engineering space without affecting efficiency and individual resonator response. An example of multilayer metasurface is provided in Fig. 1.4 below.

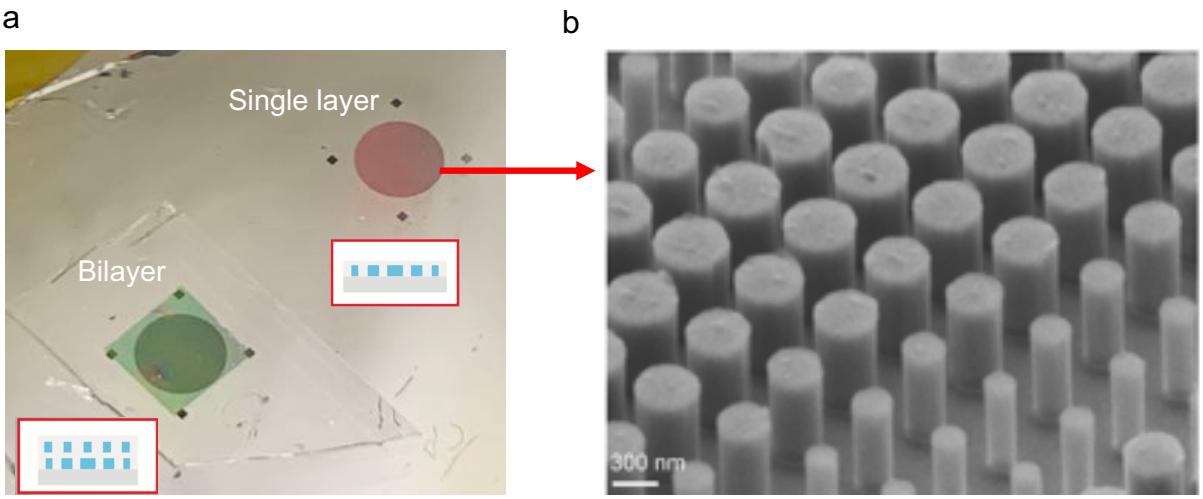

Figure 1.4. Demonstration of multilayer metasurface. (a) Optical image of a single layer metasurface (top right) and a bilayer metasurface (bottom left). The insets shows schematics of the device cross sections. (b) SEM image of the fabricated Si nanostructures.

The fabrication of multilayer dielectric nanostructures remains a challenge in metasurface community. Unlike multilayer plasmonic constituents[53], the growth of dielectrics is generally not compatible with multilayer lithography. While it is possible to fabricate bulk metamaterials with identical layered structures using multilayer chemical vapor deposition and top-down reactive ion etching[95] (Fig. 1.5a)., the structure remains 2.5D with limited added design flexibilities. Recent work has shown that patterning metasurface on both sides of a substrate enables wide-angle aberration correction[27], [96], but the metasurfaces are separated as far as hundreds of microns which negates many of the advantages of using ultrathin elements and causes many design and performance limitations (Fig. 1.5b). Tightly-spaced metasurfaces, with each layer independently designed, becomes an ideal platform for effectively multiplexing functionalities while preserving an ultrathin form factor (Fig. 1.5c).

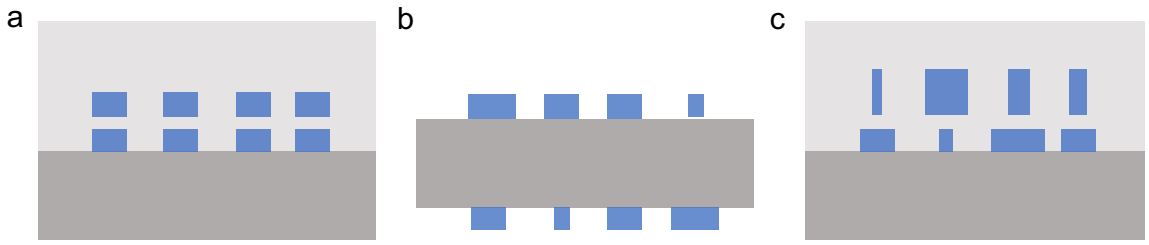

Figure 1.5. Multilayer metasurfaces (a) A schematic of bulk metamaterials with identical layered structures. (b) A schematic of a compound metaoptic. The metasurfaces are patterned on both sides of a substrate. (c) A schematic of a tightly-spaced multilayer metasurface. The multilayer system provides additional design freedoms while maintaining an ultrathin form factor.

1.6 Organization of the thesis

In this dissertation, I present my efforts to develop multilayer flat optics for realizing multifunctional metaoptics and analogue image processing systems. The improved design flexibilities arising from additional layers have been investigated for exploring interesting and novel optical functionalities (Fig. 1.6a-b). In addition, I will also present my contributions to

developing a monolithic compound system for two-dimensional image differentiation (Fig. 1.6c), as well as their associated applications for biological imaging and machine vision.

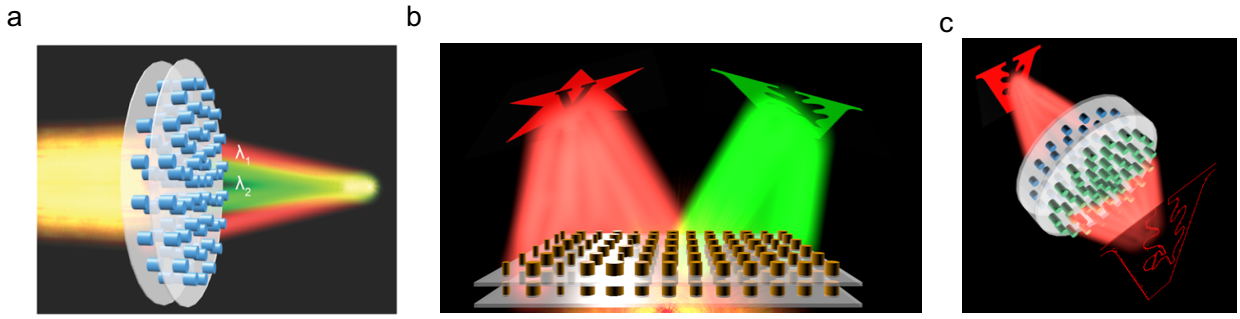

Figure 1.6. Various types of multilayer flat optics. (a-c). Schematics of a multilayer metalens (a), a multifunctional metaoptic (b) and a monolithic compound image processing system (c).

In **Chapter 2**, I develop a unique technique to experimentally realize multilayer dielectric metasurfaces. I show that the use of multilayer silicon-based transmit-arrays enables independent wavefront control at multiple wavelengths. In addition, I will also show how this platform can be applied for realizing multiwavelength metalenses and spectral splitters with high efficiency and imaging resolution.

In **Chapter 3**, I further explore the technique as a generic platform for multifunctional metasurfaces by employing various combinations of unit cells that serve to control different degrees of freedoms of light. I show that independent control over multiple optical properties can be achieved which allows for the realization of various types of multifunctional metaoptics including multiwavelength holograms, multiwavelength waveplates, and 3D holograms.

In **Chapter 4**, I transition my focus to nonlocal flat optics for optical analog computing. I design and experimentally demonstrate a photonic crystal slab exhibiting a quadratic dependent transfer function that mimics a two-dimensional Laplace operator. Based on the ultrathin form factor inherent in the photonic crystal slab, I further explore its vertical integration into various

types of imaging systems to demonstrate their associated applications such as biological imaging and computer vision.

Finally in **Chapter 5** I draw the main conclusion for this thesis and its long term implications. In the end, I would like to provide my insight and perspective on the future of multilayer flat optics.

Chapter 2

Multilayer Dielectric Metasurfaces for Multiwavelength Metaoptics

2.1 Introduction

In chapter 1, I have introduced metasurface platform that exhibits an unprecedented flexibility to manipulate the wavefront of monochromatic light with an ultrathin form factor. However, the chromatic aberration remains an intrinsic issue in resonance-based optical elements, making it challenging to create multi-wavelength or achromatic metalenses, full-color holograms, and spectrally multiplexed metadevices. Researchers have demonstrated that the use of a reflective backplane[31], [97] or strongly resonant scatters[30], [98] allows management of dispersion for achieving achromatic performance over limited bandwidths. However, these approaches are only applicable for relatively small phase delay (ie. small lens diameter or low numerical aperture) due to the tradeoff between achieving large dispersion, using resonances, and maintaining linear phase dispersion over a broadband.

Multiwavelength transmissive metadevices, while not ideal for broadband imaging systems, have many applications in fluorescent microscopy[32] and digital displays, such as virtual reality headsets, and computer vision. One common approach to achieve multiwavelength operation is to spatially multiplex resonators on the same substrate, by either engineering multiple closely spaced resonators together using a supercell[52], [99], [100], or interleaving lattices operating separately at each target wavelength[46], [49], [50], [94]. However, these methods have issues with cross-talk between meta-atoms and space filling limitations, leading to reduced efficiency, degraded holographic image quality, and unwanted diffractive orders. Ultimately, due to the limited engineering space using a single resonator layer, it is necessary to obtain an

additional degree of freedom in the third dimension if one wants to design efficient elements for multiple wavelengths.

2.2 Design of multilayer dielectric metasurfaces

In this chapter, we demonstrate independent phase modulation at multiple wavelengths by closely stacking dielectric metasurfaces. This use of multilayer metasurfaces allows the realization of multiwavelength metadevices with improved efficiency. As a proof of concept, we designed and demonstrated two and three wavelength metalenses. A schematic of a metalens doublet along with its phase distribution is shown in Fig. 2.1a. The phase response from each layer, added together, provides the required hyperbolic phase profile at two different wavelengths. The approach results in light passing through multiple resonator layers which also relaxes the requirement to achieve 2π phase shift using a single resonator. In addition, the geometry of each layer is independent providing extra design space for achieving multiwavelength operation, avoiding the issues of coupling and reduced sampling resolution when using a single layer of resonators. By the same principle, a three-wavelength metalens can be designed by a metasurface triplet (Fig. 2.1b). Multilayer metasurfaces have recently been investigated using vertically stacked plasmonic binary zone plates[53]. However, the use of plasmonic resonators results in low efficiency and multilayer lithography is generally not compatible with high index dielectrics which must be grown on a substrate. In past work on dielectric metasurface doublets designed for wide-angle corrected lenses[27], [28] and retroreflectors[96], the metasurfaces are separated as far as hundreds of microns. This large separation negates many of the advantages of using an ultrathin lens and causes many design and performance limitations for multiwavelength lenses and phase plates, as we show in this paper. Here, we develop techniques for realizing dielectric metasurfaces

that are tightly spaced, allowing the realization of ultrathin planar multiwavelength metadevices for a wide range of optic diameters.

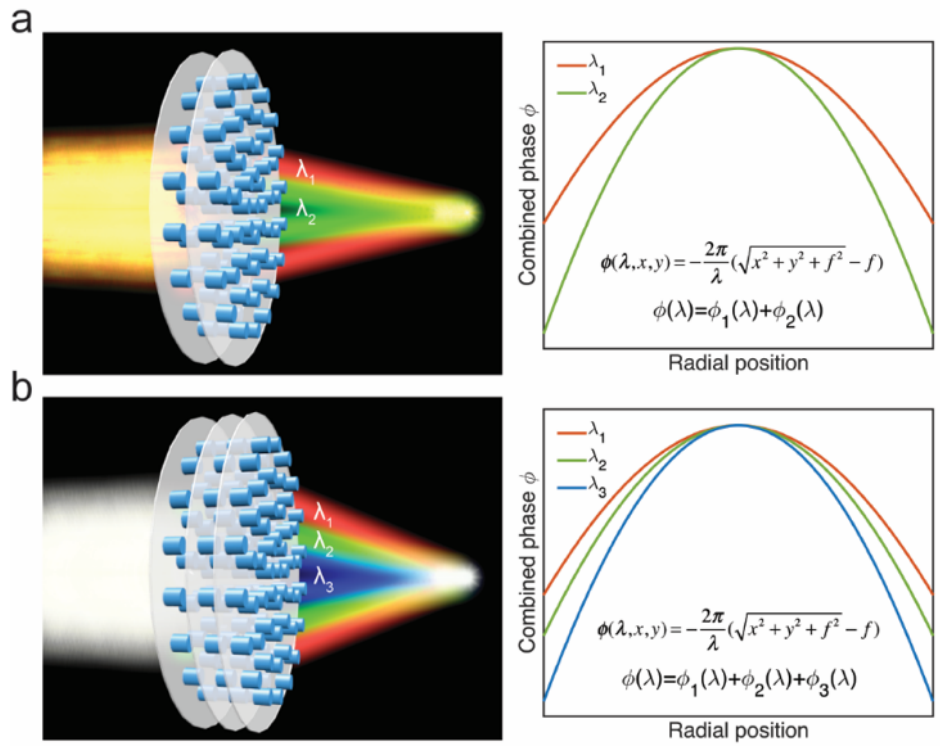

Figure 2.1. Multiwavelength focusing by tightly-spaced multilayer metasurfaces. (a) A schematic of a metasurface doublet focusing two wavelengths at the same focal distance. The phases at each layer are added together to provide the required hyperbolic phase profiles at the two different wavelengths. (b) A schematic of a three-wavelength metasurface triplet lens designed using the same principle. Note that there is only one substrate in the actual device, the semi-transparent discs are guides to the eye in order to avoid the illusion of randomly distributed structures in three dimensions.

The metalenses demonstrated here are based on Si nanoposts with a high aspect ratio. The Si nanoposts, which can be modeled as truncated waveguides supporting Fabry-Perot resonances, are an ideal candidate for transmissive phase scatters due to their high efficiency, localized resonances, and low angle of incidence sensitivity[4]. Fig. 2.2a shows a schematic of the Si nanopost unit cell embedded in a layer of polydimethylsiloxane (PDMS), where the nanopost height is set to be 750 nm with a period of 600 nm. As a proof of principle, target wavelengths of

1180 nm and 1680 nm were selected for designing a two-wavelength doublet metalens. The transmission and phase distributions at both wavelengths (Fig. 2.2b, c) were first simulated as a function of nanopost radius. At each wavelength, nanoposts that sit in transmission dips are excluded from the design database. Fig. 2.2d shows the schematic of the vertically stacked nanoposts embedded in PDMS. The resonators are designed to be closely spaced in the *z*-direction to minimize the effect of wavefront divergence after the first layer, but far enough to avoid coupling (Fig. A3). Apart from the layer-to-layer separation, the fidelity of phase transfer from the first layer to the second also depends on the in-plane phase distribution. Abrupt in-plane phase variation leads to greater wavefront divergence and deviation from a linear combination of the two layers' phase distribution. To combat this issue, the lenses were designed to be large enough so that each zone contains multiple nanoposts with the same size and phase delay. As a result, the transmission coefficient t_1 after the first layer is directly treated as the incident field to the second layer with the transmission coefficient t_2. The overall phase and transmission were calculated as the sum of the phase response ($\angle t_1 + \angle t_2$) and product of the transmission ($|t_1 t_2|^2$) from each layer. To obtain addition degrees of freedom for multiwavelength control, nanopost radii at each layer (r_1 on layer one and r_2 on layer two) were varied independently. The calculated transmission, considering all possible pairs of radii (r_1, r_2), are plotted at 1180 nm (Figure. 2.2e) and 1680nm (Figure. 2.2g) and demonstrate that high transmission can be obtained over a wide range of design parameters. Fig. 2.2f, h show the calculated phase at two wavelengths (1180 in Fig. 2f and 1680 in Fig. 2.2h). Note that the phase distributions are distinct at 1180 nm and 1680 nm and there are multiple choices of (r_1, r_2) available to provide the same phase change at one wavelength but allows arbitrary phase modulation at the other wavelength, providing extra engineering space for multiwavelength operation. The radii of nanoposts on each layer are selected such that the required

hyperbolic phase is achieved for both wavelengths (see details of the design methods in Appendix A.1).

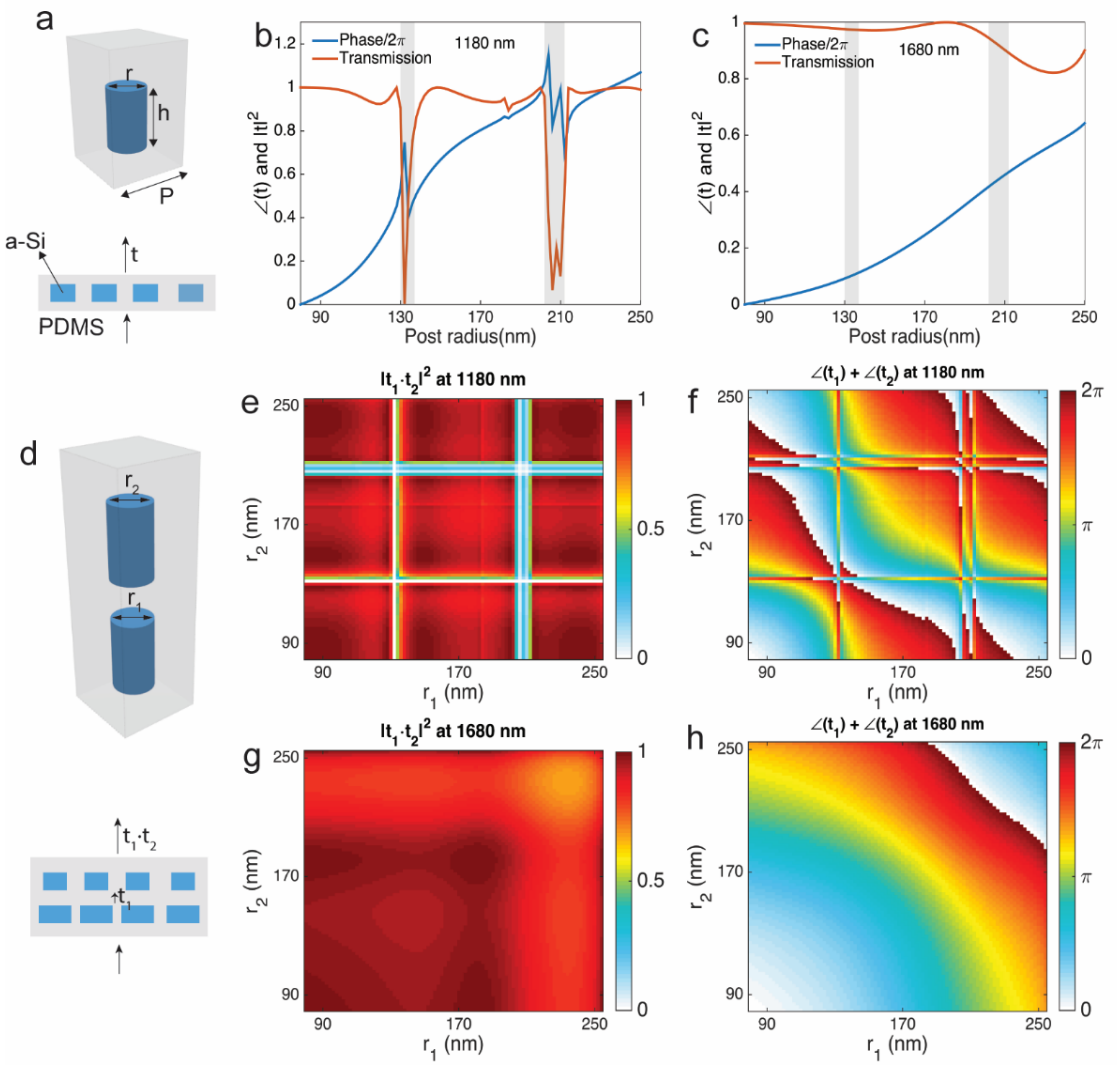

Figure 2.2. Metasurface building blocks and transmissive properties. (a) A schematic of a metalens building block made of an amorphous Si nanopost with a height h=750 nm. The nanopost is embedded in a PDMS layer and arranged in a square lattice with a period P=600 nm. (b, c) The calculated transmission and phase variations as a function of post radii at the wavelengths of 1180 nm (b) and 1680 nm (c). The radii that sit in transmission dips (highlighted by gray stripes) are excluded from the design database. (d) A schematic of a metasurface doublet unit cell. The radii (r_1, r_2) at each layer were varied independently. The overall transmission and phase were calculated as the product of transmission ($|t_1 t_2|^2$) and sum of phase ($\angle t_1 + \angle t_2$) from two layers respectively. (e, f, g, h) The calculated overall transmission and phase for the metasurface doublet as a function of (r_1, r_2) at wavelengths of 1180 nm (e, g) and 1680 nm (g, h).

2.3 Realization of multilayer dielectric metasurfaces

To validate this approach experimentally, we first designed and fabricated a metalens doublet with a 500 μm diameter and a focal length of 540 μm leading to a numerical aperture of 0.42. The fabrication involves semiconductor nanofabrication and material transfer techniques with the key steps of the processes summarized in Fig. 2.3a. The first metalens was prepared using a 750 nm thick amorphous silicon (a-Si) layer grown by plasma-enhanced chemical vapor deposition (PECVD) on fused silica. The metalens along with alignment marks was defined using electron beam lithography and reactive ion etching (RIE). A thin layer of diluted PDMS was then spin coated to encapsulate the nanoposts and to form a thin spacer layer that allows close stacking of the second layer (Fig. 2.3a (i)). The second substrate was prepared by firstly depositing a 300 nm layer of germanium (Ge) on a Si handle substrate followed by 750 nm of a-Si growth on Ge via PECVD. The Si metalens was fabricated using the same procedures as the first, followed by embedding the lens in a thick layer (~50 μm) of PDMS using spin coating. The embedded nanoposts were released from the substrate by dissolving the Ge sacrificial layer (Fig. 2.3a (ii)). The transferred layer was then flipped over with the rod side facing the first layer, aligned using a 2D material transfer stage, and bonded by heating and curing the PDMS (Fig. 2.3a (iii)). A scanning electron microscope (SEM) of the Si nanoposts after RIE is shown in Fig. 2.3b. An optical microscope image of the metalens doublet and alignment marks are shown in Fig. 2.3c, d. While it was not possible to quantitatively determine the distance between the layers, each is in focus under 20X magnification (Fig. 2.3d), indicating the vertical separation is within the focal depth of the microscope, which is 5.8 μm.

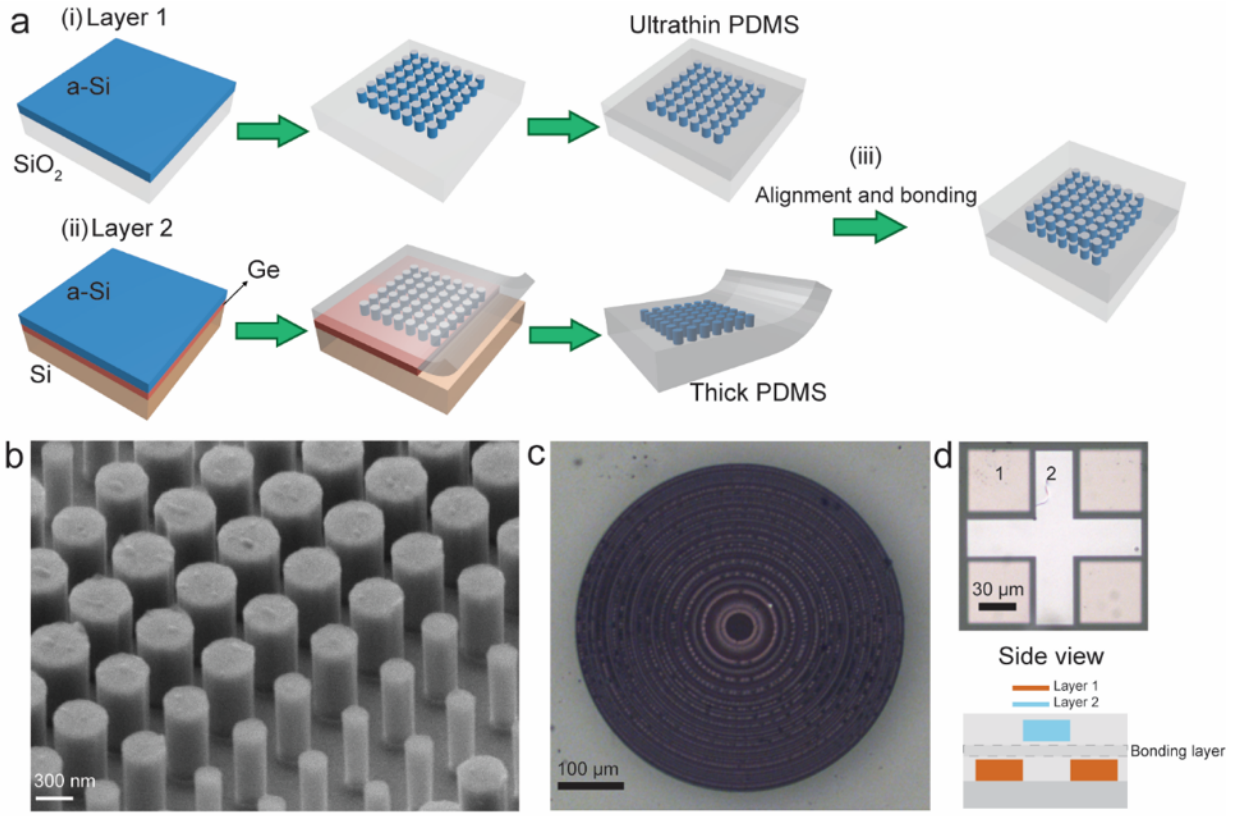

Figure 2.3. Fabrication of metalens doublet. (a) A schematic of the fabrication steps. (i) The first layer of Si structures was defined on a SiO_2 substrate and embedded in an ultrathin polydimethylsiloxane (PDMS) layer using spin coating. (ii) Metasurface structures for the second layer were generated on a Ge/Si substrate and encapsulated by a thick layer of PDMS, followed by releasing the metalens through dissolving the Ge sacrificial layer. (iii) The two layers of metalenses were aligned and bonded. (b) A scanning electron image (SEM) of Si nanoposts before PDMS spin coating. Scale bar: 300 nm. (c) An optical microscope image of the aligned metalens doublet. Scale bar: 100 μm. (d) An optical microscope (20X objective) image of the alignment marks from the two layers along with a schematic of cross-section. Scale bar: 30 μm.

As the precision of alignment can have a critical effect on the device performance, a 500 μm diameter metalens was simulated as a function of misalignment between each layer. Fig. 2.4 shows the simulated axial intensity profiles under the misalignments of 1, 3 and 6 μm at the two wavelengths, demonstrating that performance remains good for layers that are misaligned by as much as 3 μm which is in a range that is achievable using an optical microscope. As the precision of alignment can have a critical effect on the device performance, a 500 μm diameter metalens

was simulated as a function of misalignment between each layer. Fig. 2.4 shows the simulated axial intensity profiles under the misalignments of 1, 3 and 6 μm at the two wavelengths, demonstrating that performance remains good for layers that are misaligned by as much as 3 μm which is in a range that is achievable using an optical microscope.

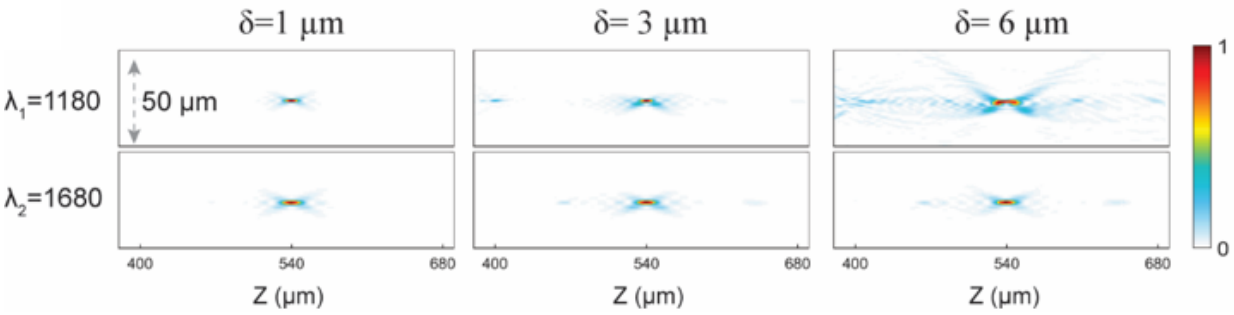

Figure 2.4. Effect of misalignment. Simulated axial intensity profiles of the metalens doublet under the misalignment of δ=1, and 3 and 6 μm at the two wavelengths.

2.4 Optical characterization of multilayer dielectric metasurfaces

The fabricated metalens doublet was characterized by illuminating the optic using a collimated and unpolarized supercontinuum laser which was passed through a monochromator (Fig. A4). To evaluate the performance of the metalens doublet, the full wave simulations were carried out using a 3D finite difference time domain (FDTD) solver (MEEP)[101]. Due to limited computational resources, a lens with a diameter of 100 μm with 5 μm layer spacing and a numerical aperture of 0.42 was used in the simulation (see details of simulation in Appendix A.1). The resulting focal spot profiles are presented in Fig. 2.5a, indicating diffraction limited FWHMs of 1.43 and 2.05 μm at 1180 and 1680 nm, respectively. Fig. 2.5b shows the measured focal spot profiles at 1180 nm and 1680 nm, and the full-width at half-maximums (FWHM) are 1.74 μm and 2.57 μm at 1180 and 1680 nm, respectively. Fig. 2.5c and 2.5d shows the simulated (c) and measured (d) axial intensity distributions along the propagation (z) direction, illustrating the same

focal distance for the two wavelengths. The slight aberrations in the experimental beam profiles are attributed to a lateral misalignment of 3 μm between the lenses during bonding. The misalignment also results in a weak secondary focal spot at z=400 μm for 1180 nm. The precision of alignment is affected by swelling of the PDMS layer and stretching due to uneven engagement during bonding. The misalignment tolerance is improved as the lens size becomes larger, assuming the numerical aperture is held constant (see details of simulation in Appendix Fig. A.2).

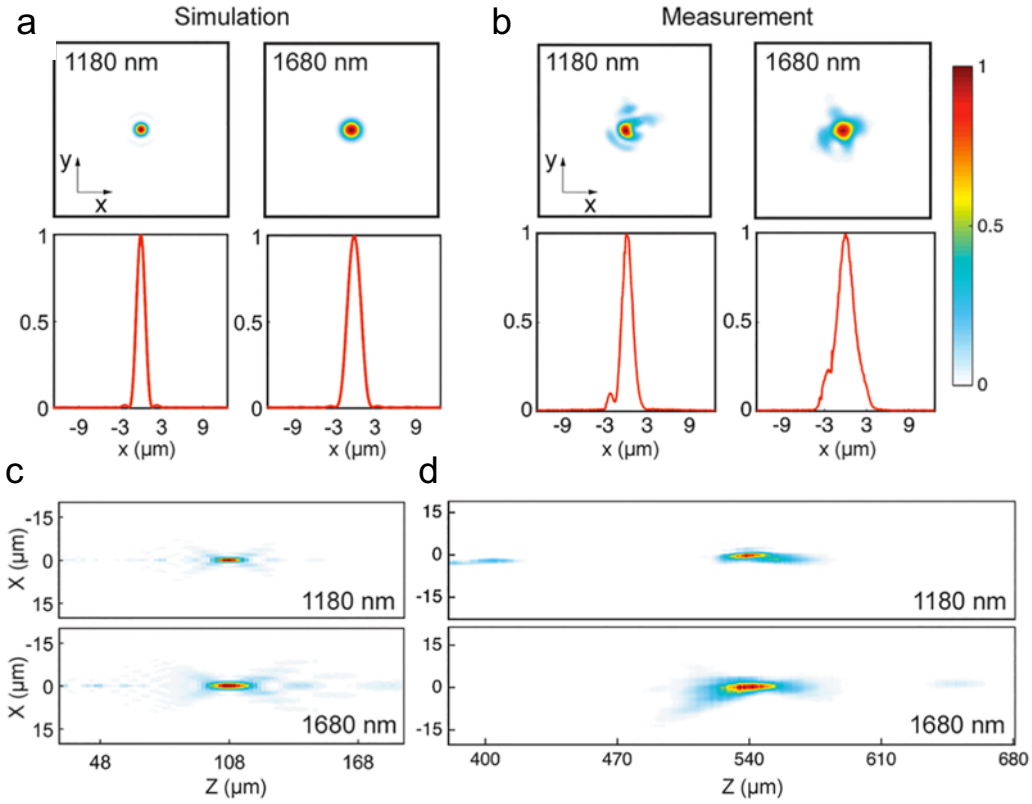

Figure 2.5 Optical characterization of metasurface doublet. Simulated (a) and measured (b) focal spot profiles at the wavelengths of 1180 and 1680 nm. Scale bar: 3 μm. Simulated (c) and measured (d) axial intensity distributions. (e) Simulated focusing efficiency of the metalens doublet (diameter=100 μm, NA=0.42) as a function of layer spacing. (f) Simulated focusing efficiency as a function of numerical aperture. The diameter of the lens is 100 μm with 5 μm layer spacing.

The focusing efficiency is defined as the ratio between the transmitted power passing through a circular aperture at the focal plane and the total incident power on the lens[3], [4]. The

focusing efficiencies were calculated to be 48% at 1180 nm and 56% at 1680 nm while the fabricated lenses had measured efficiencies of 38% and 52% at 1180 nm and 1680 nm, respectively. This can be compared with previous multiwavelength metalenses which employ spatial multiplexing[52], [94] and suffer from either distorted focal spot profiles or low efficiencies, limiting their overall optical performance. However, the efficiency of our lenses remains lower than a singlet metalens[4] (>80% with NA=0.42) primarily due to our design strategy that assumes overall phase delay is a simple sum of the phase at each lens. This strategy neglects wave front divergence after the first layer, trading efficiency for lower computational overhead. Higher efficiencies can be achieved through smaller lens spacing, reducing the role of beam divergence between the layers, which is illustrated in Fig. 2.6a. Our design strategy precludes the use of doublets with a macroscopic layer separation[27], [28], [96], as has been demonstrated in the past. The focusing efficiencies are also expected to be higher for lenses with smaller numerical aperture, which is verified by examining the efficiency of a 100 μm lens with 5 μm layer spacing as a function of numerical aperture (see Fig. 2.6b). These issues could potentially be overcome by employing a more efficient design strategy, such as optimization routine[51], [67], where the layers are designed together.

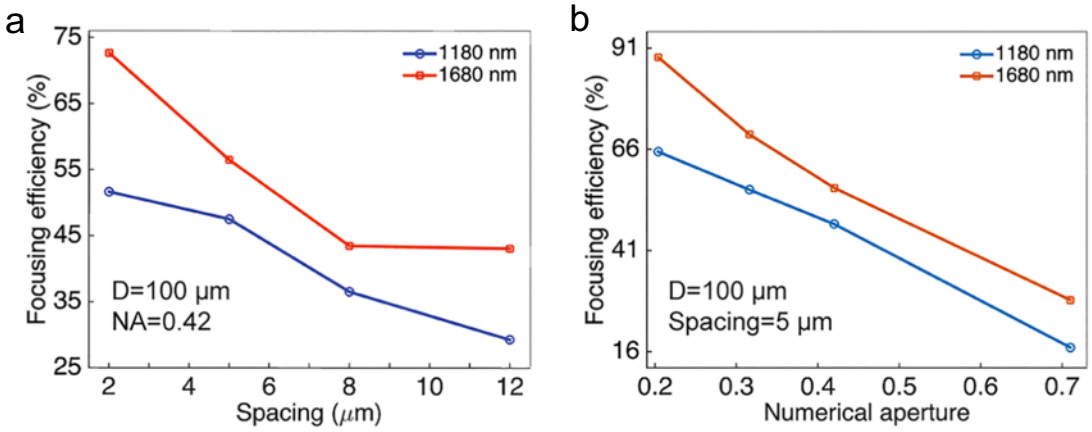

Figure 2.6. Focusing efficiency analyses. (a) Simulated focusing efficiency of the metalens doublet (diameter=100 μm, NA=0.42) as a function of layer spacing. (b) Simulated focusing efficiency as a function of numerical aperture. The diameter of the lens is 100 μm with 5 μm layer spacing.

To demonstrate imaging quality, the metalens doublet was used to image a standard 1951 United State Air Force (USAF) test chart (Thorlabs Inc). The metalens was paired with a tube lens, and positioned at a fixed distance (540 μm) from the test chart. Images at 1180 nm and 1680 nm are shown in Fig. 2.7a and Fig. 2.7b, respectively. Images of group 6 and group 7 with line width of 7.81 μm and 3.91 μm, respectively, are clearly resolved at both wavelengths. The slightly larger blur at 1180 nm can be attributed to a ghost image caused by the back reflection from lens surface, along with the secondary focal spot.

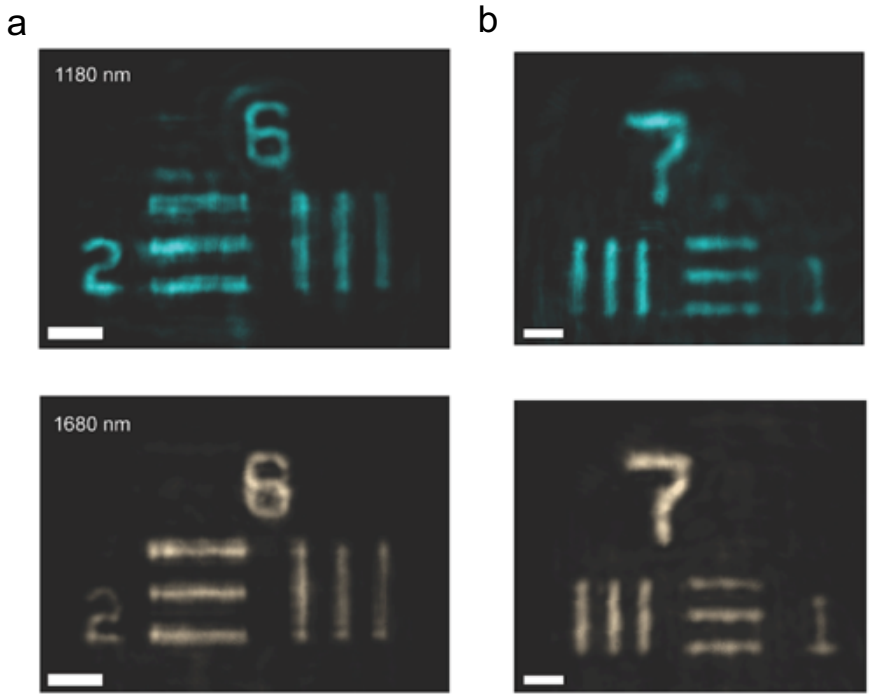

Figure 2.7. Imaging using the metasurface doublet. (a, b) Imaging results of the 1951 United State Air Force (USAF) test chart with the metalens doublet at the wavelengths of 1180 nm (a) and 1680 nm (b). The scale bars in the left column are 20 μm and 10 μm in the right column.

2.5 Three-wavelength metalenses and spectral splitters

This approach can be extended by adding a third layer to form a metasurface triplet. As a proof of concept, a metalens triplet with a diameter of 120 μm and focal length of 200 μm (NA=0.29) was designed at wavelengths of 1180 nm, 1400 nm, and 1680 nm (Fig. 2.8a). Figure 2.8b shows the FDTD simulation of the axial intensity distribution and focal spot profiles at the three wavelengths, which have the same focal distance and no secondary focusing. Diffraction limited FWHMs of 2.22, 2.37 and 3.03 μm and focusing efficiencies of 34.5%, 30.7%, and 51.1%, were obtained for 1180, 1400 and 1680 nm, respectively. These efficiencies surpass past work on three-wavelength transmissive metalenses[53], [99], [100] but are lower than the doublet lens primarily due to increased interlayer scattering from the additional layer. Note that the use of three layers triples the group delay of the nanoposts while allowing for linear phase dispersion, which enables dispersion engineering over a continuous band. In past work on achromatic metalenses based on geometric phase[30], [98], the approach is only applicable for circularly polarized light and exhibits efficiency variations across the spectrum. Here, the use of low quality factor cylindrical resonators allows for flat transmission over a continuous band and a polarization-insensitive response.

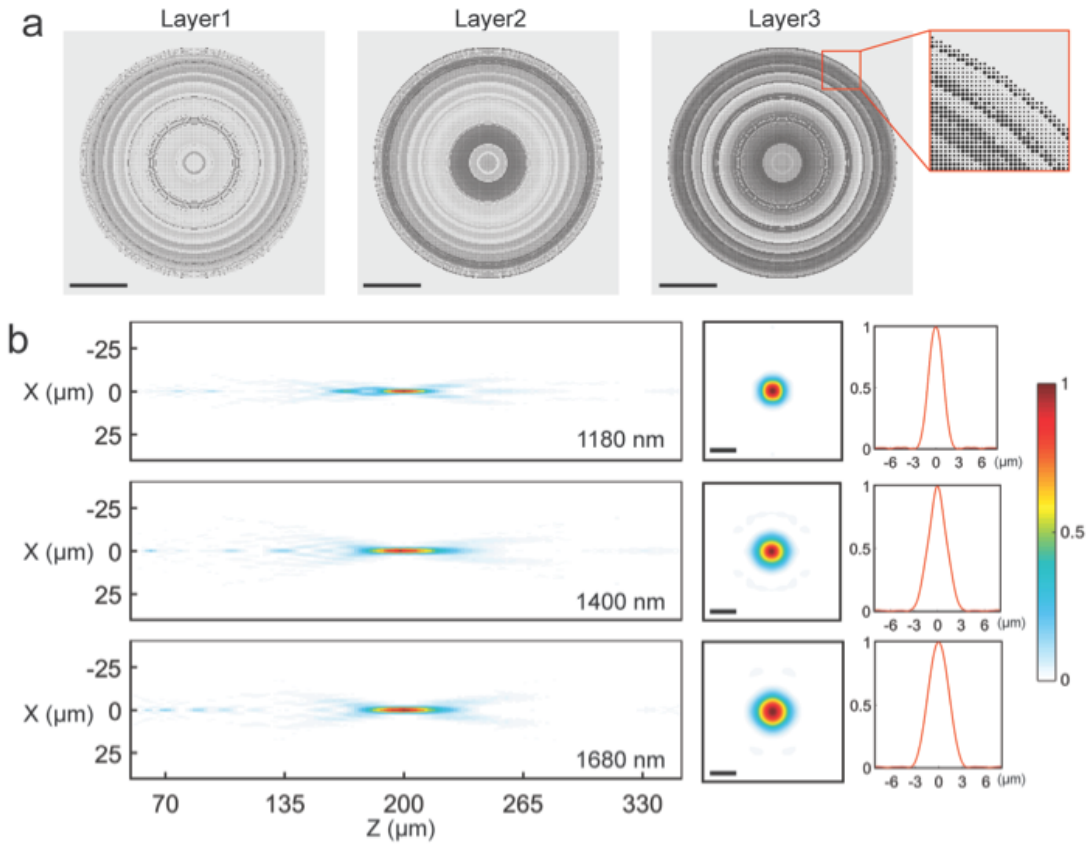

Figure 2.8. Three-wavelength metalens triplet. (a) A schematic of a three-wavelength metalens triplet (size=120 μm, NA=0.29) for the wavelengths of 1180, 1400 and 1680 nm. The Si (black) resonator layers are separated by 2 μm and embedded in a layer of PDMS (gray). Scale bar: 30 μm. (b) FDTD simulations of axial intensity distributions and focal spot profiles, illustrating the same focal distance and diffraction limited focusing for the three wavelengths. Scale bar: 3 μm.

Apart from correcting chromatic aberration at specific wavelengths, the proposed multilayer metasurface platform can also be used to realize multiwavelength functionalities. Such elements could be used for color routing[102], multispectral imaging[42] and wavelength division multiplexing. To validate this concept, we designed a multiband spectral splitter based on a metasurface doublet that can split three wavelengths separately on the same focal plane, a schematic of which is shown in Fig. 2.9a. Here, we have added a third wavelength to the doublet resulting in less demanding fabrication, compared to three layers, at the expense of phase optimization. Based on full-wave simulations, a devices with a 100 μm diameter, 120 μm focal

length, and 20 μm focal plane separation was found to have focusing efficiencies of 25%, 22% and 40% at 1180 nm, 1400 nm, and 1680 nm, respectively. Experimentally, we fabricated a scaled device with a 500 μm diameter, 100 μm focal plane separation, and focal length of 600 μm. The optical image of the device is presented in Fig. 2.9b. Fig. 2.9c shows the measured intensity distribution at the focal plane. The measurement shows intensity peaks at -100, 0 and 100 μm with measured focusing efficiencies of 5.1%, 12.8% and 22% at 1180 nm, 1400 nm, and 1680 nm, respectively. We attribute the lower measured efficiencies to greater misalignment sensitivity due to an irregular arrangement of nanoposts. This was verified by adding a 2 μm misalignment to the simulation resulting in efficiencies being reduced to 5.4%, 8.8%, and 18.4% at 1180 nm, 1400 nm, and 1680 nm, respectively. However, since the size of the focal spot is generally not as critical in spectral splitting applications, the designs could be further optimized by designing supercells containing multiple resonators of the same size to enhance misalignment tolerance at the expense of phase sampling resolution. A higher efficiency is also achievable for splitters with a longer focal distance.

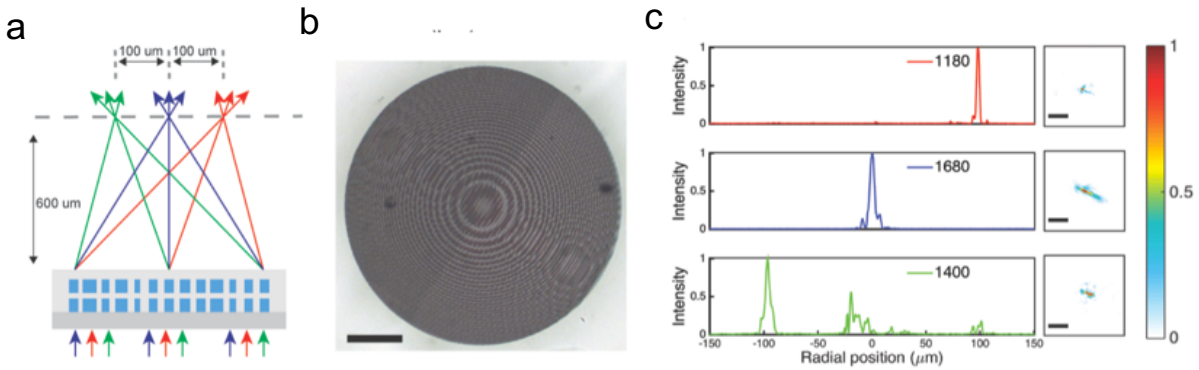

Figure 2.9. Three-wavelength spectral splitter. (a) A schematic of a wavelength splitter using a metasurface doublet. The device is designed to focus three wavelengths (1180, 1400 and 1680 nm) separated by 100 μm on the same focal plane (600 μm). (b) An optical image of the spectral splitter. Scale bar: 100 μm. (c) Measured intensity distributions and focal spot profiles at the three wavelengths. Scale bar: 20 μm.

2.6 Conclusion

In conclusion, we have developed a multilayer transmissive metasurface platform to perform multi-wavelength functionalities, and thus address chromatic aberration at discrete wavelengths for diffractive metadevices such as metalenses and metagratings. The complete and independent control over phase at multiple wavelengths also enables integrated functionalities on a single planar device for applications such as full-color holograms and encoded optical information storage. Such integration can be further extended by superimposing polarization[11] or angle[9] response for increased functionality. Apart from phase modulation, the multilayer fabrication technique outlined here can be used to implement complex monochromatic functionalities which are hard to embed on a single metasurface, such as bianosotropic metasurfaces[103], [104], topology optimized meta-optics[67] and metaholograms with depth cues[57].

Chapter 3

Multifunctional Metaoptics Based on Bilayer Metasurfaces

3.1 Introduction

In chapter 2 we have illustrated multiwavelength functionality using the multilayer metasurface platform. In addition to phase control, however, light is also governed by optical other properties including phase, amplitude, and polarization. A platform for achieving independent control over each of these properties, however, remains elusive due to the limited engineering space available when using a single-layer metasurface. For instance, multiwavelength metasurfaces suffer from performance limitations due to space filling constraints, while control over phase and amplitude can be achieved, but only for a single polarization. Ultimately, the limited design freedom associated with a single resonator layer imposes limits on device functionality.

In this chapter, we explore a bilayer metasurface architecture with the goal of increasing the design space for metaoptics. In chapter 2, we have used this architecture to realize multiwavelength lenses using layers composed solely of nanopost resonators[105]. Here, we use bilayers that comprise various combinations of nanoposts, nanodisks, and rectangular nanopillars to increase the available freedom of design. In this approach, each unique unit cell geometry provides a unique design freedom, and when combined, these geometries enable independent control over any two of the following three properties: amplitude, phase, and polarization. The proposed approach also enables any one of these properties to be independently controlled at two different wavelengths. This freedom is used to realize metaoptics with a wide range of

functionalities, including multiwavelength holograms, multiwavelength waveplates and 3D holograms.

3.2 Concept of multifunctional metasurfaces

A schematic of our general approach is shown in Fig. 3.1. We start with independent control of the phase at two different wavelengths, which is achieved by using nanopost unit cells in both layers (Fig. 3.1a). The nanopost unit cell enables 2π phase coverage while maintaining high transmission, which, in the bilayer format, can be used to encode independent phase-only holograms at two different wavelengths. Independent control of the polarization at two different wavelengths can be achieved by utilizing polarization-sensitive resonators in both layers (Fig. 3.1b). This combination can be used to design independent waveplates operating at each wavelength. Finally, the design space can be further enlarged by using two dissimilar resonator geometries. For instance, independent phase and amplitude control can be achieved by combining a nanopost geometry for phase control and a strongly resonant nanodisk geometry for amplitude control, as shown in Fig. 3.1c. While previous phase-only meta-holograms have suffered from speckle noise and a limited depth of focus, such amplitude and phase holograms enable clearer 2D, as well as 3D, holograms. Furthermore, the use of bilayer metasurfaces enables amplitude and phase control that is independent of the polarization, unlike in single-layer designs, whose operation is restricted to circularly polarized light of a particular handedness[106]–[108]. We believe that the increased engineering freedom provided by bilayer metasurfaces will open new avenues for the development of a wide range of planar multifunctional metaoptics.

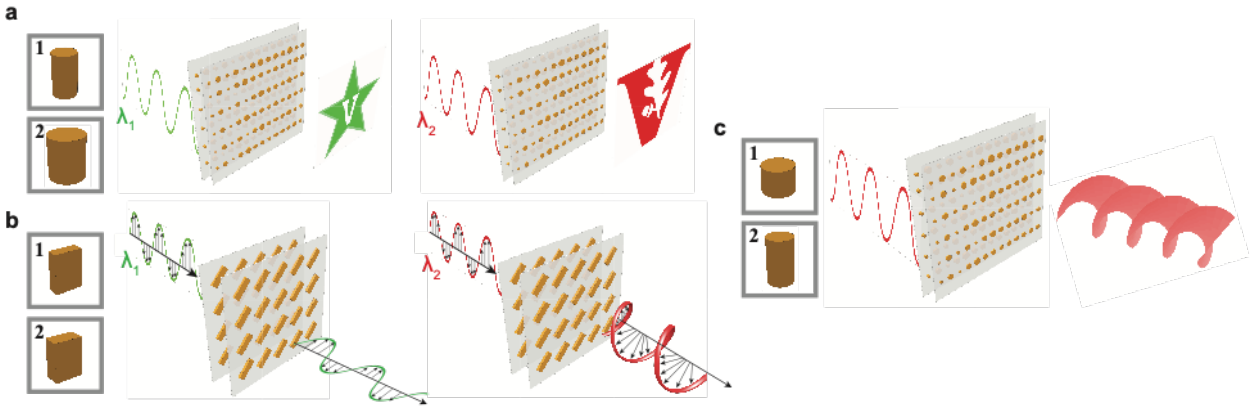

Figure 3.1. Illustrations of multiwavelength holograms, multiwavelength waveplates and 3D holograms using bilayer metasurfaces. (a) Illustration of a multiwavelength hologram. The metasurface is designed to achieve independent phase modulation at two wavelengths. (b) Illustration of a multiwavelength waveplate using a combination of two polarization-sensitive rectangular nanopillar geometries. The bilayer metasurface functions as a half-wave plate and a quarter-wave plate at two different, and independent, wavelengths. (c) Schematic of a metaoptic for producing a 3D hologram with on-axis evolution. The bilayer metasurface comprises nanodisks and nanoposts to enable polarization-insensitive control over both amplitude and phase.

3.3 Metaoptics for multiwavelength phase control

The proposed bilayer metasurfaces for multiwavelength phase control are based on high-contrast transmit arrays made of silicon (Si) nanoposts with a high aspect ratio. The nanoposts, which can be modelled as truncated waveguides, serve as ideal building blocks for phase modulation due to their high transmission efficiency, localized resonances, and low sensitivity to the angle of incidence[4]. To begin, we will explore multiwavelength phase control by cascading two layers of cylindrical nanoposts while keeping them uncoupled in the vertical direction. Figure 2a shows a schematic of the corresponding unit cell embedded in a layer of polydimethylsiloxane (PDMS). The independent variation of the nanopost radii (r_1 and r_2) in each layer provides independent phase control at two different illumination wavelengths. Here, we have arbitrarily selected working wavelengths of 1180 nm and 1680 nm. The height of the Si nanoposts is 750 nm, and they are arranged in a square lattice with a period of 600 nm. To mitigate wavefront divergence

between the layers, the nanoposts are placed in close proximity along the z direction but remain uncoupled, such that the transmission coefficient of the bilayer can be assumed to be the product of the transmission coefficients (t_1 and t_2) of each individual layer. The independent control of the radii in each layer allows one to independently specify the spatial phase profile at each wavelength. Fig. 3.2b and Fig. 3.2c show the required radii in layer 1 (r_1) and layer 2 (r_2), along with the corresponding transmission values, for achieving all combinations of $\phi(\lambda_1)$ (the phase at 1180 nm) and $\phi(\lambda_2)$ (the phase at 1680 nm); the deviation between the designed and ideal phases is presented in Appendix Fig. B2. These design plots can be used to quickly select the structural parameters of each layer to achieve arbitrary and independent phase profiles at the two wavelengths of interest.

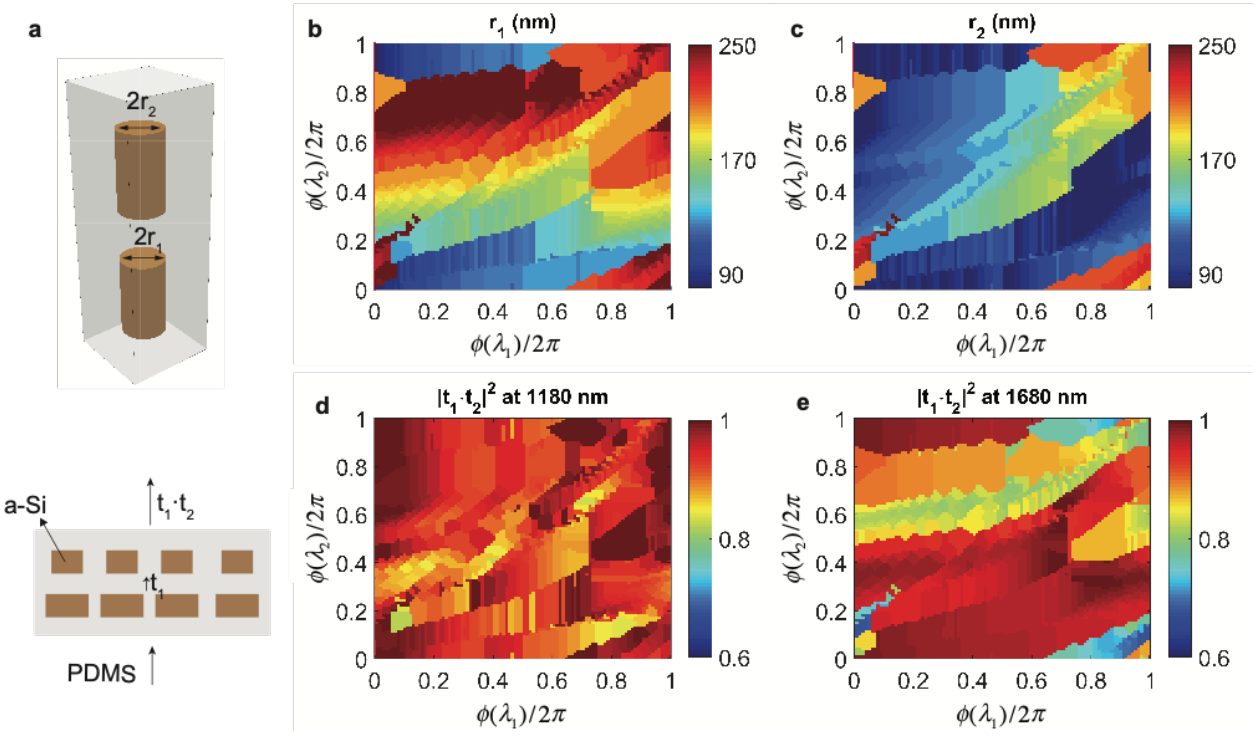

Figure 3.2. Unit cell and design plots for a multiwavelength metaoptic based on nanoposts. (a) Schematic of a bilayer metasurface unit cell consisting of amorphous silicon nanoposts vertically stacked in close proximity. The nanoposts have a height of 750 nm and are arranged in a square lattice with a period of 600 nm and embedded in a PDMS layer. The transmission coefficient (t) of the bilayer is calculated as the product of the transmission coefficients of each

individual layer (t_1 and t_2). (b, c) Design plots showing the corresponding radii in layer 1 (r_1) and layer 2 (r_2), as indicated by the colour bars, for achieving all possible combinations of $\phi(\lambda_1)$ (the phase at 1180 nm) and $\phi(\lambda_2)$ (the phase at 1680 nm). (d, e) Corresponding transmission values ($|t_1 t_2|^2$) at 1180 nm (d) and 1680 nm (e).

In chapter 2, we have used this architecture to realize multiwavelength lenses[105]; here, we extend the approach to the more arbitrary phase profiles found in holograms. A phase-only low-k hologram consisting of two different Vanderbilt University logos projected at the wavelengths of 1180 nm and 1680 nm (Fig. 3.3a) has been designed using the Gerchberg-Saxton algorithm[109]. The holographic metasurface has a size of 500 μm, and the images are designed to be displayed in the Fraunhofer region (see the design details in Appendix B.2). As has been detailed in chapter 2, the fabrication involved the processes including traditional lithography and etching followed by metasurface transfer and bonding. Figure 3.3b shows a scanning electron microscope (SEM) image of the Si nanoposts after RIE. Optical images of the metasurface doublet and the alignment marks in each layer (inset) are shown in Fig. 3.3c. Both layers are clearly visible under a 20× optical microscope, indicating a separation smaller than the focal depth of the objective, which is 5.8 μm.

The metasurface was characterized using an unpolarized supercontinuum laser beam that was passed through a monochromator. To reduce the beam diameter, a lens (f = 200 mm) was used to partially focus the beam onto the sample, and the images produced by the metasurface were directly recorded on a near-infrared camera (for the details of the optical systems, see Appendix B.4). To evaluate the design, the transmission of the bilayer metasurface was calculated as a direct product of the designed transmission through each individual layer. The simulated far-field images are shown in Fig. 3.3d. The absence of unwanted diffraction orders indicates excellent multiwavelength phase coverage. The measured images are presented in Fig. 3.3e, showing good

agreement with the simulations and an absence of twin images such as those observed in previous work on multiwavelength holograms[48], [56] based on spatially multiplexed metasurfaces. The intense spots in the centre are primarily due to the beam overfilling the metasurface, which results in additional zero-order diffraction. The reduced image quality compared with the simulations is attributed to the lateral misalignment of the layers, which is estimated to be 3 μm (see Appendix Fig. B3). The misalignment tolerance is expected to be improved by employing a larger holographic metasurface, under the assumption of the same maximum diffraction angles.

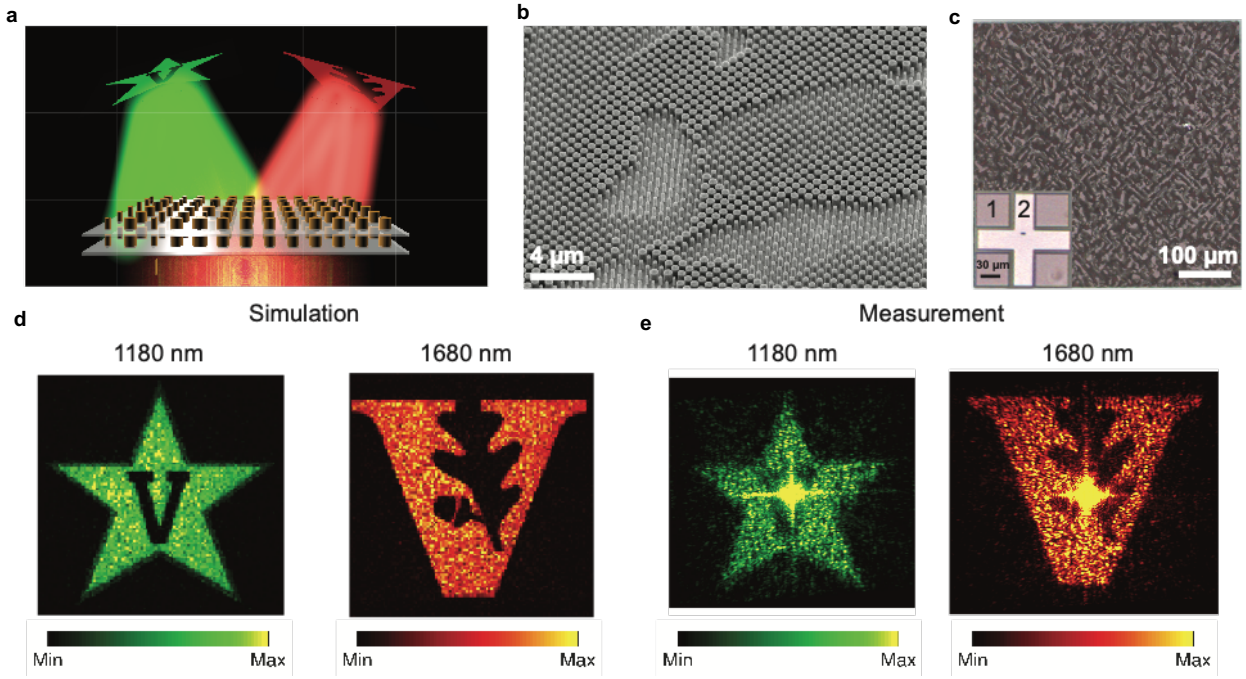

Figure 3.3. Realization of a multiwavelength holographic metaoptic. (a) Schematic of the bilayer hologram consisting of two independent Vanderbilt logos projected at two independent wavelengths. (b) Scanning electron microscope image of the Si nanoposts before PDMS spin coating. (c) Optical images of the bonded metaoptic and the alignment marks in each layer (inset). (d, e) Simulated (d) and captured (e) images produced under illumination wavelengths of 1180 nm and 1680 nm.

While it is difficult to gauge the hologram efficiency due to the prohibitively large simulation domain and the beam overfilling in the experiment, we can quantify the diffraction

efficiency of similar devices. To accomplish this, a wavelength-multiplexed grating was designed to deflect incident light at 1180 and 1680 nm to -15° and 15°, respectively (Fig. 3.4). The grating has a size of 200 μm, and the metasurfaces are separated by 3 μm (for the details of the simulation methods, see the Appendix B.2). The device was simulated using a finite-difference time-domain (FDTD) solver (MEEP)[101], and the absolute efficiency was calculated as the ratio of the power diffracted into the desired order over the total power incident on the device. The calculated transmission is 81.4% at 1180 nm and 83% at 1680 nm, and the relative diffraction efficiencies are 59% at 1180 nm and 61% at 1680 nm, resulting in absolute efficiencies of 48.1% and 50.3% at 1180 and 1680 nm, respectively. These efficiencies are consistent with the theoretical and experimental efficiencies of multilayer metalenses[105] based on the same architecture.

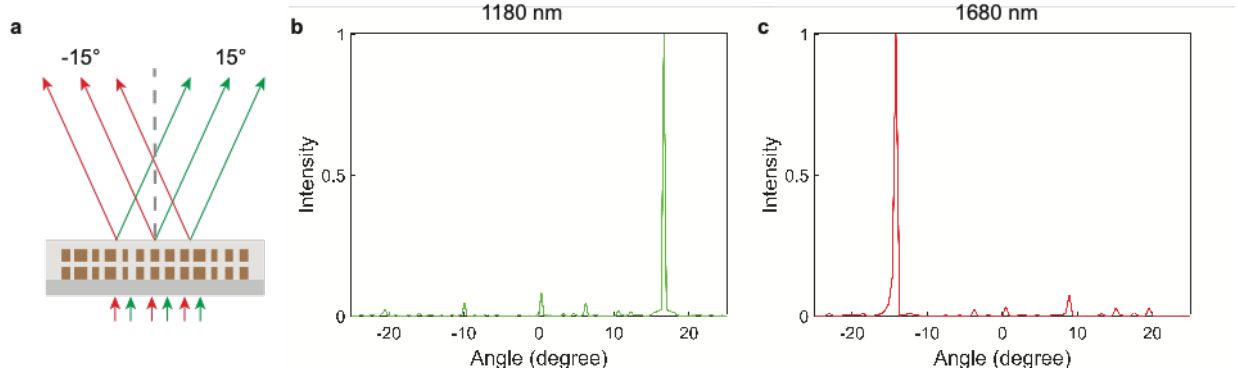

Figure 3.4. Wavelength-multiplexed blazed grating. (a) Schematic of the grating that deflects incident light at 1180 and 1680 nm into beams at 15° and -15°. (b-c) Simulated far-field intensity as a function of diffraction angle at 1800 nm (b) and 1680 (c). The absolute diffraction efficiencies are 48.1% and 50.3% at 1180 and 1680 nm, respectively.

3.4 Metaoptics for multiwavelength polarization control

The proposed approach can be further extended to achieve independent polarization conversion at multiple wavelengths. To achieve this, polarization-sensitive rectangular nanopillars were selected because their length and width can be independently tuned to achieve polarization-

dependent phase retardance. As a proof of concept, we designed a bilayer metasurface that functions as a half-wave plate at a wavelength of 1200 nm and a quarter-wave plate at 1600 nm. Figure 3.5a shows a schematic of the unit cell of this metasurface. The resonators are oriented at a 45° rotation, and the length and width (u, v) are designed to be (400, 280) and (320, 200) nm for each layer, resulting in phase retardances between the long and short axes of π and π/2 for the wavelengths of 1200 and 1600 nm, respectively. Figure 3.5b and Fig. 3.5c show the simulated transmission and phase retardances, respectively, at 1200 nm. The metaoptic has a polarization conversion efficiency ($|t_{xy}|^2$) of over 80% and a phase retardance of π between wavelengths of 1180 and 1230 nm. Figure 3.5d and Fig. 3.5e show the simulated transmission amplitudes and phases, respectively, at 1600 nm for the x and y polarizations. At 1616 nm, we observe a transmission of 47.5% for both polarizations while maintaining a π/2 phase difference, resulting in conversion from linearly to circularly polarized light with 95% efficiency. To numerically determine the polarization state, we extracted the ellipticity, $\tan(\chi)$, by calculating the Stokes parameters (for the details of the calculation, see the Methods), revealing an ellipticity of larger than 0.8 from 1565 to 1670 nm (Fig. 3.5d).

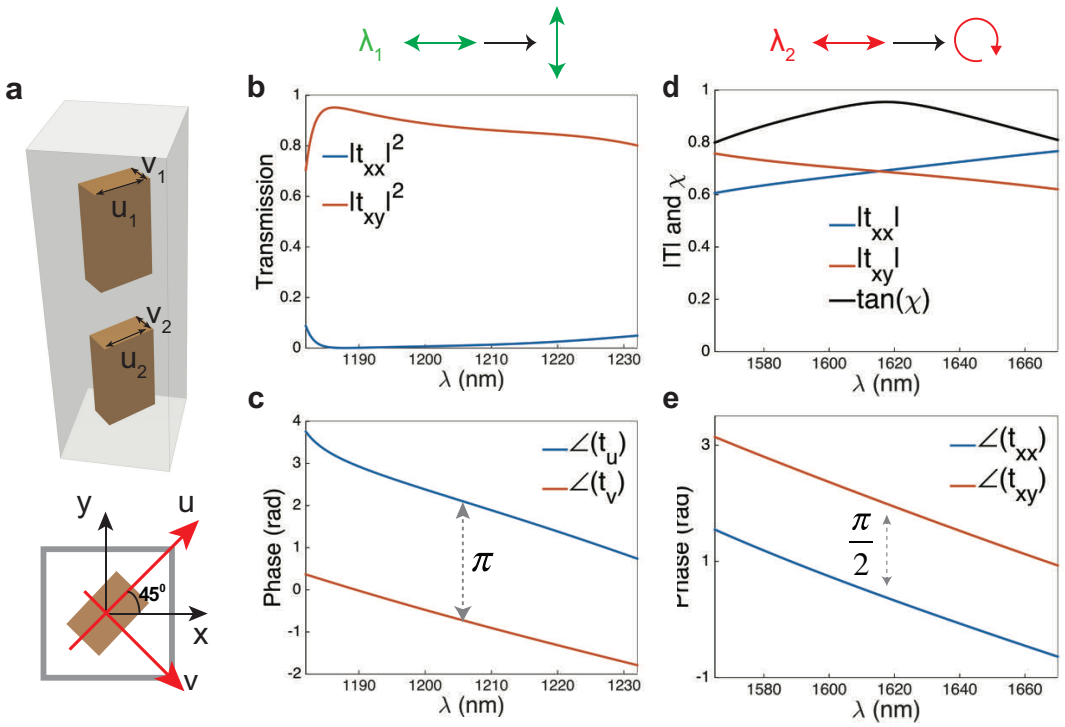

Figure 3.5. Multiwavelength metaoptic waveplate. (a) Schematic of the rectangular nanopillar unit cell. The metasurface is designed to function as a half-wave plate and a quarter-wave plate at 1200 and 1600 nm, respectively. The resonators have a height of 750 nm and are arranged in a square lattice and oriented at 45° with respect to the *x*-axis. The lengths and widths (*u*, *v*) are (400, 280) and (320, 200) in the bottom and top layers, respectively. (b, c) Simulated transmission profiles for the *x* and *y* polarizations (b) and phase delays for the short and long axes (c) at wavelengths near 1200 nm. (d, e) Simulated transmission amplitude and ellipticity ($\tan(\chi)$) profiles (d) and phases (e) for the *x* and *y* polarizations at wavelengths near 1600 nm.

While this functionality could have been achieved using an unstructured material with substantial dispersion, the true advantage of the proposed approach is that any combination of waveplates can be readily realized by modifying the widths and lengths of the nanopillars in each layer. To illustrate this freedom, we present a design graph for achieving all combinations of half- and quarter-wave plates at the wavelengths of 1200 and 1600 nm in Fig. 3.6 (additional details regarding the transmission and ellipticity can be found in Appendix Fig. B1).

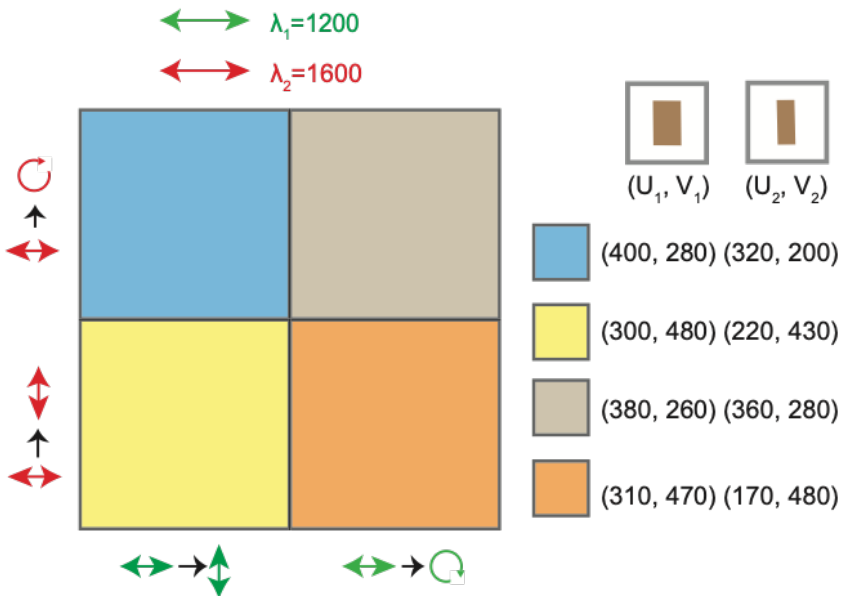

Figure 3.6. Multiwavelength waveplate design graph. Design graph for achieving all combinations of waveplates at the two considered wavelengths. The *x* and *y* axes correspond to the half- and quarter-wave plate cases at 1200 and 1600 nm, respectively, and the colours represent the designed nanopillar widths and lengths, as indicated in the legend on the right.

3.5 Metaoptics for polarization-insensitive phase and amplitude control

Finally, we explore the use of the proposed bilayer architecture to achieve complete control over amplitude and phase. In past amplitude and phase meta-holography, amplitude modulation has been achieved through polarization conversion[106]–[108], resulting in an efficiency loss due to polarization sensitivity. Here, we use a bilayer metasurface composed of polarization-insensitive elements for phase and amplitude modulation. Wavefront control is achieved by assigning phase modulation to one layer and amplitude modulation to the other. Amplitude modulation is achieved by utilizing Si nanodisks that support fundamental Mie resonances at the wavelength of operation, and the spectral positions of the resonances can be adjusted by changing the nanodisk radius. In previous work, similar resonators have been used to achieve Huygens surfaces[110], perfect reflectors[111], and polarizing beam splitters[112]. Here, we have designed the nanodisks to operate near the magnetic dipole resonance, with a transmission amplitude that is controlled by

tuning the structures to work either at or away from the resonance. A schematic of the unit cell is shown in Fig. 3.7a; the nanodisks have a height and period of 440 nm and 600 nm, respectively. Figure 3.7b shows the transmission amplitude and phase as functions of the nanodisk radius at a wavelength of 1400 nm, demonstrating 100% amplitude modulation along with a phase change of π. The second layer is used to implement the designed phase functions by means of cylindrical nanoposts with a larger aspect ratio than that of the nanodisks. Figure 3.7c shows a schematic of the second-layer unit cell, which is used for phase modulation. The nanoposts have a height of 750 nm and a period of 600 nm, and the corresponding transmission amplitude and phase as functions of the nanopost radius are presented in Fig. 3.7d. The transmission dips highlighted in grey were excluded from the design database, resulting in 2π phase coverage and an average transmission of 96%.

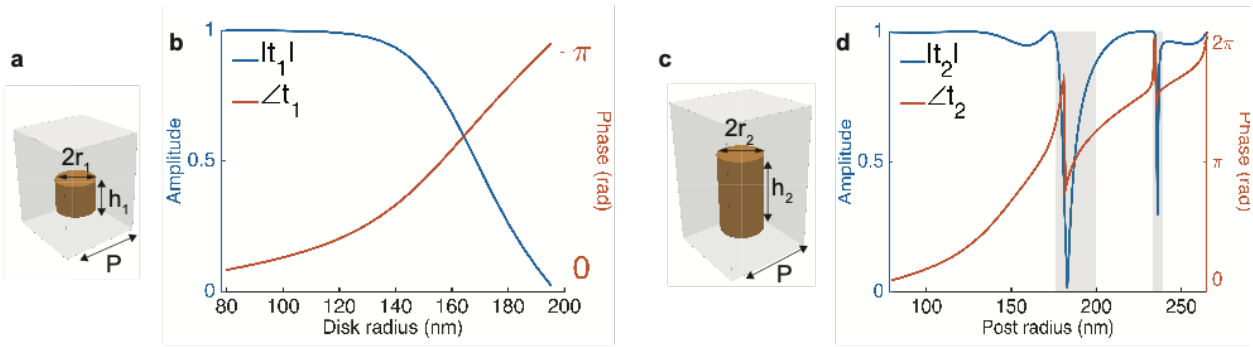

Figure 3.7. Metaoptic for polarization-insensitive phase and amplitude modulation. (a) Schematic of the Si nanodisk that serves as the unit cell for the bottom layer for phase modulation. The disks have a height of h_1 = 440 nm and are arranged in a square lattice with a period of P = 600 nm. (b) Simulated transmission amplitude $|t_1|$ and phase $\angle t_1$ as functions of the disk radius. (c) Schematic of the nanopost that serves as the unit cell for the second layer for amplitude modulation. The nanoposts have a height of h_2 = 750 nm. (d) Simulated transmission amplitude $|t_2|$ and phase $\angle t_2$ as functions of the post radius.

As a proof of concept, we designed a 3D hologram (600 μm × 600 μm) to display a clock evolving along the z-axis. The design of the holographic plate involves three types of 3D holograms. The two hands of the clock are designed to rotate in opposite directions with different

angular speeds along the z-axis, while the outer frame remains in focus over an extended depth of view (for the details of the hologram design, see Appendix B.3). Figures 3.8b-d show the designed phase profile (Fig. 3.8b) along with corresponding optical (Fig. 3.8c) and SEM (Fig. 3.8d) images of the nanopost metasurface. The designed amplitude profile is presented in Fig. 3.8e. Optical and SEM images of the fabricated metasurface are shown in Fig. 3.8f and Fig. 3.8g, respectively. The optical images illustrate the substantial difference between the two metasurfaces and indicate that the global distribution of the unit cells is correct. Note that the nanodisks (layer 1) used for amplitude modulation also introduce a phase shift, and thus, the phase profile of the nanopost layer (layer 2) is designed to compensate for this variation.

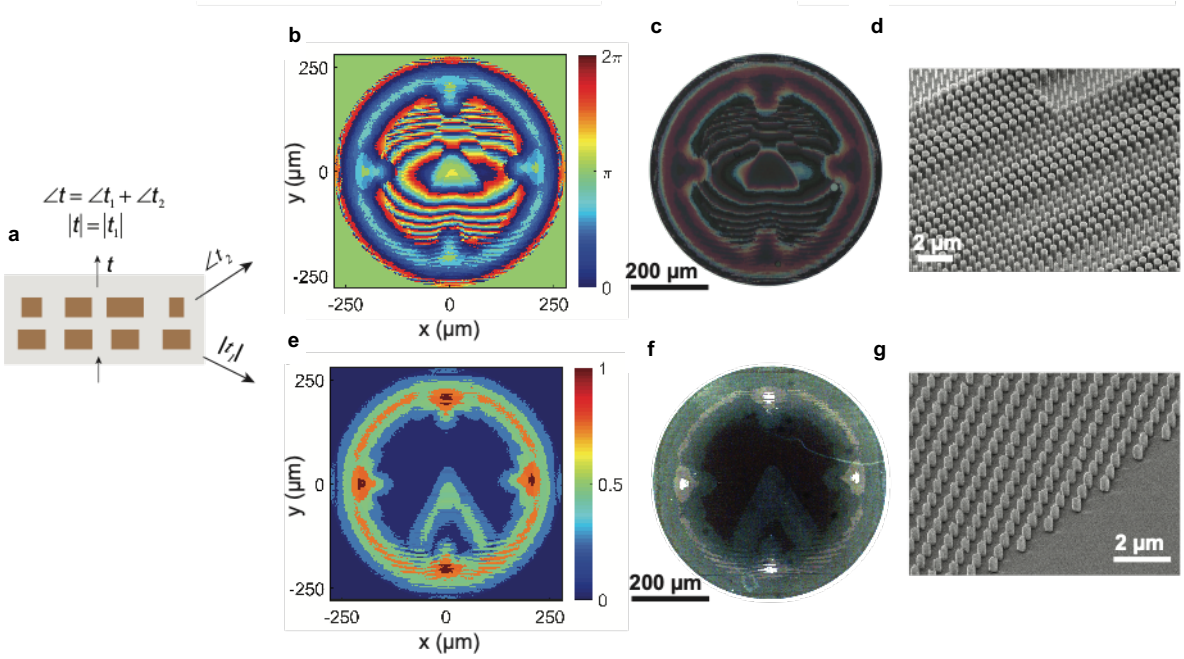

Figure 3.8. Metaoptic for polarization-insensitive phase and amplitude modulation. (a) Schematic of the bilayer metasurface. The bottom layer is used for amplitude modulation ($|t|$), and the top layer is used for phase modulation ($\angle t_2$). The total phase profile of the bilayer metasurface is $\angle t_1 + \angle t_2$. (b, c, d) Designed phase pattern (b), along with an optical microscope image (c) and an SEM image (d) of the top metasurface. (e) The designed amplitude profile. (f, g) Optical (f) and SEM (g) images of the bottom metasurface. All phases and amplitudes are calculated for $\lambda = 1400$ nm.

Figure 3.9a shows the simulated on-axis evolution of the hologram from z = 0.9 mm to z = 2.7 mm based on the designed phase and amplitude patterns from Fig. 3.8b and Fig. 3.8e. To determine the performance of the fabricated device, the metasurface was characterized using a collimated and unpolarized monochromatic beam. The incident wavelength was tuned slightly to 1330 nm to achieve the best performance, and image slices were recorded at various distances using a 20× objective paired with a tube lens (f = 200 mm). The real images acquired at the various on-axis planes are presented in Fig. 3.9b and show good agreement with the simulation. It should be noted that the intensity maps have been slightly saturated to reveal clear outlines in the images.

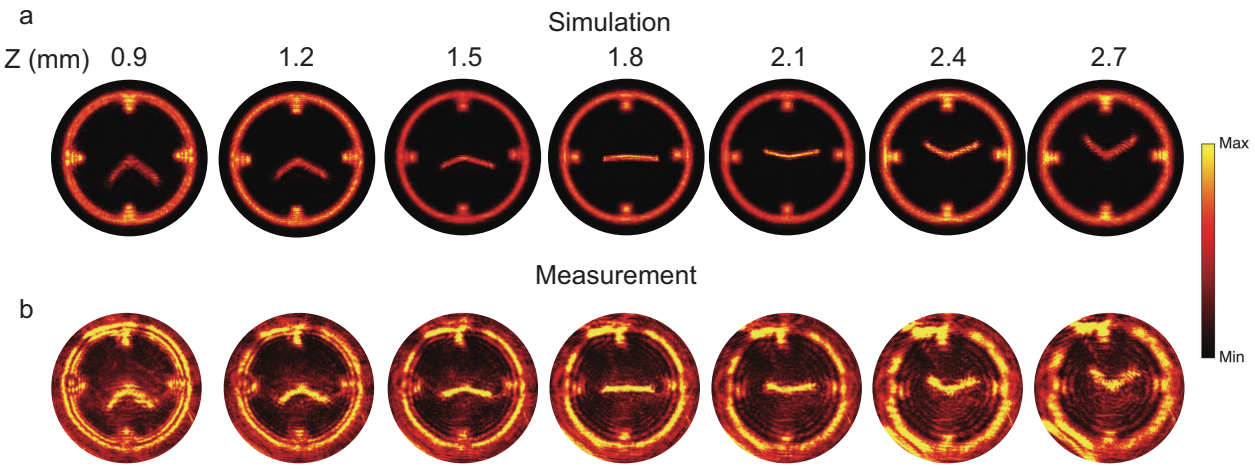

Figure 3.9. Three-dimensional meta-hologram with on-axis evolution. (a, b) Simulated (a) and captured (b) on-axis evolution of the clock hologram under an illumination wavelength of 1330 nm.

3.6 Discussion on the three-dimensional meta-hologram

We attribute the lower contrast and resolution in the measured images mainly due to the strong structural sensitivity of the nanodisk layer, resulting in errors in the amplitude mask (Fig. B7). To illustrate the role of misalignment, we also realized 3D holograms based on two layers of waveguide-based nanopillars (Fig. 3.10a-b), which permit polarization-sensitive amplitude and phase control. The bottom layer consists of a rectangular resonator designed to have a height of

750 nm, a width of 180 nm and a length of 460 nm, so that the phase difference between the long and short axis is equal to π at the wavelength of 1200 nm, serving as a half-wave plate. Under x-polarized incident light, the y-axis transmission coefficient t_{xy} has a form

$$t_{xy} = \sin(2\theta)e^{i\varphi}$$

where the θ is the orientation angle with respect to the x axis, and φ is the phase change along the long axis. As a result, the conversion efficiency of the cross polarization follows a $|\sin(2\theta)|$ dependence while maintaining a constant phase, which is verified in the FDTD simulations of amplitude $|t_{xy}|$ and phase $\angle t_{xy}$ as a function the orientation angle θ in Fig. 3.10b. For the second layer, the cylindrical nanoposts, with the same height and lattice constant, are used for phase-only modulations with high efficiency (Fig. 3.10c-d).

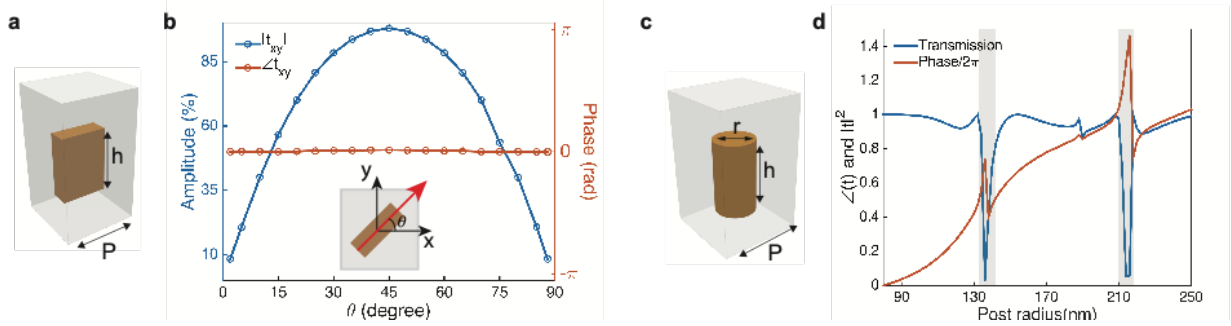

Figure 3.10. Metaoptic for complete amplitude and phase modulation based on linear polarization conversion. (a) Schematic of the first-layer unit cell made of Si rectangular nanopillars. The pillars have a height of 750 nm, a width of 90 nm and a length of 230 nm and are arranged in a square lattice with a period of 600 nm. (b) Simulated cross-polarization conversion amplitude $|t_{xy}|$ and phase $\angle t_{xy}$ as a function of the orientation angle θ with respect to the x axis. (c) A schematic of the unit cell on the second layer. The unit cell is a polarization insensitive cylindrical nanoposts with a height of 750 nm. (d) Simulated transmission and phase as a function of post radius.

In this case, the structural sensitivity is quite low, and as a result, the far-field images which was designed as a helicoid pattern, (Fig. 3.11h-k) show an absence of background noise and good

agreement with the simulation. While better control over the nanodisk size should alleviate the background noise, high-resolution polarization-independent greyscale transmission masks can also be achieved using high-energy beam-sensitive (HEBS) glass[113], [114].

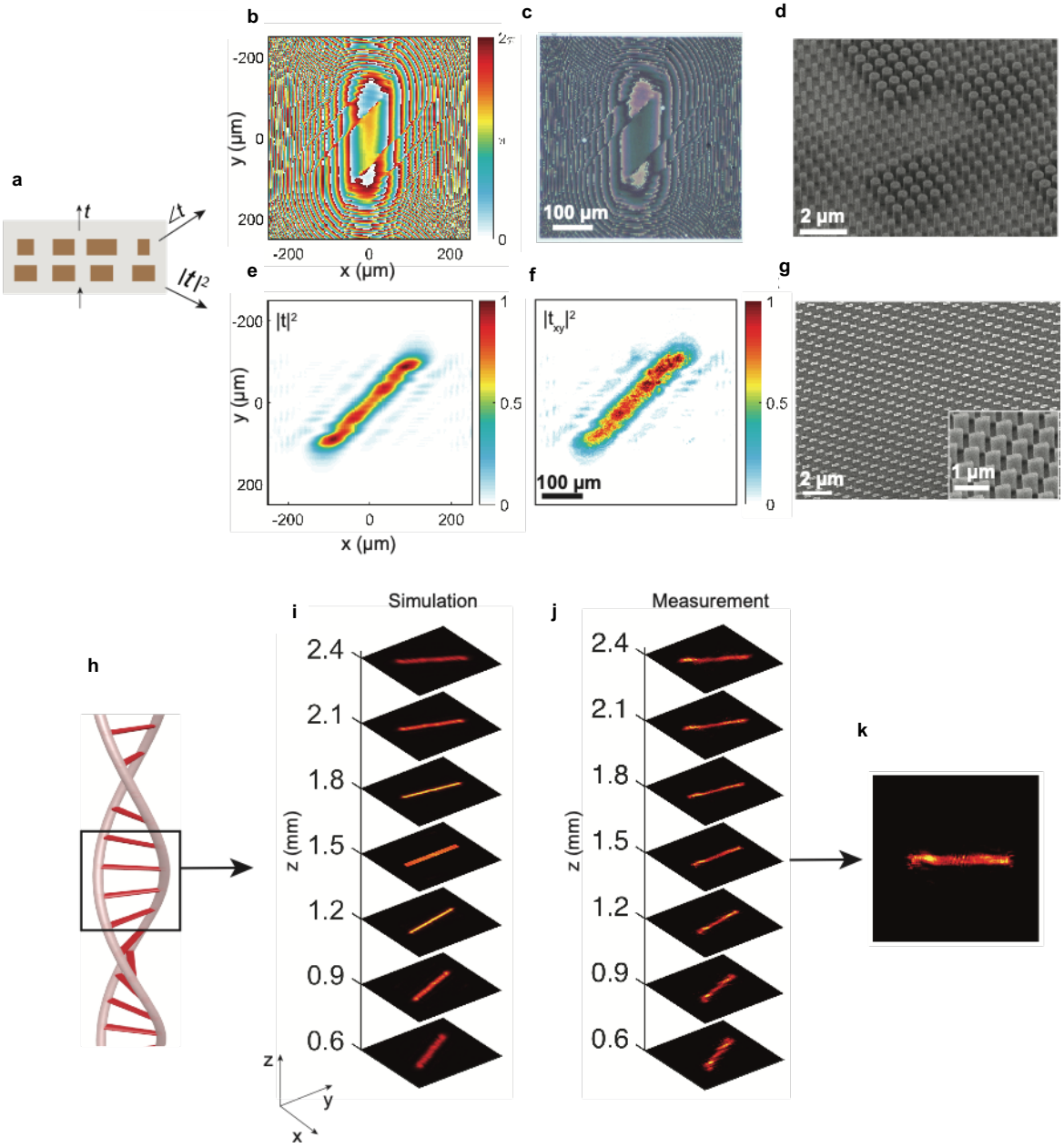

Figure 3.11. Three-dimensional helicoid hologram based on linear polarization conversion. (a) Schematic of the bilayer metasurface. The bottom layer is used for amplitude modulation ($|t|$), and the top layer is used for phase modulation ($\angle t$). (b, c, d) The designed phase pattern (b), along with an optical microscope (c) and SEM image (d) of the fabricated metasurface. (e, f, g) The bottom metasurface layer for amplitude modulation. (e) Simulated amplitude map and the (f)

experimental polarization conversion map $|t_{xy}|^2$. The SEM image of the bottom layer is shown (g). (h-k) (h) A schematic of the 3D hologram with on-axis rotation. The metasurface is designed to show a portion of the helicoid image ranging from z=0.6 mm to z=2.4 mm. (i, j) Simulated (i) and measured (j) on-axis evolvement of the hologram. In the measurement, two orthogonal polarizers were used before and after the device. (k) Measured image at z=1.5 mm, showing the absence of speckle noise.

3.7 Conclusion

In conclusion, we have demonstrated a bilayer metasurface architecture with various combinations of unit cells to increase the available design space for metaoptics. This approach can be further extended using other sets of unit cell geometries to achieve independent control over other combinations of properties (Fig. B5). Metasurfaces sensitive to the angle of incidence[9] could also be incorporated into the platform for applications such as holographic storage and augmented reality displays. While we have combined independent metasurfaces here, the proposed fabrication techniques can also be utilized to prepare more complex metaoptics with interacting layers, including topology-optimized devices[67] and bianisotropic metasurfaces[103], [104]. Further improvements in performance are also expected if design optimization methods[64], [70], [71], [73] are employed.

Chapter 4

Flat Optics for Image Differentiation

4.1 Introduction

In chapter 2 and 3, we have shown that metasurfaces can be promising for reducing the thickness of conventional optical elements for certain applications. In this chapter, we extend such concept beyond wavefront shaping to nonlocal functionality. By exploring a flat optics with tailored dispersion in momentum space, we demonstrate applications for optical analog image processing in a fast, energy-efficient and compact fashion[115].

Recently, imaging processing have become a critical and rapidly advancing technology for various science and engineering disciplines with ever more complex digital tools opening the door for new avenues in biological imaging, 3D reconstruction, and autonomous cars. Edge-based enhancement[116], [117] is particularly useful for data compression[118], [119], object inspection[120], microscopy[121]–[123] and general machine vision[124]. Edge-based enhancement is accomplished using spatial differentiation that can be based on either electronic or optical architectures. While digital circuits are able to perform complex data processing there are limitations due to computation speed and power consumption. Optical analog computation[125], with the ability to process information directly using the optical signal, provides an alternative approach to perform large-scale and real-time data processing with minimal, if any, power consumption.

Traditionally, analog image differentiation has been performed using Fourier methods based on lenses and filter systems. However, the use of multiple conventional lenses, such as those found in 4*f* Fourier filtering, results in a large form factor which is not compatible with compact

integrated systems. One option for significantly reducing the optical system size is to employ nanophotonic materials such as metasurfaces[126] and photonic crystals[127] for optical image processing. For instance, it has been shown that multiple metasurfaces can be used to perform a range of mathematical operations[128] and there have been several theoretical proposals for image differentiation using single layer nanophotonic materials[91], [92], [129]. Furthermore, image differentiation has been experimentally demonstrated using photonic crystals[93], the spin hall effect[130], surface plasmon-based devices[90] and Pancharatnam–Berry (PB) phase[131]. However, these past experimental approaches have been restricted to one dimension and some require additional refractive elements (i.e., prisms or lenses) for either plasmon coupling or performing a Fourier transform, which negates the advantage of thin and flat elements.

In this work, we experimentally demonstrate a two-dimensional spatial differentiator that operates in transmission. As shown in Fig. 4.2a, the differentiator consists of a silicon (Si) nanorod photonic crystal that can transform an image, E_{in}, into its second order derivative, $E_{out} = \nabla^2 E_{in}$, allowing for direct imaging of the edges in the image. The use of a 2D photonic crystal allows for differentiation and edge detection in all directions with an NA up to 0.315 and with an experimental resolution smaller than 4 μm. The nanophotonic differentiator is directly integrated into an optical microscope and onto a camera sensor demonstrating the ease at which it can be vertically integrated into existing imaging systems. Furthermore, we demonstrate integration with a metalens for realizing a compact and monolithic image processing system (Fig. 4.1). In all cases, the use of the nanophotonic differentiator allows for a significant reduction in size compared to traditional systems, opening new doors for optical analog image processing in applications involving machine vision.

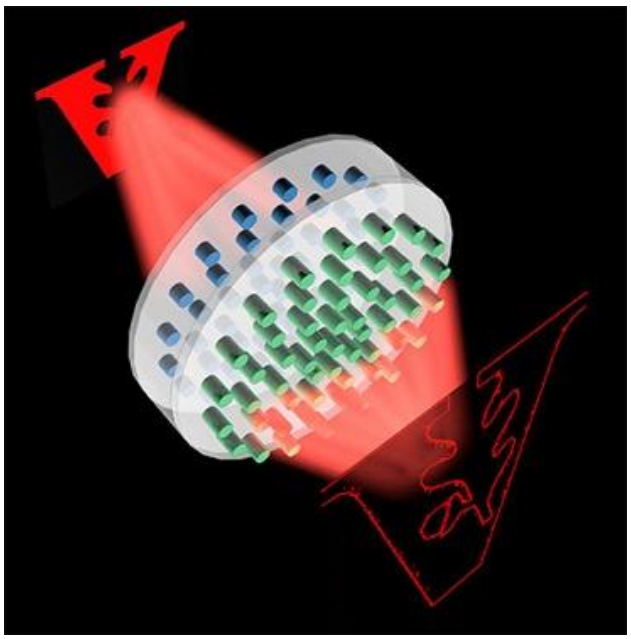

Figure 4.1. Monolithic image processing system. The bilayer system is composed of a metalens and a differentiator based on flat optics.

4.2 Design and working mechanism

In order to perform spatial differentiation, an optical filter or material should act as a Laplacian operator on the transmitted light with an electric field profile given by, $E_{out} = \nabla^2 E_{in}$, where ∇^2 is given by $\frac{\partial^2}{\partial x^2} + \frac{\partial^2}{\partial y^2}$. In this case the optical transfer function $H(k_x, k_y)$ follows the function[132]:

$$H(k_x, k_y) = \begin{bmatrix} H_{ss}(k_x, k_y) & H_{sp}(k_x, k_y) \\ H_{ps}(k_x, k_y) & H_{pp}(k_x, k_y) \end{bmatrix} \tag{1}$$

$$= \begin{bmatrix} c_{ss}(k_x^2 + k_y^2) & c_{sp}(k_x^2 + k_y^2) \\ c_{ps}(k_x^2 + k_y^2) & c_{pp}(k_x^2 + k_y^2) \end{bmatrix}$$

where *s*, *p* on the first and second subscript denote the polarization of the incident and transmitted light, respectively, and c_{sp} and c_{ps} correspond to polarization conversion. To achieve the required

transfer function we employ a photonic crystal slab supporting quasi-guided modes. Unlike modes guided below the light line[133], quasi-guided modes are leaky, propagating in the high-index dielectric slab within the light cone[134], [135]. When the frequency, momentum and symmetry match with the quasi-guided modes, Fano interference occurs between the direct transmission and quasi-guided mode which can lead to near-unity back reflection or transmission[136]–[138]. In recent experimental work Fano interference in 1D photonic crystals has been employed for spatial differentiation[93] and there has been theoretical work on 2D photonic crystals[92] for this purpose though the numerical aperture was limited. Here, we employ a 2D design with a numerical aperture that is large enough for integration into both traditional and nontraditional imaging systems allowing for compact optical analog image processing systems.

In order to realize the required transfer function we employ a 2D photonic crystal composed of cylindrical silicon (Si) nanorods embedded in polymethyl methacrylate (PMMA) on a silicon dioxide (SiO_2) substrate (see Figs. 4.2a,b). The nanorods have a height of 440 nm, diameter of 280 nm, and period of 600 nm. Fig. 4.2c shows the simulated color-coded transmittance $|t(f,\theta)|$ as a function of frequency and incident angle (θ_{air}) along the $\Gamma - \mathrm{X}$ direction ($\varphi = 0°$, where φ is the azimuthal angle in the horizontal plane) for *s*- and *p*-polarization. It's worth noting that no polarization conversions occurs for the transmitted light. At normal incidence, two broad transmission dips are observed at 244 and 268 THz, indicating the presence of two Mie resonances with low quality factor. There is also a bound-state-in-the-continuum (BIC) at the frequency of 249 THz, which is completely decoupled from the free space at the Γ point due to symmetry protection[139], [140]. At oblique incidence, the transmission follows a different trend for *s*- and *p*-polarization. Under *s*-polarization, it is observed that the dipole resonant frequencies remain unchanged as a function of incident angle. The invariant resonances results in

no transmitted light for *s*-polarized input. Due to mirror symmetry of the photonic crystal with respect to the horizontal plane ($z = 0$), regardless of incident polarization, there is also no *s*-polarized output based on optical reciprocity, leading to the matrix components $c_{ss}, c_{sp},$ and c_{ps} being zero in equation (1). However, under *p*-polarization the BIC resonance begins to couple to free space, becoming quasi-guided, with a finite lifetime and a Fano resonance results in a rapid change in transmittance as the incident angle becomes larger. We choose the working frequency of 268 THz ($\lambda_0 = 1120$ nm), away from the BIC, to obtain the proper transfer function. The resulting modulation transfer function $|H(k_x)|$ and phase along the $\Gamma - \mathrm{X}$ direction for *p*-polarization are shown in Fig. 4.2d. Importantly, the modulation transfer function has the required quadratic dependence given by, $H(k_x) = c_{pp}k_x^2$, evidenced by a fit to the simulated data. The quadratic curve is a near perfect fit up to an NA (nk_x) of 0.315, which equates to an edge resolution on the scale of 2.17 μm (1.94λ).

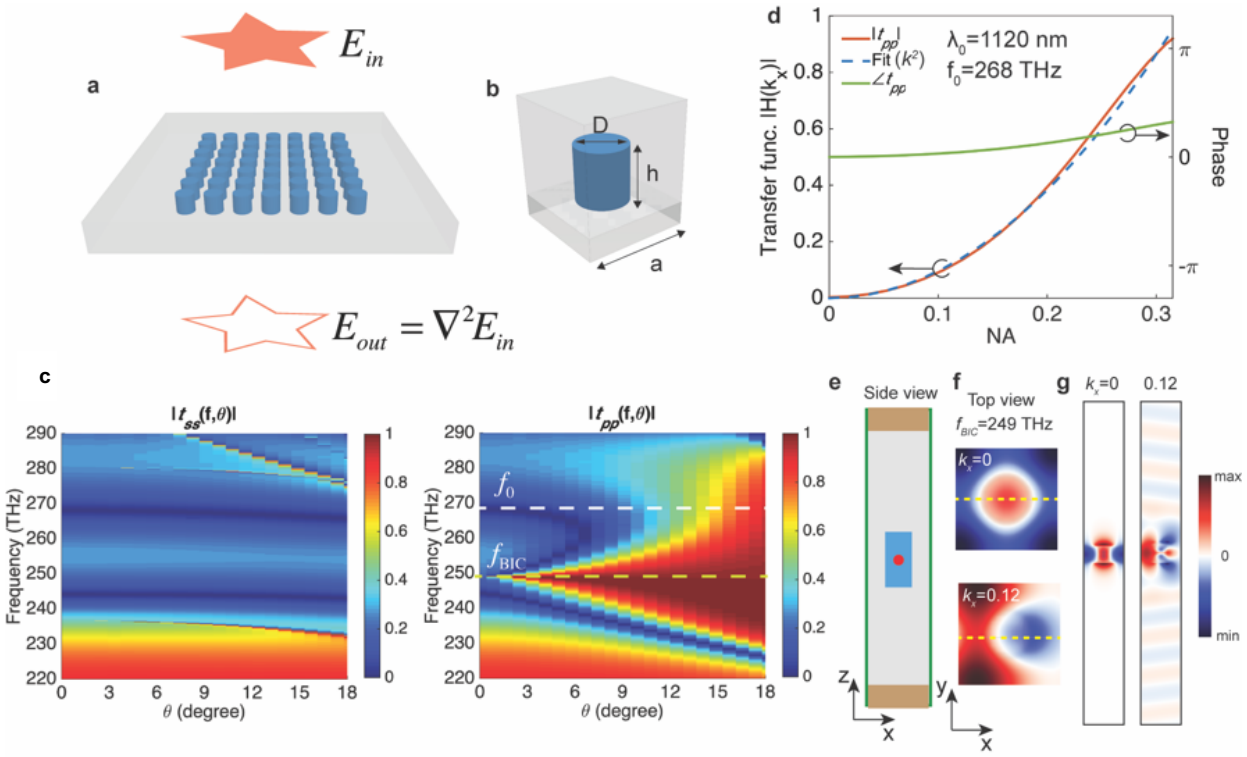

Figure 4.2. Two-dimensional image differentiation using nanophotonic materials. (a) Schematic of a dielectric nanophotonic slab acting as a Laplacian operator that transforms an image, I_{in}, into its second order derivative, $I_{out} = \nabla^2 I_{in}$. (b) Unit cell of the differentiator composed of Si nanorods. The array is embedded in a layer of polymethyl methacrylate (PMMA) on a SiO_2 substrate. (c) Simulated color-coded transmittance $|t(f,\theta)|$ as a function of frequency and incident angle (θ) along the $\Gamma - X$ direction ($\varphi = 0°$) for *s* and *p* polarization. (d) Optical transfer function $H(k_x)$ along the $\Gamma - X$ direction for *p* polarization at $\lambda_0 = 1120$ nm, and the quadratic fitting in the form of $c_{pp}k_x^2$. (e) Schematic of the simulation model for the BIC and leaky modes. An electric dipole E_z (red dot) was placed within the slab as an excitation source. (f) Top view of the E_z field profiles showing the excitation of the BIC (top) and leaky mode (bottom) at $k_x = 0$ and $0.12\ (2\pi/a)$, respectively. The symmetry plane is denoted by the yellow dashed line ($y = 0$). (g) Side view of E_z field distributions for the BIC ($k_x = 0$) and leaky mode at $k_x = 0.12\ (2\pi/a)$.

To balance the roles of NA, accuracy of the transfer function, and transmittance for image differentiation, we define the differentiation efficiency (η) as the square of transfer function ($|H(k)|^2$) at the maximum spatial frequencies that can be fitted to the desirable mathematical function (e.g. Laplacian for this work). In this regard, the efficiency can be as high as 81% at an NA of 0.315. Since the maximum NA also depends on the fitting accuracy, we can also expand the maximum fitted NA to 0.326 to achieve an efficiency of 90%, at a slight expense to the accuracy (see the summary of previous works in the Table 1 below and Fig. C4).

Table 1. Summary of past work on image differentiators

References	NA	Operation	$\lvert H(k_{max})\rvert$	Efficiency η
Zhu *et al*[1].	<0.01	1D, 1st order	~40%	~16%
Cordaro *et al*[2].	0.35	1D, 2nd order	~100%	~100%
Guo *et al*[3].	0.013	2D, 2nd order	<30%	<9%
This work	0.32	2D, 2nd order	95%	90%

1. Zhu, T. *et al.* Plasmonic computing of spatial differentiation. *Nat. Commun.* **8**, 1–6 (2017).
2. Cordaro, A. *et al.* High-index dielectric metasurfaces performing mathematical operations. (2019).
3. Guo, C., Xiao, M., Minkov, M., Shi, Y. & Fan, S. Photonic crystal slab Laplace operator for image differentiation. *Optica* **5**, 251 (2018).

To better understand the polarization dependence, we examine the profile of the BIC mode

as a function of in-plane wave vector. The structure was modeled using a finite difference time domain (FDTD) solver (MEEP[101]) by placing an electric dipole, E_z (red dot), within the slab at the BIC frequency of 249 THz and the in-plane wave vector was swept long the $\Gamma - \mathrm{X}$ direction, as shown in Fig. 4.2e.. The top view of E_z field profiles are shown in Fig. 4.2f, indicating the excitation of a vertical electric dipole. For a system with a sub-diffractional period, the array of dipoles oscillates in-phase supporting in-plane radiation completely decoupled from free space. Away from the Γ point, this state starts to become quasi-guided and radiative as the symmetry is no longer protected, as can be seen from the sideview of the E_z field distributions (Fig. 4.2g). Along the $\Gamma - \mathrm{X}$ direction, odd and even modes, with respect to the vertical mirror plane ($\mathrm{y} = 0$), can be excited by the *s*- and *p*-components, respectively. Based on symmetry considerations, the photonic crystal slab only couples to free-space modes of the same type of symmetry[139], [141]. Thus, the quasi-guided mode, which possess an even symmetry (Fig. 4.2f), can only be excited by *p*-polarization, leading to an angularly-dependent transmission for *p*-polarization while remaining reflective for *s*-polarization.

To verify the excitation of the quasi-guided mode as the primary mechanism for the angular-dependent transmission, we have used a quasi-analytical coupled mode model to calculate the transmission amplitude of the differentiator. This model is based on the interference between a direct transmission pathway and an indirect pathway which is due to the quasi-guided mode[134]. In our case, we further expand the traditional coupled mode theory[134] to express the transmission coefficient as a function of incident angle:

$$t(\omega, k) = t_d + f\frac{\gamma(k)}{i\left(\omega - \omega_{QG}\right) + \gamma(k)} \tag{1}$$

where t_d is the direct transmission coefficient and ω is the incident frequency. ω_{QG} and $\gamma(k)$ are

the center frequency and radiative linewidth of the quasi-guided mode, respectively. This quasi-guided mode becomes a BIC at normal incidence with $\gamma(k) = 0$. f is the complex amplitude constrained by energy conservation and time-reversal symmetry[134], which can be expressed as[134]:

$$f = -(t_d \pm r_d) \tag{2}$$

where r_d is the direct reflection coefficient. t_d and r_d are calculated using full-wave simulations at normal incidence where the linewidth ($\gamma(k)$) goes to zero. As illustrated in the inset of Fig. 4.4d, t_d is near-zero at normal incidence over the frequency band of interest due to the presence of Mie resonances, which is further illustrated in the *s*-polarization transmission plot in the manuscript (Fig. 4.2c). In our model, we assume that t_d remains near-zero as a function of in-plane wavevector (k). While we cannot verify this assumption directly we will see that there is excellent agreement between the analytical and full-wave results. This assumption is also supported by the fact that transmission for *s*-polarization does remain near-zero as a function of k (Fig. 4.2c).

Next, to extract $\gamma(k)$ we can use the quality factor, $Q(k)$, which is retrieved using the Harminv tool of Meep[101], [141] by directly exciting the quasi-guided modes inside the photonic crystal as a function of k. The radiative linewidth $\gamma(k)$ can then be determined using $({}^{\omega_{QG}}/_{Q(k)})$. Fig. 4.3a shows the band structure obtained from Meep, indicating an invariant position of ω_{QG} over an NA ($nsin(\theta)$) of 0.12. Fig. 4.3b shows the retrieved $Q(k)$ and $\gamma(k)$ over the NA ranging from 0 to 0.12, beyond which the $Q(k)$ is below the lifetime threshold of Harminv and becomes intractable. We note that the extracted quality factors are far greater than what is achievable with a Mie resonance in a cylinder verifying that this mode must be quasi-guided.

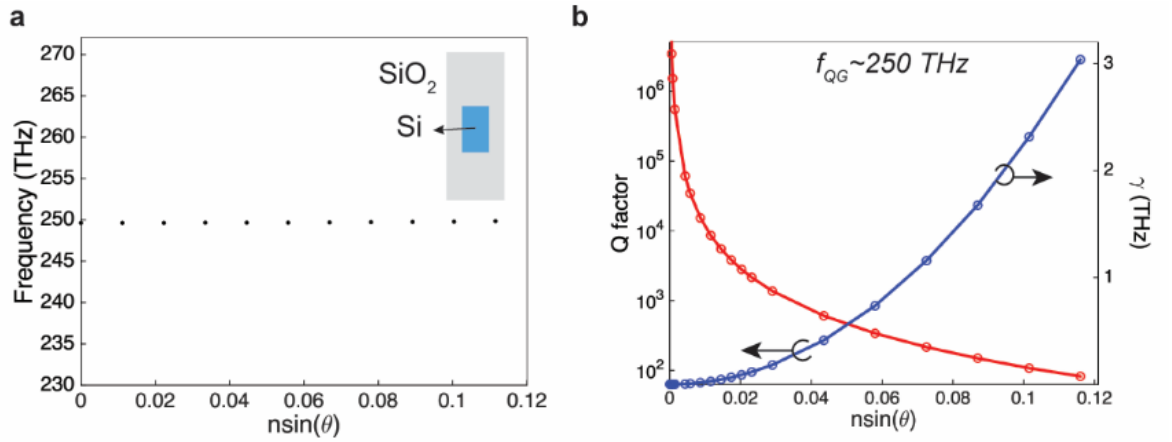

Figure 4.3. Quasi-guided mode quality factor and effect on transfer function. (a) Band structure along the $\Gamma - X$ direction obtained from FDTD. The inset corresponds to a schematic of a unit cell. The Si rod is embedded in a uniform layer of SiO_2. (b) Retrieved Q factor and radiative linewidth (γ) as a function of NA ($nsin(\theta)$).

Based on equation (1), the transfer function at the working frequency (f_0 in Fig. 4.4a) can be plotted as a function of angle using the retrieved $\gamma(k)$ which is shown in Fig. 4.4b with a comparison to the full-wave solution. The transmission spectra as a function of frequency and incident angle are provided in Fig. 4.4c with the full-wave comparison in Fig. 4.4d. From Fig. 4.4b-d, it can be observed that the theoretical predictions agree well with the full-wave simulations, indicating the excitation of the quasi-guided modes as the primary mechanism responsible for the angularly-dependent transmission. The theoretical calculation was only performed over a small angle range (~6.67°) due to the intractable Q factor owing to strongly radiative modes. However, due to the smooth variation of transmission beyond 7° and across the frequency range of interest (Fig. 4.4a) we believe that it's reasonable to assume that the quasi-guided modes remain the primary mechanism even at higher angles.

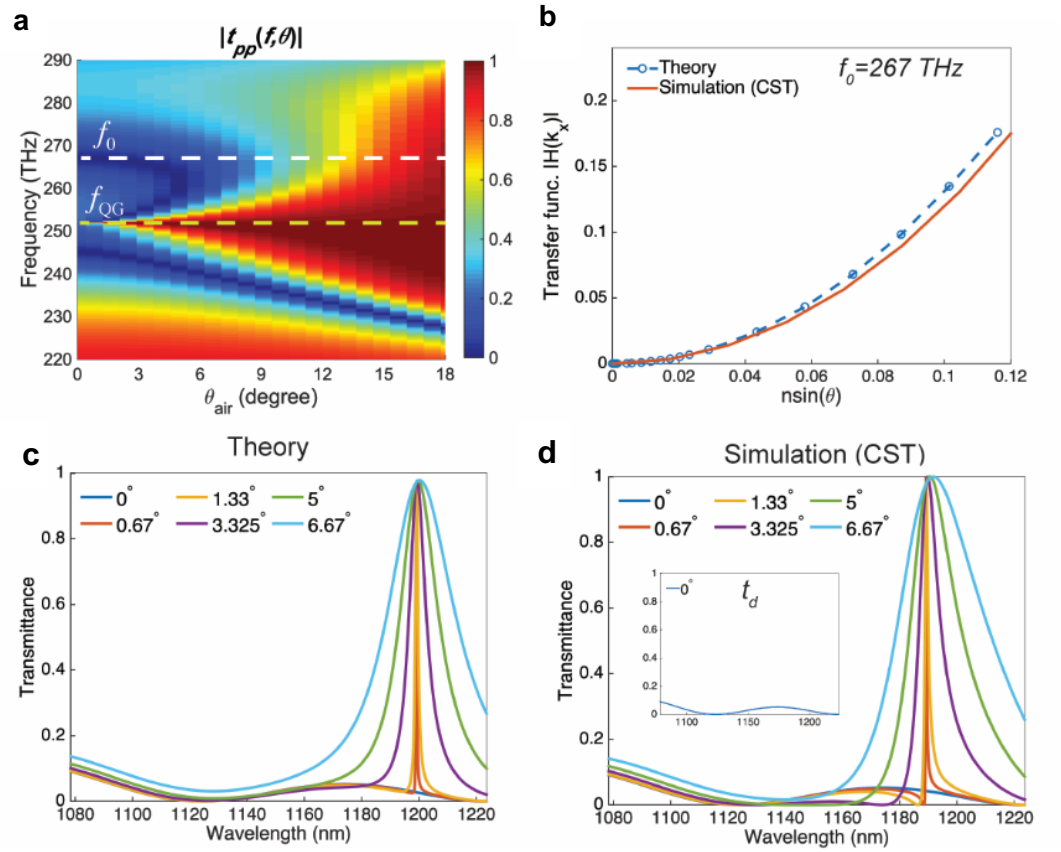

Figure 4.4. Quasi-guided mode quality factor and effect on transfer function. (a) Simulated transmission amplitude $|t(f,\theta)|$ as a function of frequency and incident angle (θ_{air}) for *p*-polarization. Note that the use of a uniform SiO_2 cladding layer results in a slight shift in the quasi-guided mode and working-frequencies. (b) Modulation transfer function at the working frequency (f_0) calculated by theory and full-wave simulation. (c-d) Transmission spectra calculated by theory (c) and full-wave simulation (d). The inset in (d) corresponds to the transmission at normal incidence.

4.3 Experimental realization

In order to experimentally validate the design, we fabricated a 200×200 μm^2 differentiator using electron beam lithography (EBL) in conjunction with reactive ion etching (RIE). A scanning electron microscope (SEM) image of the fabricated device is shown in Fig. 4.5a. The simulated transmission spectra are presented in Fig. 4.5b and Fig. 4.5c for *s* and *p* polarization, respectively and a schematic of the measurement setup is shown in Fig. 4.5d. To acquire angle dependent transmission measurements the sample was mounted on a rotation stage

and imaged through a magnification system composed of an objective paired with a tube lens. Fig. 4.5e and f show the measured transmission spectra at various incident angles under *s* and *p* polarization, respectively. The incident light is along the $\Gamma - X$ direction with the angles ranging from 0° to 24°. The trend and shape of the measured spectra are in good agreement with the simulation.

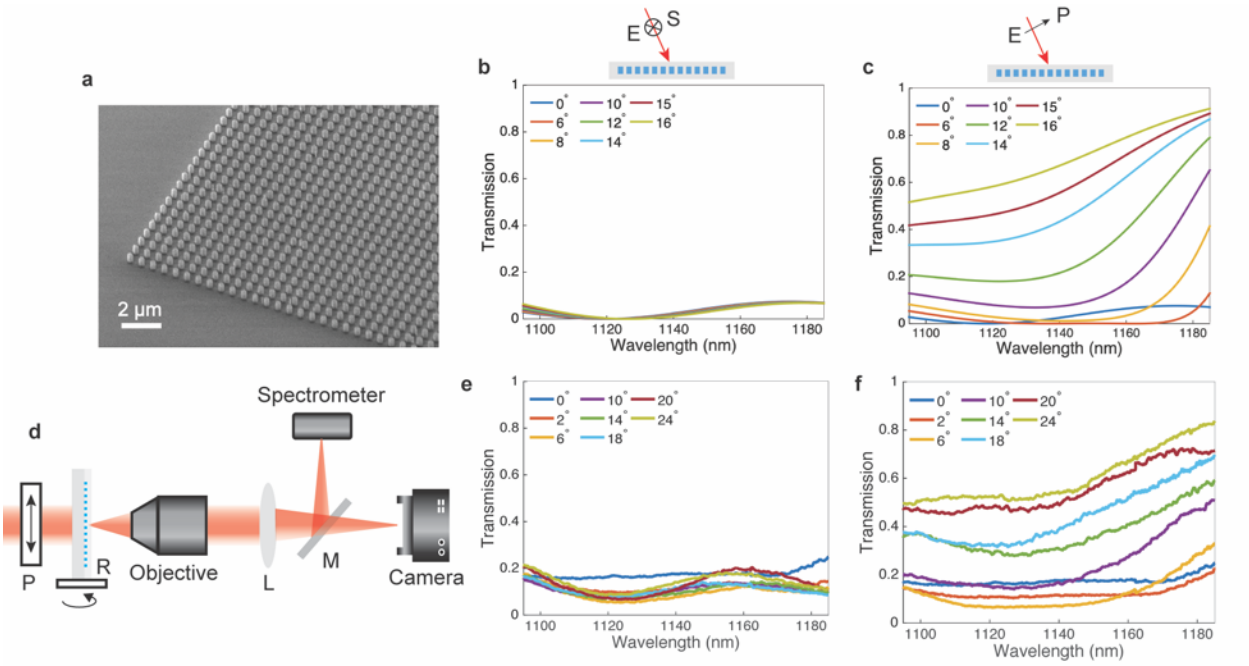

Figure 4.5. Fabrication and characterization of the nanophotonic spatial differentiator. (a) SEM image of the fabricated Si photonic crystal. (b-c) Simulated transmission spectra along the $\Gamma - X$ direction for *p* (c) and *s* (d) polarization. (d) Experimental setup for measuring the transmission spectra at various angles. P, polarizer; R, rotation stage; L, tube lens (f=200 mm); M, flip mirror. (e-f) Measured transmission spectra for *p* (c) and *s* (d) polarized incident light.

To map the entire transfer function in *k*-space, we carried out Fourier plane imaging of the device. The nanophotonic differentiator was illuminated by unpolarized light at a wavelength of 1120 nm and a 50X objective (NA=0.42) was used as a condenser with the Fourier images acquired in the back focal plane of a 20X objective (NA=0.4). Fig. 4.6a and b show the measured back focal plane imaging, along with the transfer function $|H(k)|$ along the $\varphi = 0^\circ$ $(\Gamma - X)$ and $\varphi = 45^\circ$ azimuthal plane $(\Gamma - M)$. Along the $\Gamma - X$ direction, the transfer function matches with the fitted

parabolic curve over an NA of 0.305. While the Fourier imaging indicates a non-isotropic transfer function, the Laplacian transform at $\varphi = 45°$ can still be fitted with a quadratic function up to an NA of 0.28.

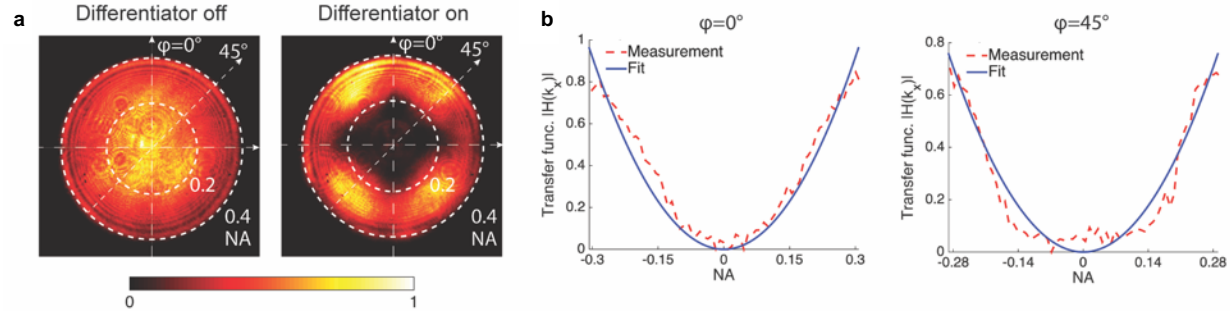

Figure 4.6. Back focal plane imaging. (a) Measured back focal plane images without and with the nanophotonic differentiator. (b) Extracted 1D modulated transfer function along φ =0° and 45°.

4.4 Resolution characterization

To experimentally quantify the resolution, we used the nanophotonic differentiator to detect the edges of 1951 USAF resolution test chart. A schematic of the imaging setup is shown in Fig. 4.7a. The test chart was illuminated using unpolarized and collimated light with a wavelength of 1120 nm. Different from previous experimental work[93], in this case no polarizers are needed necessary to implement image differentiation which further reduces the system footprint and complexity. The differentiator was placed directly in the front of the test chart which was then imaged through a magnification system comprising an objective paired with a tube lens and a near-infrared camera. The imaging results without the differentiator for element sizes ranging from 30 μm to 4 μm are shown in Fig. 4.7b. Fig. 4.7c shows the images of the test chart after being passed through the differentiator. The edges of the micron-scale elements are clearly revealed along both horizontal and vertical directions, which indicates 2D spatial differentiation with a resolution higher than 4 μm. Fig. 4.7d shows the horizontal-cut intensity distributions

through the differentiated images in 3c (white dotted line), compared to the 2nd order derivative based on the Laplacian-of-Gaussian filter. Due to the nature of 2nd order derivative, two closely-spaced peaks are formed around each edge, which can be observed from both the calculation and measurement.

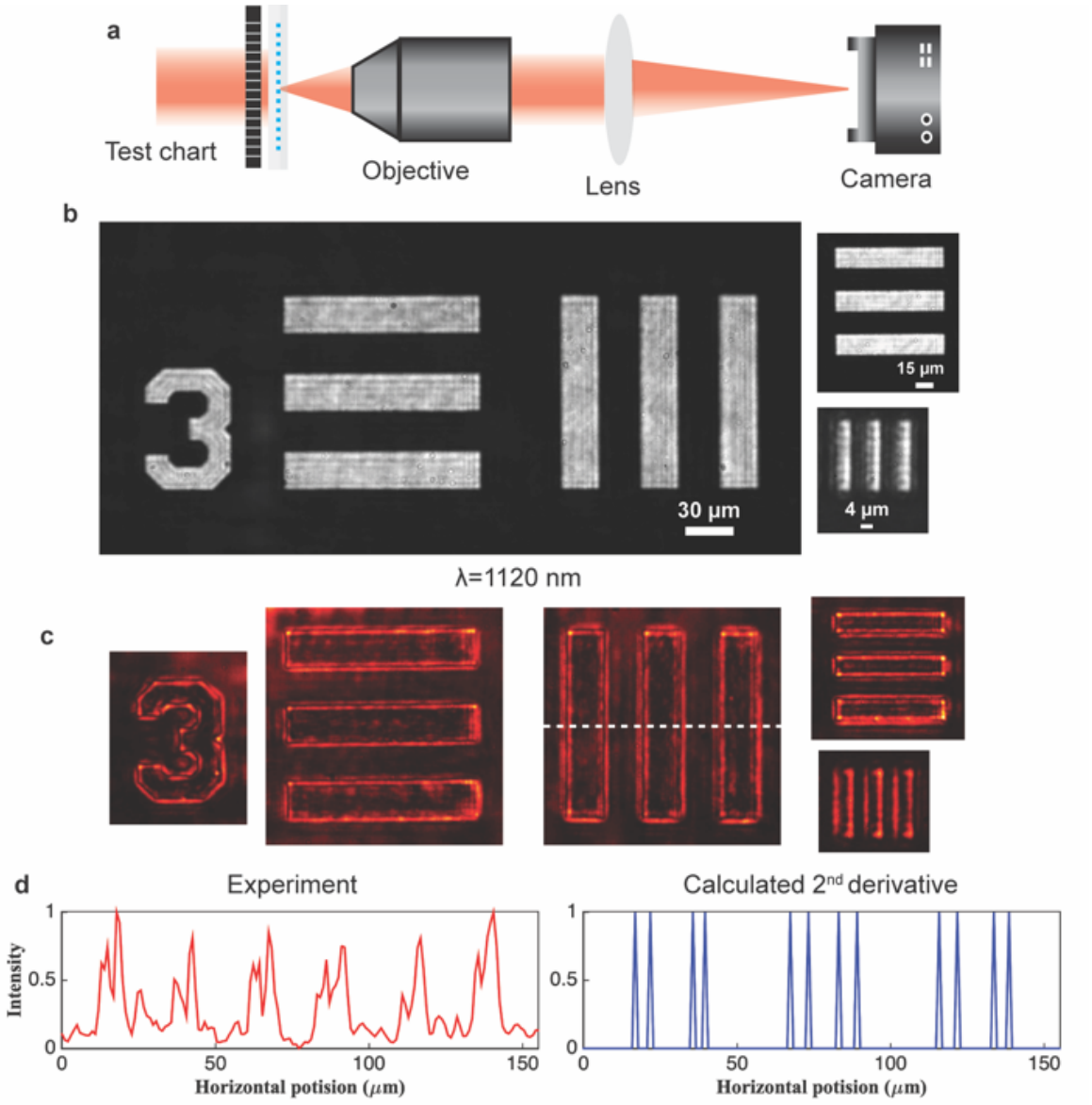

Figure 4.7. Differentiator resolution characterization. (a) A schematic of the imaging setup. The nanophotonic differentiator is placed in front of a standard 1951 USAF test chart and the targets are magnified through an objective paired with a tube lens. (b-c) Imaging results of the target without (b) and with (c) the differentiator. (d) Horizontal cut through the image in 3c (white

dotted line), compared to the calculated 2nd order derivative calculated by the Laplacian of Gaussian filter.

It's also important to note that the differentiator can operate over a relatively broadband due to the low-quality factor resonance away from the BIC state (see details of modulation transfer functions at other wavelengths in Appendix Fig. C5). While the differentiator is not an ideal Laplacian away from the designed wavelength the images in Fig. 4.8e indicate that it can still operate for edge discrimination across a bandwidth from 1100 and 1180 nm.

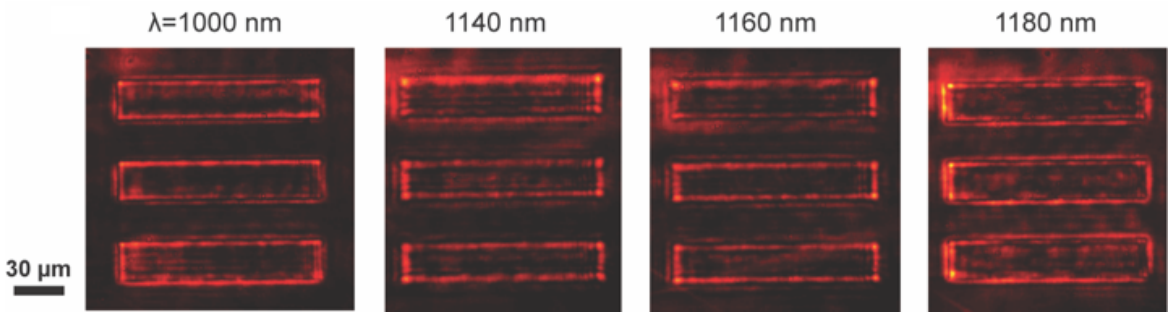

Figure 4.8. Wide-band operation. Edge detection results at different wavelengths ranging from $\lambda_0 = 1100$ nm to 1180 nm.

4.5 Integration with Optical Microscope

One of the primary benefit of flat optics is the ability to vertically integrate them with traditional optical systems. To demonstrate the potential of this approach, we built an edge detection microscope by integrating the image differentiator with a commercial optical microscope (Axio Vert.A1). In this case, the nanophotonic differentiator was redesigned for a wavelength of 740 nm using pillars with a diameter of 180 nm, a period of 385 nm, and a height of 280 nm. Fig. 4.9 shows a schematic of the microscope setup. The differentiator has a size of 3.5×3.5 mm^2 and is placed below the sample stage directly on top of the microscope objective (10X). An unpolarized

monochromatic laser ($\lambda_0 = 740$ nm) was used as the light source incident from the top and imaged on a CCD (uEye).

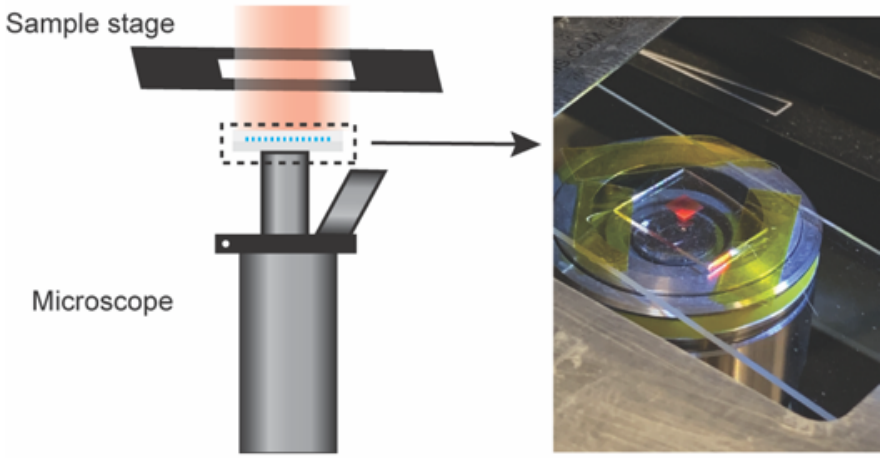

Figure 4.9. Edge detection microscope at visible frequencies. A schematic of the edge detection microscope. The spatial differentiator is redesigned at the wavelength of $\lambda_0 = 740$ nm and fabricated at a size of 3.5×3.5 mm^2, which is directly integrated with a commercial inverted optical microscope (Axio Vert.A1).

Three types of biological cells were used as the imaging specimen. Fig. 4.10a-c show the imaging and edge detection results of onion epidermis (a), pumpkin stem (b), pig motor nerve (c). The bright-field images were obtained at a wavelength of $\lambda = 900$ nm, which is away from the quasi-guided resonance. It can be seen that the shapes and boundaries of cells are less discernable due to the transparent nature of the specimen. By switching to the working wavelength of $\lambda_0 = 740$ nm, we observe clear and high-contrast cell boundaries shown on the right. This edge enhancement is similar to dark-field microscopy but without the use of complex components such as a condenser annulus, which has to be aligned in the optical pathway, resulting in significantly reduced system complexity.

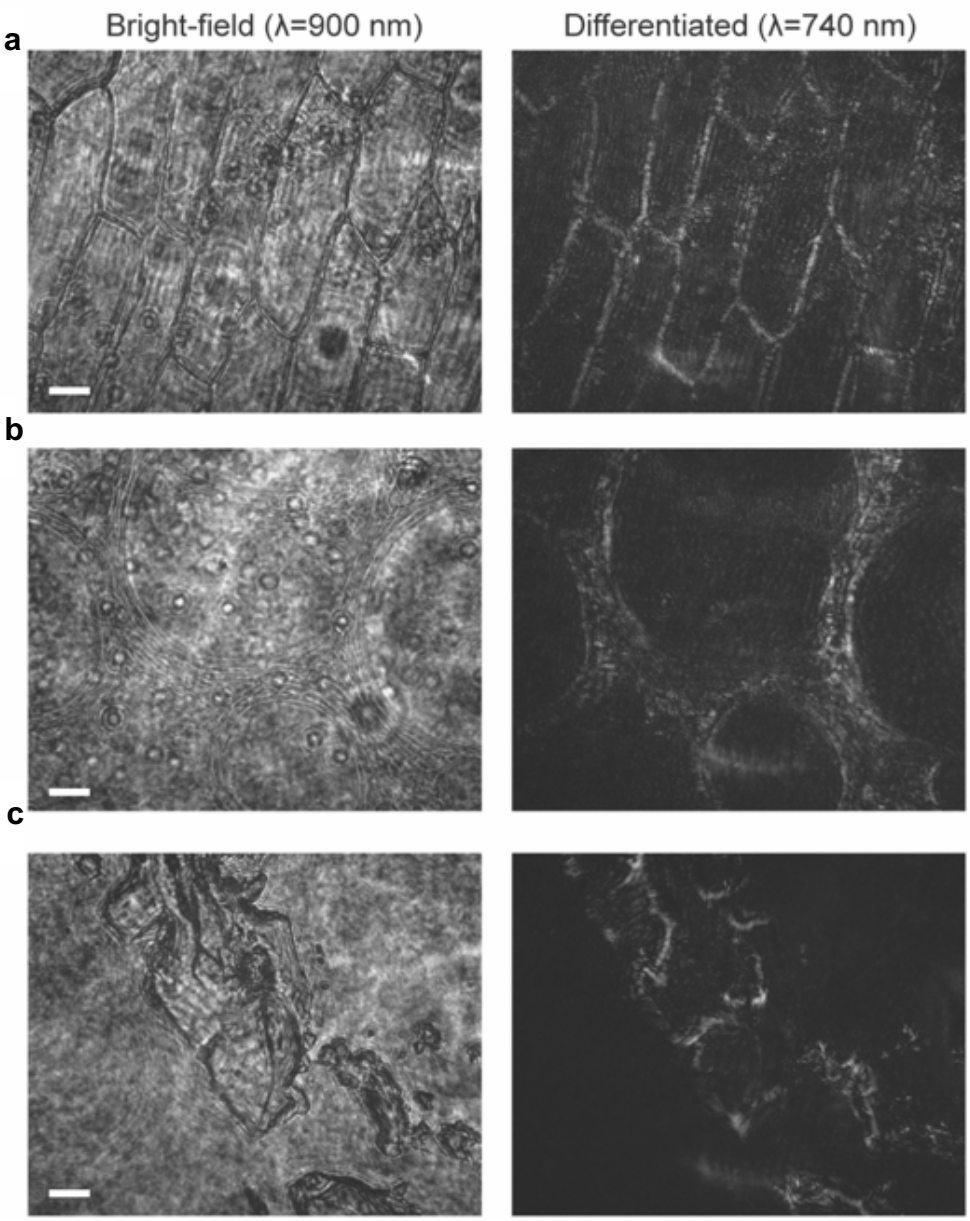

Figure 4.10. Imaging and edge detection on biological samples. (a-c) Imaging and edge detection results of three types of biological cell samples. (b), onion epidermis; (c), pumpkin stem; (d), pig motor nerve. Images on the left are obtained at a wavelength of $\lambda = 900$ nm which is away from the resonant frequency and the images on the right correspond to the results at the working wavelength of $\lambda_0 = 740$ nm. Scale bar: 50 μm.

4.6 Large-scale Differentiator for integration with camera sensor

Another way in which the differentiator can be used in traditional optical systems is integration onto a camera sensor. In this case, and in most practical machine vision applications,

fabrication at much larger scales is necessary. One potential avenue for scale-up is to employ self-assembly based nanosphere lithography which takes advantage of the inherent periodicity and cylindrical unit cell geometry employed here. We have recently employed this method for realizing large area reflectors and Fig. 4.11a shows a schematic flowchart of this fabrication process[142]. A wafer with a 480 nm thick layer of Si on SiO_2 was titled at 10° and placed at the bottom of the Teflon bath. The densely packed hexagonal nanospheres were transferred to the wafer by slowly draining the bath. The nanospheres were then downscaled using an O_2 plasma and used as an etch mask during reactive ion etching to define the Si rods.

To investigate the feasibility of this technique for realizing the differentiator we redesigned the device for an operational wavelength of 1450 nm, which corresponds to a rod diameter of 340 nm, height of 480 nm, and a hexagonal lattice with a period of 740 nm. This redesign was necessary to match the periodicity with the size of commercially available nanospheres. The fabrication technique, outlined in detail in the Appendix C.2, involves using an array of self-assembled nanospheres as an etch mask for the photonic crystal. Fig. 4.11b shows the optical image of a fabricated ~1 cm x 1 cm size image differentiator. The color variation corresponds to different grain orientations which does not affect the transmission at different incident angles (Fig. C7). The SEM images in Fig. 4.11c indicate high quality Si resonators and a well-defined hexagonal lattice over a large area (Appendix, Fig. C2).

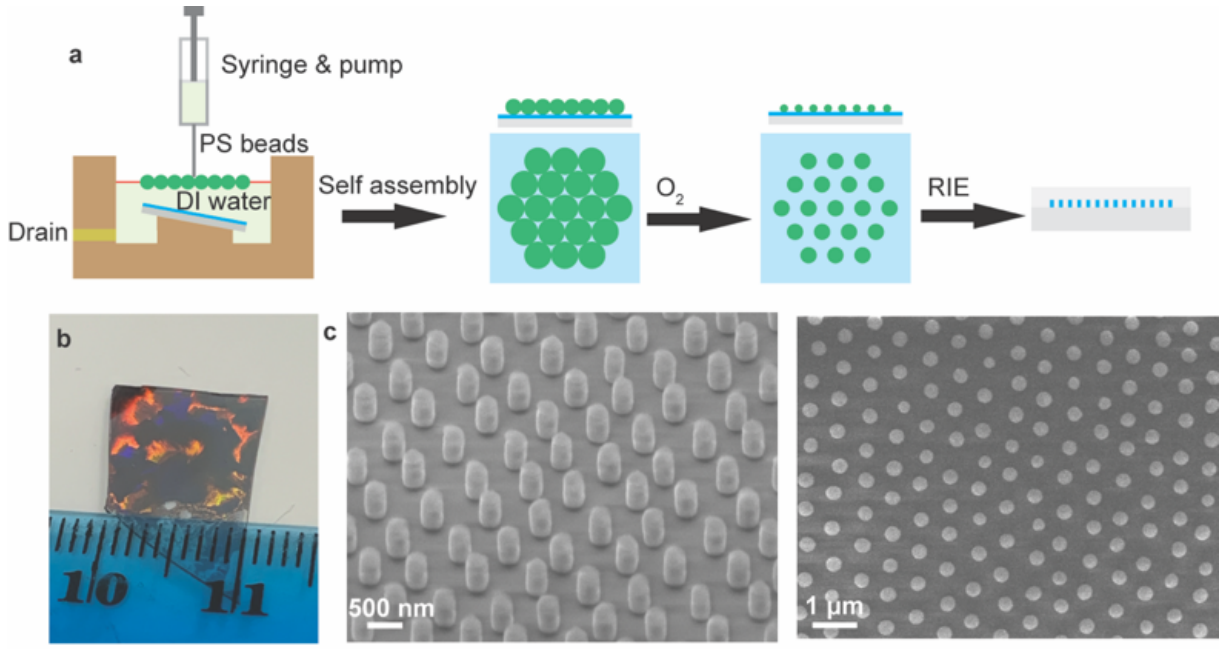

Figure 4.11. Large-scale image differentiator using nanosphere lithography. (a) Flowchart of the fabrication process. A monolayer of nanospheres (diameter of 740 nm) were formed at the water-air interface of a bath and then transferred to a tilted substrate with a Si film (thickness of 480 nm), resulting in a densely-packed nanospheres arranged in a hexagonal lattice. The nanospheres were then downsized and used as a dry etch mask for defining the Si nanostructures. (b) Optical image of a centimeter-scale spatial differentiator. (c) SEM images of the Si rods. The device is designed at a wavelength $\lambda_0 = 1450$ nm.

In order to mimic a configuration that may be found in a machine vision application, the large-scale spatial differentiator was placed directly in front of a NIR camera detector, after the imaging lens, as shown in Fig. 4.12a. For imaging we used transparent centimeter-size plastic flower molds (Figs. 4.12b,d) as the targets due to their curved surfaces which scatter light at large angles. Figs. 4.12c,e show the imaging results with and without the differentiator for two separate objects. Compared to the bright-field images, the edges of the flowers are clearly revealed when applying the differentiator. While we have not placed the differentiator directly on the sensor in this case, there is nothing that would prevent this in creating a monolithic edge-detecting sensor for machine vision applications.

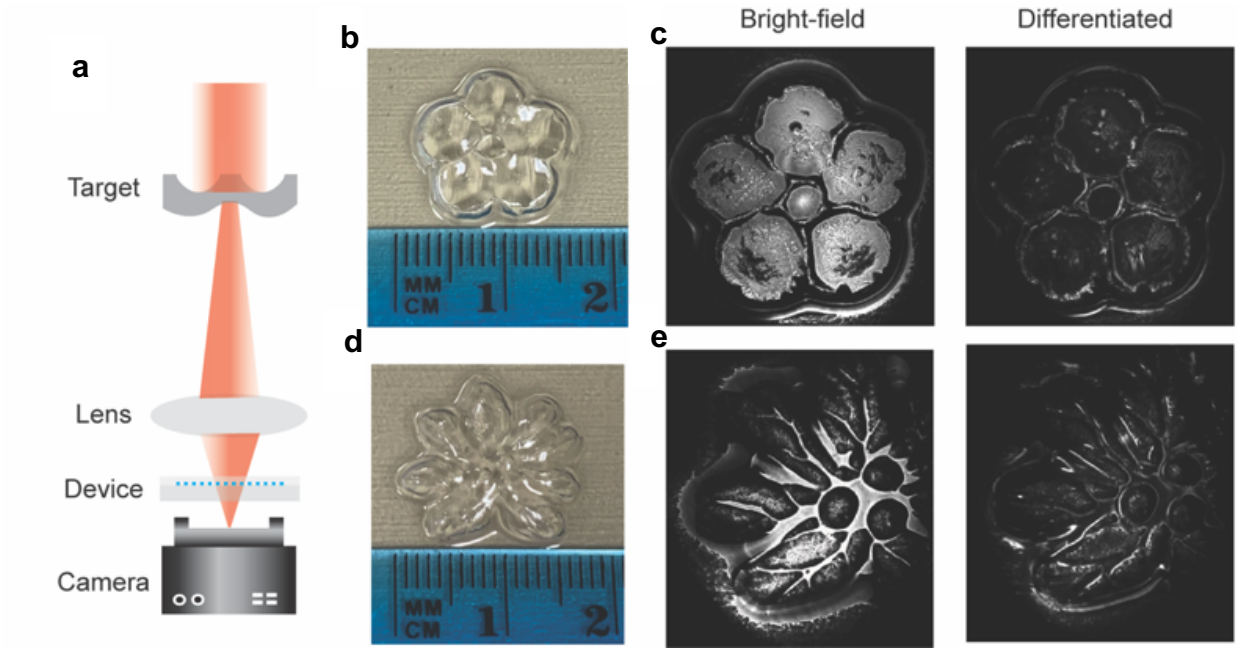

Figure 4.12. Large-scale image differentiator using nanosphere lithography. (a) Flowchart of the fabrication process. A monolayer of nanospheres (diameter of 740 nm) were formed at the water-air interface of a bath and then transferred to a tilted substrate with a Si film (thickness of 480 nm), resulting in a densely-packed nanospheres arranged in a hexagonal lattice. The nanospheres were then downsized and used as a dry etch mask for defining the Si nanostructures. (b) Optical image of a centimeter-scale spatial differentiator. (c) SEM images of the Si rods. The device is designed at a wavelength $\lambda_0 = 1450$ nm. (d) Schematic of the imaging setup. The large-scale device is placed in front of a NIR camera sensor. (e) Optical image of a plastic flower mold which was used a 3D macroscopic imaging target. The size of the object is on the scale of centimeters. (f) Imaging and edge detection results. Images on the left and right correspond to the systems without and with the angular differentiator, respectively. (g-h) The same imaging results on a second target.

4.7 Monolithic compound metaoptic

Lastly, while we have showcased vertical integration with convention optics, the imaging system can be further compacted by employing a metalens as the focusing element for realizing an ultrathin and monolithic image processing system. To create the device we employed multilayer metasurface transfer techniques that we have previously employed for creating doublet lenses[105] and other multilayer metaoptics[143] (see details of fabrication in Appendix C.3 and Fig. C3). Briefly, the metalens and differentiator were designed for operation at λ = 1200 nm and fabricated

on separate wafers with the sizes of $\sim 2 \times 2\ \mathrm{mm}^2$ followed by embedding in polydimethylsiloxane (PDMS). Fig. 4.13a and b show the optical images of the differentiator and metalens, respectively, before transfer. The differentiator layer was then released from the handle wafer and transferred on top of the metalens, forming a compound monolithic element shown in Fig. 4.13c (see details of the fabrication steps in Appendix C.3).

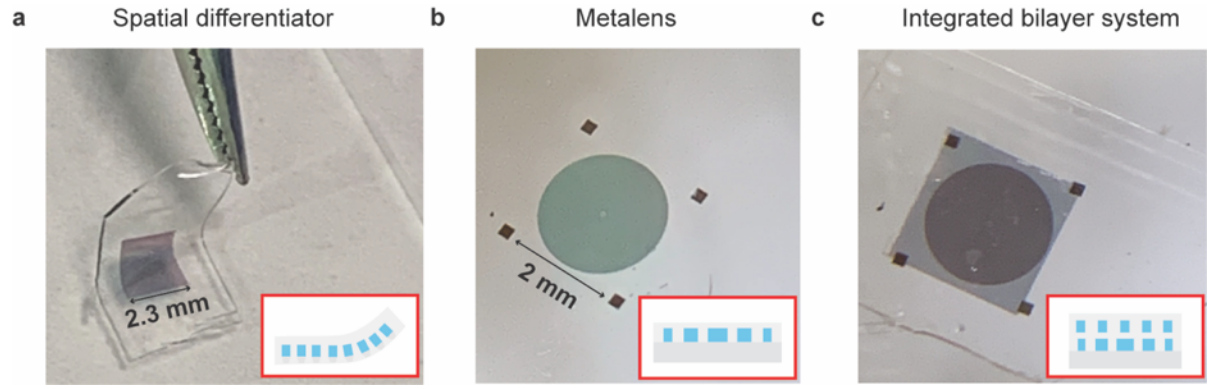

Figure 4.13. Compound metaoptic. (a-c) Optical images of the nanophotonic differentiator (a), metalens (b) and monolithic compound system (c). The insets correspond to schematics of the device cross-sections.

The compound metaoptic was then used as an ultrathin system to image a micron-scale target (Fig. 4.14a). Fig. 4.14b shows the bright-field and differentiated onion cells for wavelengths of 1280 and 1120 nm. At the off-resonant wavelength ($\lambda = 1280$ nm) the images are formed without differentiation while at resonance ($\lambda = 1120$ nm) there is significant edge enhancement for each of the cell walls. In this case there is more noise in the images compared to the experiments employing the differentiator on an objective lens or camera sensor. We believe that the additional noise can be attributed to the diffractive artifacts from the metalens due to non-unity focusing efficiency, an issue that is slightly exaggerated due to the weaker signal strength after passing through the differentiator. This issue can be minimized by optimizing the lens design[68], [71] and fabrication [3], [4].

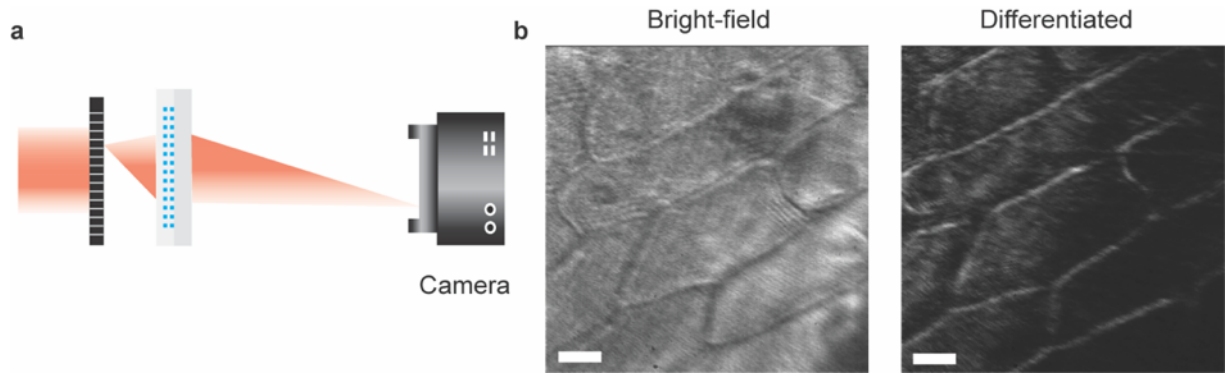

Figure 4.14. Imaging and edge detection using bilayer compound metaoptic. (a) A schematic of the imaging setup. (b) Imaging results for bright-field (left) and differentiated (right) onion cells. Scale bar: 50 μm.

4.8 Conclusion

In conclusion, we have experimentally demonstrated two-dimensional image differentiators with high resolution, thin form factor, and a simple geometry which allows rapid and cost-effective large-scale manufacturing. Furthermore, we have demonstrated how a complete image processing system can be accomplished using monolithic compound flat optics. These types of optical analog image processors could open new doors for applications in areas such as biological imaging and machine vision. Metaoptics with more complex ***k***-space response could also be realized by employing multilayer architectures[105] and inverse design mechanisms[63], [67], [71] for more complex optical analog computing and image filtering.

Chapter 5

Conclusion and Outlook

The focus of this thesis research has been to expand the engineering freedoms of metasurfaces by exploring multilayer flat optics. The multilayer platforms outperform conventional single-layer metasurface as they provide additional design freedoms, thus allowing enhanced functionalities to be integrated on a single chip while maintaining an ultrathin form factor. There were several impactful results obtained in this journey with the focus on probing their prospects of applications for metaoptics and optical analogue computing. In this chapter, I will summarize my work as well as outline several promising research directions.

5.1 Summary

In Chapter 2, I developed a unique technique to realize multilayer dielectric metasurfaces using standard nanofabrication processes along with 2D material transfer technique. The tightly spaced architecture ensures an ultrathin planar form factor but provides additional design freedoms without sacrificing sampling resolution or introducing adjacent resonator coupling, which have been commonly employed on a single layer surface. I further explored multilayer dielectric transmit-arrays for achieving highly efficient phase control at multiple wavelengths, and experimentally demonstrated multiwavelength metalenses and spectrum splitters with improved focusing efficiency and high imaging resolution.

In Chapter 3, I extended the technique as a generic platform that allows for independent control over multiple optical properties. I went beyond phase modulation by employing various combinations of metasurface layers that serves to control different degrees of freedoms of light

such as phase, polarization and amplitude. The independent design of each layer allows to realize various types of high-performance multifunctional metaoptics including multiwavelength holograms, multiwavelength waveplates and polarization-independent 3D holograms with on-axis evolvement.

In Chapter 4, I transitioned my focus to developing nonlocal flat optics and their associated compound systems for optical analog image processing. I worked out a photonic crystal slab that exhibits a quadratic dependent 2D transfer function over a large numerical aperture, which serves as a differentiator to perform optical analogue of Laplace operation. The compactness of the differentiator allows us to flexibly integrate the device into conventional imaging systems such as optical microscope and camera sensor, thus outlining the potential applications for biological imaging and computer vision with fast computing speed and low power consumption. To further shrink down the system footprint, I also demonstrated a monolithic bilayer metaoptic by integrating the differentiator with a metalens, resulting in a compound image processing system that is compatible for integration with ultracompact optoelectronic systems.

5.2 Future outlook

In the past decade, the development and study of dielectric metasurfaces have been rapidly growing, as they can mimic the functionalities of many of the conventional diffractive and refractive optics, with higher efficiency and resolution and more importantly, the capability to provide novel functionalities that are challenging to implement in convention optics. With today's growing need for compact, flexible and portable consumer devices, their ultrathin form factor and compatibility with micro- and nano-fabrication techniques are promising to make a revolution in optics design and manufacturing, and thus enable the realization of the next generation ultracompact optical systems. The multilayer dielectric metasurfaces provide an ideal platform to

resolve the long-standing issue regarding the number of degrees of freedoms that can be encoded on a single chip, which allows us to increase their functionality density with reduced performance degradation. Despite the advances presented in this thesis, there are still plenty of room for improvement from both the theoretical and application aspects, thus leading to many new research directions to explore. Here I will briefly list some of the opportunities and their potential challenges.

One of the major challenges in the multilayer systems is their design complexity, as the systems not only involve analyses of each individual layer, but also their interlayer interaction. To reduce the design complexity, the majority of the design mechanisms in this thesis are based on the assumptions that the functionality of each layer is directly passing to the next without considering their interlayer spacing effect. While such effect can be mitigated by bringing the two layers close enough, it still leads to performance degradation and efficiency reduction, which can be substantially amplified if one wants to extend to more than three layers. Ultimately, it is necessary to employ a more rigorous mechanism that can precisely design the whole system to reach an state-of-art performance. One promising route is to employ inverse design such as adjoint-based optimization, as the full wave simulation ensures that all possible physical mechanisms are simultaneously taken into account for each iteration. While such method has proved to be useful for designing periodic metasurfaces such as gratings and polarizers, for non-periodic system the full wave simulation becomes particularly demanding if one wants to design a large-scale system. To rigorously design a metasystem with a practical size, a more efficient full-wave solver needs to be developed for modelling large-scale non-periodic metasurfaces.

In addition to design complexity, there are also great challenges for extending the multilayer platform in the visible. While the use of silicon allows for broad applications in the near

infrared such as night vision and information processing, a large portion of the commercial optical devices on the market are targeted at the visible frequencies. One major unresolved issue is the absence of high-index and low-loss dielectric materials in the visible. While TiO_2 and Si_3N_4 have been investigated for realizing visible metalenses, their relatively low index (<2.5) imposes challenges to achieve a 2π phase coverage when capped in a low-index material. One possible route is to explore gallium phosphide (GaP) as an alternative material platform, which has a higher index (~3.3) essential for the transfer process that involves low-index encapsulation. However, the growth of the GaP film is generally not compatible with low-index transparent substrate, and special material transfer or wafer bonding techniques need to be developed.

Another interesting topic is to explore complex $\boldsymbol{k}$-space functions in nonlocal flat optics for a wide range of applications such as signal processing, periodic extraction, mode sorting, lasing and optical neural network. To date, the majority of the metasurface research are focused on wavefront manipulation in real space, but many of the principles and functionalities are a direct replicate of classical optics which can generally be achieved in conventional optics. The nonlocal dispersion, also referred to as dispersion in momentum space, is fundamentally challenging to realize in convention refractive and diffractive optics. Based on nonlocal flat optics such as photonic crystal slabs, the guided mode resonances supported within the slab can provide an alternative route to achieve nonlocality due to their angularly dependent mode matching conditions. In chapter 4, we have realized a quadratic-dependent transfer function for image differentiation but the design is not generalizable to other $\boldsymbol{k}$-space functions. To realize an arbitrary nonlocality, it is highly desirable to develop a generic design methods that can deterministically search for a particular set of guided mode resonances.

Finally, I believe another impactful and exciting area is tunable metasurface. While extensive efforts have been devoted to exploring various tuning mechanisms, the ability to precisely address each individual meta-atom remains a major challenge and none of the work has proved to be able to compete with the commercially available spatial light modulators. There is still plenty of room for improvement in terms of speed, resolution and efficiency. Future efforts may be devoted to developing new active materials or fundamentally novel tuning mechanisms.

Appendix A

Multilayer Dielectric Metasurfaces for Multiwavelength Metaoptics

A.1: Design and simulation

The transmission coefficient of the nanoposts was retrieved using a rigorous coupled wave analysis (RCWA) solver[144]. A 750 nm tall Si nanopost was arranged in a square lattice with a period of 600 nm, embedded in PDMS. The refractive index of the Si was acquired using ellipsometry (3.547, 3.5 and 3.47 at 1180 nm, 1400 nm and 1680 nm, respectively) and the index of PDMS was set to be 1.4. The complex transmission coefficients as a function of nanopost radii were calculated under normal incidence. The diameters of the nanoposts that sit in the transmission dips were neglected by evaluating deviation from an ideal phase mask. Note that the use of a SiO_2 substrate has a negligible effect on the optical properties of nanoposts due to its small index contrast (<0.05) with the PDMS cladding layer. The transmission coefficients were assumed to be the same for both layers.

To design the multiwavelength metalens, the radii at each layer (r_1, r_2) are designed using a brute force search algorithm. The desired phase of the lens, $\varphi_{lens}(x, y, \lambda)$, at each lattice site was first calculated based on the equation

$$\varphi_{lens}(x, y, \lambda) = -\frac{2\pi}{\lambda}\left(\sqrt{x^2 + y^2 + f^2} - f\right)$$

An error function was defined to quantify the deviation between the ideal phase of the lens and the added phase from each pair of radii

$$\Delta(x,y,r_1,r_2,n,m)=$$
$$|\varphi(r_1,\lambda_1)+\varphi(r_2,\lambda_1)+2\pi n-\varphi_{lens}(x,y,\lambda_1)|+|\varphi(r_1,\lambda_2)+\varphi(r_2,\lambda_2)+2\pi m-\varphi_{lens}(x,y,\lambda_2)|$$

where n and m are integers to unwrap the phase. At each lattice site (x,y), all possible pairs of (r_1,r_2) are used as input in the algorithm to find the designs that give rise to the function minima. The comparisons between the designed phase and the target phase are provided in Fig. A1 below.

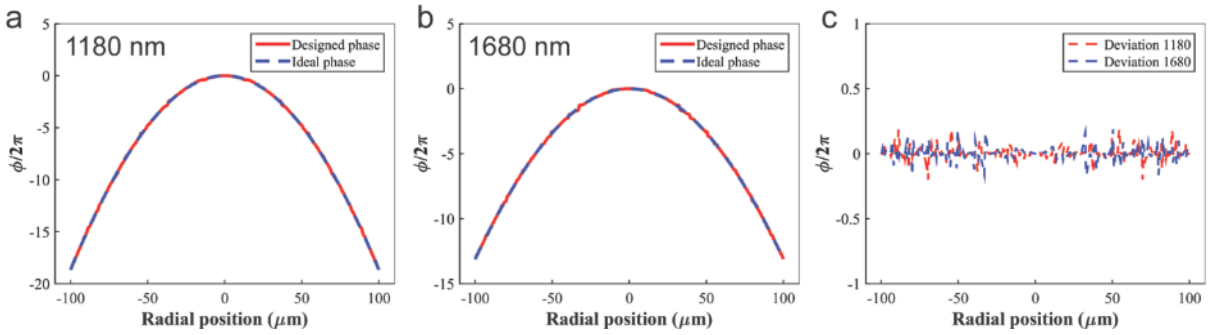

Figure A1. Designed phases VS target phases. (a, b) Retrieved spatial phase distributions from the designed nanoposts (solid red) and an ideal phase of lens (dashed blue) at 1180 nm (a) and 1680 nm(b). The lens has a diameter of 200 μm and a focal length of 216 μm (NA=0.42). (c) Deviation of the designed phases from the ideal phase of lens as a function of radial positions. The average deviations are 0.057π and 0.059π at 1180 nm and 1680 nm, respectively.

By the same principle, the function for designing a three-wavelength metalens using three layers of metasurfaces has the following form

$$\Delta(x,y,r_1,r_2,r_3,n,m,l)=$$
$$|\varphi(r_1,\lambda_1)+\varphi(r_2,\lambda_1)+\varphi(r_3,\lambda_1)+2\pi n-\varphi_{lens}(x,y,\lambda_1)|$$
$$+|\varphi(r_1,\lambda_2)+\varphi(r_2,\lambda_2)+\varphi(r_3,\lambda_2)+2\pi m-\varphi_{lens}(x,y,\lambda_2)|$$
$$+|\varphi(r_1,\lambda_3)+\varphi(r_2,\lambda_3)+\varphi(r_3,\lambda_3)+2\pi l-\varphi_{lens}(x,y,\lambda_3)|$$

The designed nanopost parameters were then loaded into an open source finite difference time domain (FDTD) solver, MEEP[101], which was run on the Advanced Computing Center for

Research and Education (ACCRE). To avoid the Fabry-Perot resonance between the top and bottom PDMS surface while keeping the computation space small in z direction, the PDMS is extended to the top perfectly matched boundary layer. A continuous source is normally incident from the air to the bottom PDMS surface, passing through the multilayer metasurfaces. The complex electric field was then taken at a distance 3 μm above the nanoposts, and intensity distributions in the farfield were calculated based on a transfer function of free space.

A.2: Misalignment simulation for large-scale Lenses

The misalignment effect for large-scale lenses show in Fig. A2 below was simulated by retrieving transmission coefficients for each wavelength based on the designed nanopost parameters at each layer. The phase mask at one layer was then shifted and added to the phase from the second layer to form a misaligned transmission mask. The transmission mask was then used to propagate a beam into the farfield based on a transfer function in free space.

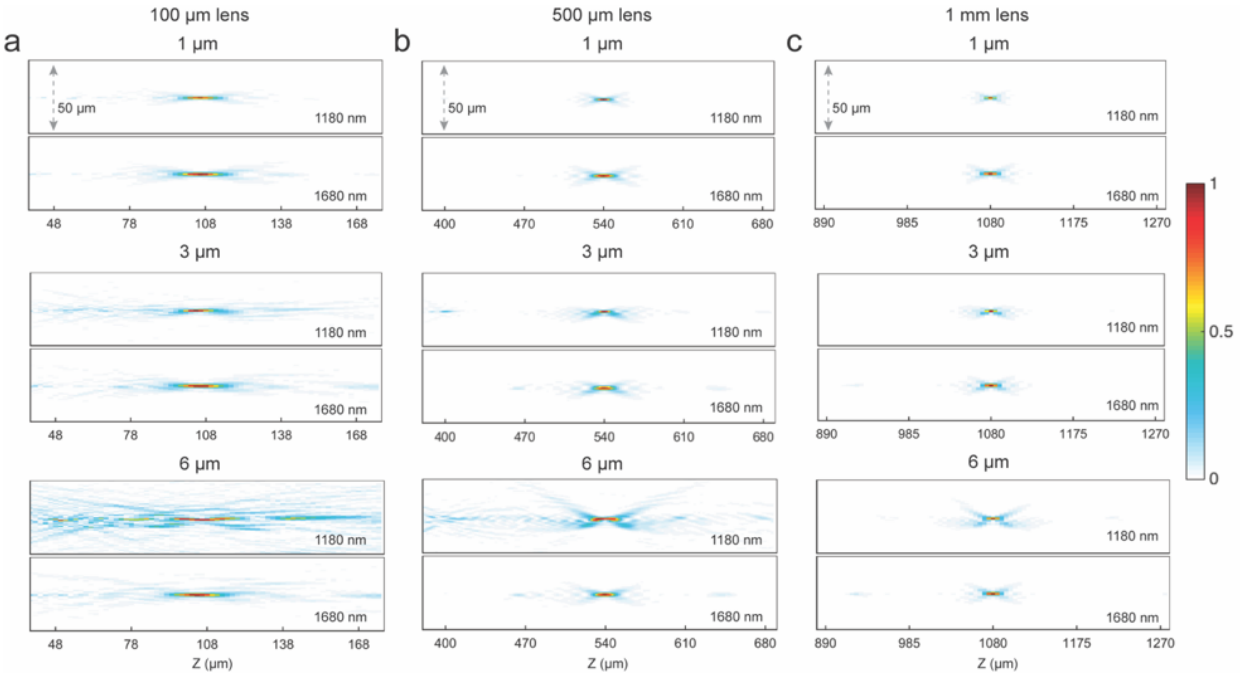

Figure A2. Misalignment effect for different lens diameters with the same numerical aperture. (a, b, c) Simulated axial intensity distributions under different misalignments for lens diameters of 100 μm (a), 500 μm (b) and 1 mm (c) with the same numerical aperture (0.42).

A.3: Non-interacting bilayer metasurfaces

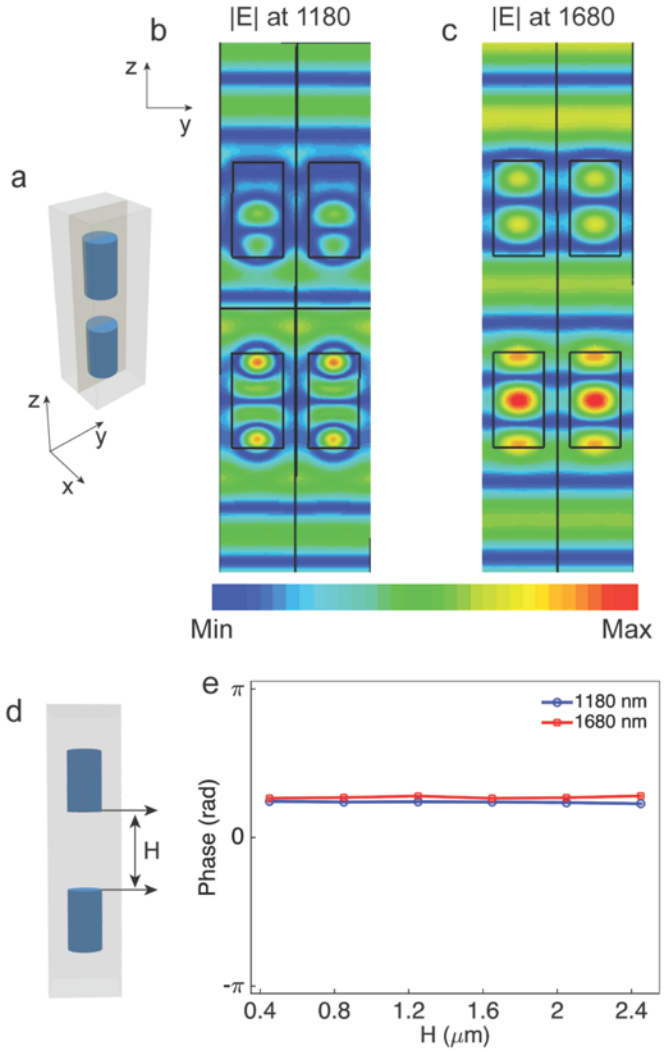

Figure A3. Field profiles of the metasurface doublet. (a) Schematic of a unit cell with a radius of 100 nm at both layers. (b, c) Simulated electric field amplitude at 1180 nm (a) and 1680 (b) with a 1.5 μm layer separation in the YZ cross section plane, showing no field coupling in the Z direction. (d, e) Simulated phase of the bi-layer unit cell as a function of layer distance H. The constant phase profiles indicate the response of each layer is independent of the other.

A.4: Measurement

A customized imaging system was built up by a 50X objective (Mitutoyo Plan Apo, NA=0.42) paired with a tube lens. To ensure achromaticity of the characterization system, a 5X objective (Mitutoyo Plan Apo, NA=0.14) was used as a tube lens. The focal spot profiles were characterized by illuminating the sample with a collimated supercontinuum laser (Fianium WhiteLase) that passed through a monochromator (Cornerstone^{TM} 130 1/8m), and the image intensity was recorded by a NIR camera (Xeva-1.7-640). The metalens was driven continuously on a motorized stage (Throlabs PT1-Z8) along the propagation direction for 0.3 mm while 267 slices of images around the focal plane were subsequently captured by the camera corresponding to 1.13 um between each slice. The images were then stacked together to form the axial intensity distributions shown in Fig. 2.5d. A schematic of the characterization system is shown in Fig. A4. The focusing efficiency was calculated by the ratio between the focusing power and the total incident power on the lens. To ensure that most of the power was incident on the device, a lens (AC254-200-C-ML, f=200 mm) was placed in the front to form a ~200 μm diameter beam illumination. The focusing power was measured by passing the beam through an iris placed at the conjugate plane opened at a diameter corresponding to eight times the FWHM of the focal spot on the image plane. The total incident power was measured by removing the sample and opening the iris completely.

To perform the imaging, the test chart was illuminated using a 20X objective (Mitutoyo Plan Apo, NA=0.40) as a condenser. The metalens was placed at a fixed position (~one focal length) away from the chart for imaging at both wavelengths. A tube lens (Mitutoyo Plan Apo, NA=0.14) was used to form an image on the camera. Meanwhile, the condenser was slightly

adjusted to reduce the noise and ghost images. A schematic of the imaging system is shown in Fig. A4b.

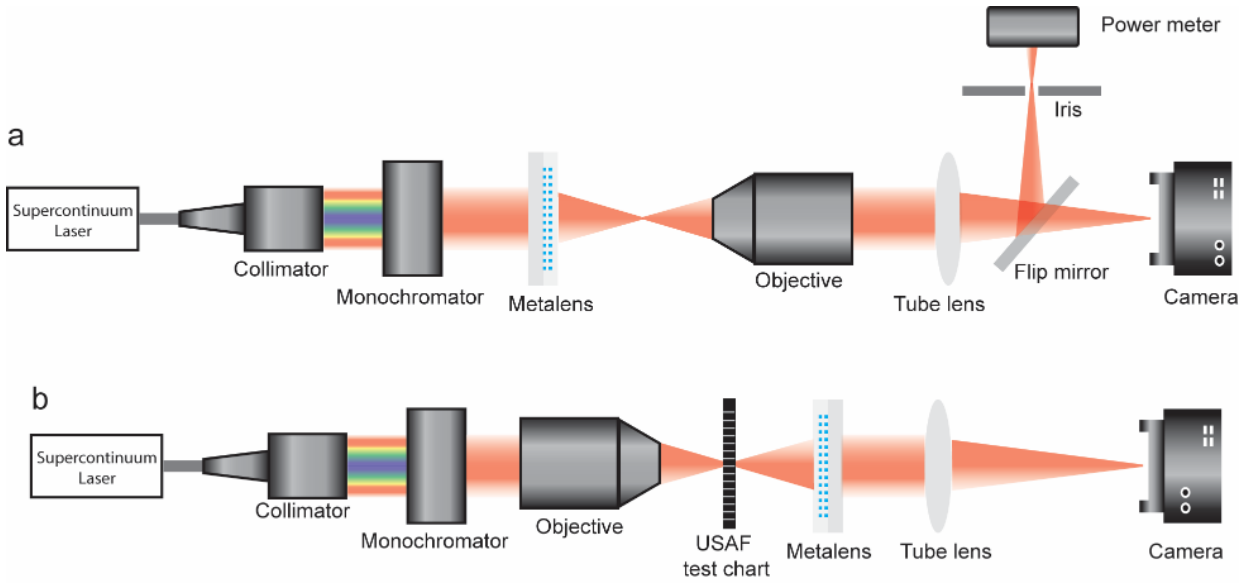

Figure A4. A schematic of the measurement setup for the focal spot characterization, focusing efficiency measurement and imaging. (a) A collimated laser beam was passed through a monochromator and the focal spot profile was imaged through an objective, paired with a tube lens, on a camera. The focusing efficiency was measured by a flip mirror directing the beam through an iris placed at the conjugate plane, and the intensity was measured by a power meter (Newport meter 1918-c). The iris was opened at a diameter of eight times the FWHMs on the imaging plane. b, The optical system for imaging an 1951 USAF test chart.

A.4: Fabrication of multilayer metasurfaces

The first layer was prepared using a 750 nm thick a-Si wafer grown on a fused silica by plasma-enhanced chemical vapor deposition (PECVD). A 200 nm PMMA A4 was spin coated at 4500 rpm, followed by a 10 nm chromium conduction layer deposition using resistive evaporation. The patterns were then defined in the PMMA by electron beam lithography followed by developing in MIBK: IPA 1:3 (MicroChem). A 35 nm thick aluminum oxide was then deposited by e-beam evaporation to form a dry etch hard mask, followed by removing the remaining PMMA using PG remover. The Si nanoposts were subsequently formed by reactive ion etching using C_4F_8

and SF_6. To fully encapsulate the high-filling-fraction nanoposts, the PDMS (10:1 mixing ratio of Sylgard 184 base and curing agent) was diluted with toluene in a 2:3 weight ratio. After degassing for 5 minutes, the diluted PDMS was spin coated at 2000 rpm to encapsulate the Si nanoposts and cured at 80 C° for more than one hour.

The second substrate was prepared by firstly depositing a 300 nm thick germanium (Ge) by Ar sputtering from a 3" Ge target. The same thickness a-Si was grown using PECVD and the second-layer metasurface structures were defined using the same fabrication procedure as the first. The nanoposts were embedded by first spin coating a thin layer of diluted PDMS (2:3 PDMS Toluene weight ratio, 2000 rpm spin coating) to penetrate through the nanoposts, followed by curing at 80 C° for more than one hour. The second layer of thicker PDMS without dilution (10:1 mixing ratio of Sylgard 184 base and curing agent) was spin coated at 1000 rpm and cured at 80 C° for more than three hours to form a ~50 μm thick mechanical support for transferring the film. The sample was then immersed in a mixture of hydrogen peroxide, ammonium hydroxide and DI water to dissolve the germanium sacrificial layer (>30 h) to release the second layer of metalens.

A.5: Alignment

A schematic of the alignment setup[145] is shown in Fig. A5. To perform the alignment, the first layer of metalens was attached on a glass slide by Kapton tape, and loaded in an XYZ translation stage with the lens side facing down. A second sample stage was placed underneath with a copper hotplate and a rotation stage. The second metalens layer was flipped over with the rod side facing up, mounted on a ~250 nm thick PMMA A5 spin coated on a Si substrate, and held on the copper hot plate by a vacuum pump. Due to optical transparency of both SiO_2 and PDMS, one can see through the first layer using a digital camera (Nikon D3200) paired with a zoom lens

(MVL12X3Z) and an extension tube (MVL20FA). The first metalens was then brought close enough to the second until both alignment marks were clearly visible. The alignment marks were then aligned by tuning the XYZ translation and rotation stage. After spatial alignment was achieved, the top metalens was lifted up, and a drop of uncured PDMS was applied on the bottom metasurface. The top metalens was then brought close enough to engage with the bottom, followed by pressing to form a thin PDMS bonding layer until both alignment marks were clearly visible. The hotplate was then turned on at 80 C° for more than one hour to bond the two layers together by means of PDMS curing. Meanwhile, the XYZ translation stage was slightly adjusted to compensate for the PDMS thermal drift.

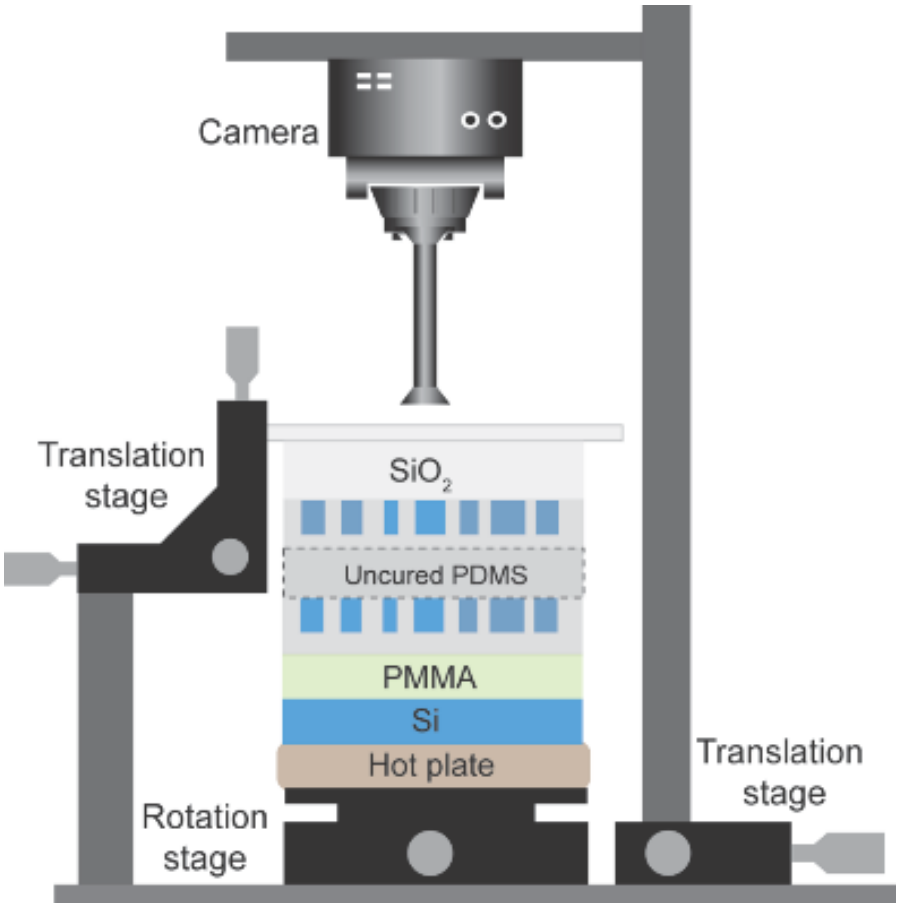

Figure A5. A schematic of the alignment and bonding processes. A camera paired with a zoom lens and an extension tube was positioned to image through the metalens doublet. The imaging system was mounted on an XY translation stage to switch the field of view between two alignment marks. The top metalens was attached to a glass slide and placed on an XYZ translation stage. The bottom metalens was mounted on a layer of PMMA spin coated on a Si substrate. Uncured PDMS was applied in between as a thin bounding and index-matched layer.

A.6 Misalignment approximation

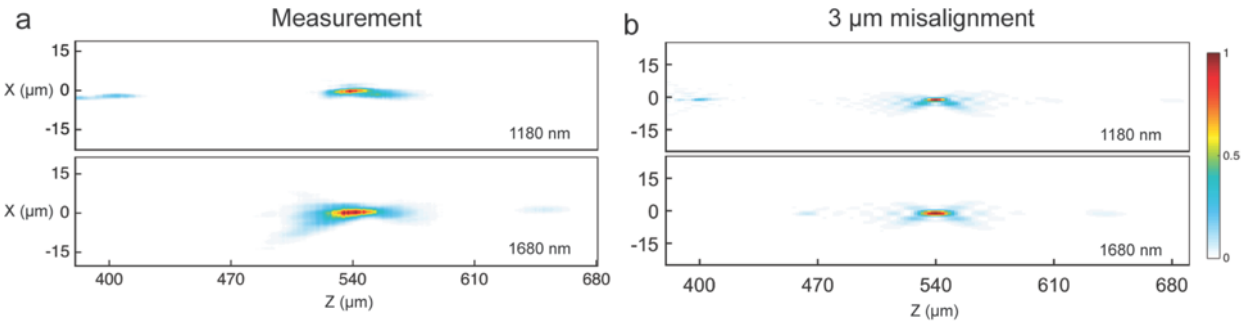

Figure A6. Measurement compared to a 3 μm lens misalignment. (a) Measured axial intensity distributions. (b) Simulated axial intensity distributions under 3 μm misalignment. Note that the weak secondary focuses are shown at ~400 μm at 1180 nm and ~650 μm at 1680nm, agreeing well with the measurement.

A.7: Continuous band metalens triplet

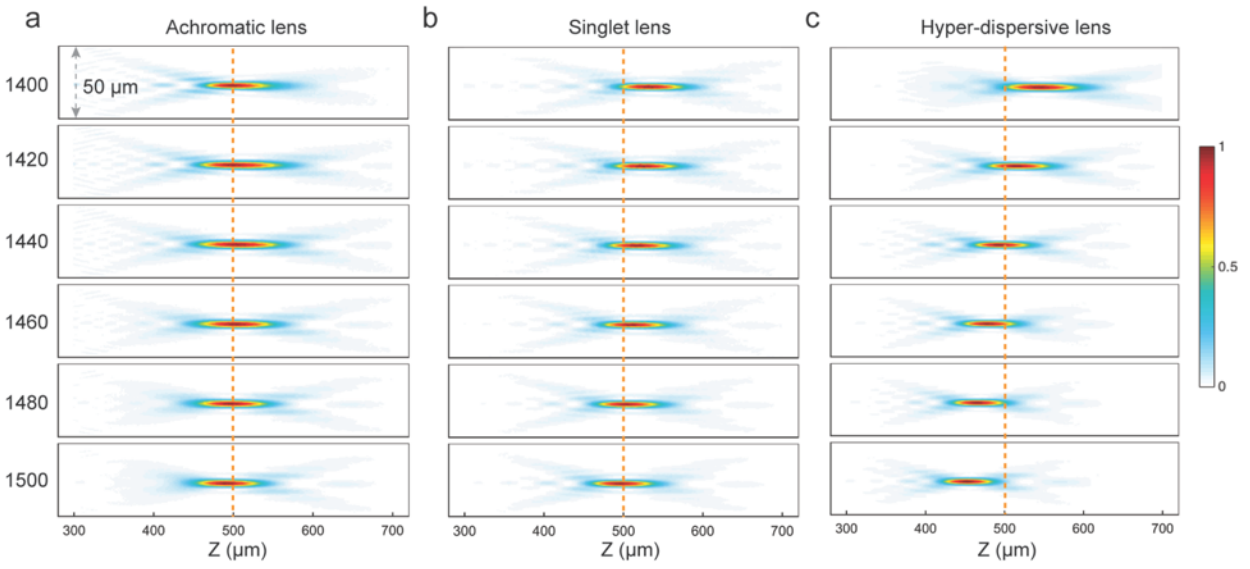

Figure A7. Demonstration of dispersion engineering by a 200 μm metasurface triplet with NA=0.196 and 100 nm bandwidth. (a, b, c) Simulated axial intensity distributions of an achromatic metalens triplet (a), a singlet metalens (b), and a hyper-dispersive metalens triplet (c).

Appendix B

Multifunctional Metaoptics Based on Bilayer Metasurfaces

B.1: Ellipticity calculation

The polarization state of the quarter-wave plate was numerically determined by using the Stokes parameters:

$$S_0 = |t_{xx}|^2 + \left|t_{xy}\right|^2$$

$$S_1 = |t_{xx}|^2 - \left|t_{xy}\right|^2$$

$$S_2 = 2|t_{xx}|\left|t_{xy}\right| cos\Delta\varphi$$

$$S_3 = 2|t_{xx}|\left|t_{xy}\right| sin\Delta\varphi$$

where t_{xx} and t_{xy} are the transmission coefficients for co-polarization and cross-polarization, respectively, and $\Delta\varphi$ is their phase difference, $\angle t_{xy} - \angle t_{xx}$. The ellipticity χ can be expressed in terms of the Stokes parameters as follows: $\sin(2\chi) = \frac{S_3}{S_0}$. The details of transmission and ellipticity for all the designed multiwavelength waveplates are provided in Fig. B1. Below.

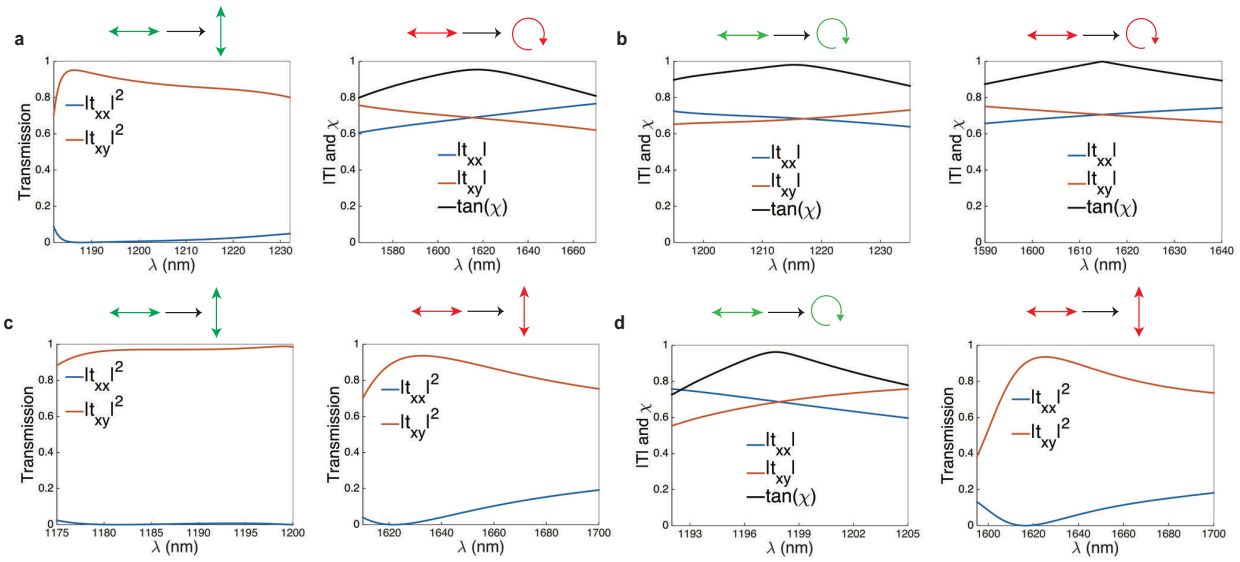

Figure B1. All combinations of multiwavelength metaoptic waveplate based on polarization sensitive nanopillars. (a-d) Simulated transmission for a HWP at 1200 nm, QWP at 1600 nm (a), QWP at 1600 nm, QWP at 1200 nm (b), HWP at 1200 nm, HWP at 1600 nm (c), and QWP at 1200 nm, HWP at 1600 nm (d), where HWP denotes a half-wave plate and QWP denotes a quarter-wave plate.

B.2: Multiwavelength hologram design

The multiwavelength hologram was designed using a brute search algorithm. The transmission properties of the bilayer metasurface were calculated using the product of the transmission coefficients from each layer,

$$t(\lambda, r_1, r_2) = t_1(\lambda, r_1, r_2) \cdot t_2(\lambda, r_1, r_2)$$

where r_1 and r_2 are the radii of the nanoposts at each layer. The phase patterns for producing different hologram images were calculated using the Gerchberg-Saxton algorithm[109], resulting in two independent target phase masks (t_{λ_1} and t_{λ_2}) for each wavelength. At each lattice size, the radii at each layer (r_1, r_2) were designed by calculating the total error from the desired transmission masks at the two wavelengths

$$\Delta(x,y) = \left|t_{\lambda_1}(x,y) - t(\lambda_1, r_1, r_2)\right| + \left|t_{\lambda_2}(x,y) - t(\lambda_2, r_1, r_2)\right|$$

The Color-coded deviation plot between the designed and ideal transmission phase is provided below in Fig. B2. The transmission coefficients of the metasurface for each wavelength were selected based on the designed nanoposts at each layer, and the far-field images were calculated by taking a Fourier transform of the transmission masks.

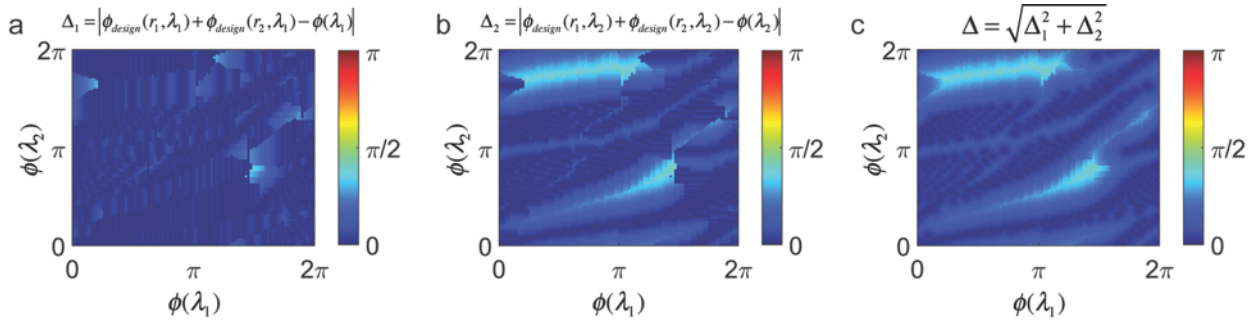

Figure B2. Color-coded deviation plot between the designed and ideal transmission phase. (a-b) The deviation plot for λ_1(a) and λ_2 (b). The deviation is defined as $\Delta = \left|\phi_{design}(r_1, \lambda_{1,2}) + \phi_{design}(r_2, \lambda_{1,2}) - \phi(\lambda_{1,2})\right|$ for each wavelength where $\phi(\lambda_{1,2})$ is the designed phase for $\lambda_{1,2}$, respectively. (c) The total deviation plot for both wavelengths.

The full wave simulation of the grating was carried out using an open source FDTD solver (Meep[101]). A multiwavelength blazed grating was designed to diffract the incident light at 15° and -15° at the wavelengths of 1180 and 1680 nm, respectively. The bilayer metasurface was embedded in a layer of PDMS and simulated with a 3 μm vertical layer spacing. The transmitted and total incident power were acquired by using a Gaussian pulse source and measuring the power flux with and without the device. The relative diffraction efficiency was calculated using a plane wave source to acquire the complex electric field after the metasurface and the diffracted power was obtained by taking its Fourier transform. The absolute diffraction efficiency was calculated using the product of the transmission and relative diffraction efficiency.

B.3: Misalignment approximation

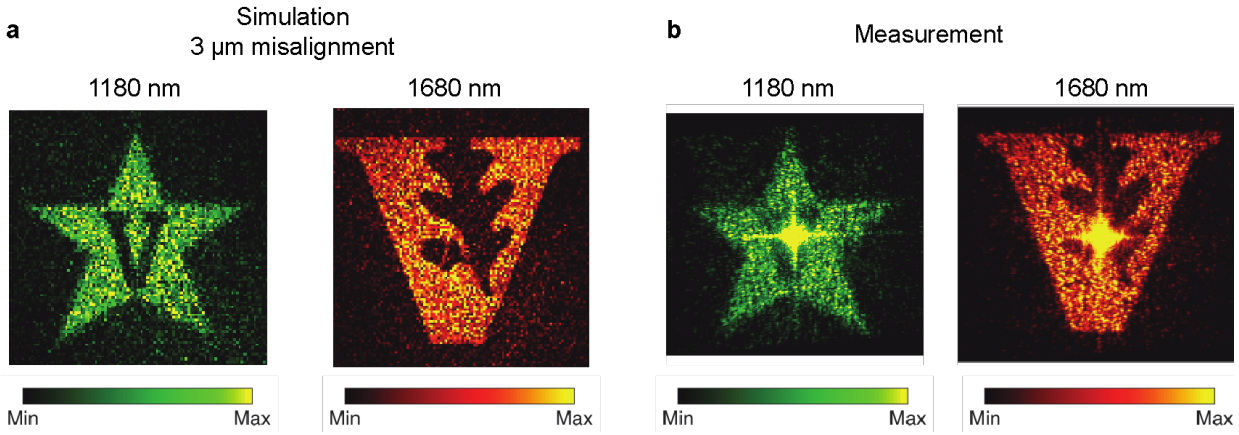

Figure B3. Measurement compared to a 3 μm metasurface misalignment. Simulated hologram images (a) under a 3 μm misalignment and measurement (b).

B.4: 3D hologram design

To design a 3D clock hologram with on-axis evolvement, three types of 3D holograms were created that comprise the frame and two hands of the clock. The frame is composed of a 3D hollow cylinder with an extended depth of focus from z=0.9 mm to 2.7 mm. To reduce on-axis image distortion, the ring image was sampled into multiple slices along z axis and a constant phase distribution $k \times z$ was added to each xy-plane, where k is the wave vector in free space. The transmission masks were then used to propagate a beam backwards at the wavelength of 1400 nm by the distance away from the metasurface, and the complex field profiles (E_{frame}) were calculated by the sum of contributions from all slices. The central areas with amplitude smaller than 0.2 were set to zero for incorporating additional hologram design.

To design the two hands of the clock, two rectangular amplitude masks with different length (L_1=35 μm, L_2=73 μm) were created to appear at the distance of 1.8 mm away from the metasurface. A phase pattern was added to each rectangle for generating an angular velocity, which is given by $\varphi = \omega r^2 \theta$. Here, r and θ are the radius and angle in polar coordinates. Thus, in

Cartesian coordinates the complex electric field profile for creating the hands of clock is

$$E_{hand}(x,y) = E^1_{rect}(x,y) \cdot \exp\left[i\omega_1(x^2+y^2)\, arctan\frac{y}{x}\right] + E^2_{rect}(x,y) \cdot \exp\left[i\omega_2(x^2+y^2)\, arctan\frac{y}{x}\right]$$

where E^1_{rect} and E^2_{rect} are the amplitude profiles of the two rectangles. Independent angular velocities of $\omega_1 = 5.2 \times 10^{-3}$ μm^{-2} and $\omega_2 = -3.6 \times 10^{-3}$ μm^{-2} were added to each amplitude mask. The field was then used to back propagate a beam for a distance of 1.8 mm to generate the phase and amplitude of the metasurface. To increase the misalignment tolerance, every pixel on the metasurface is expanded to a 4 × 4 supercell. Combined with the field distribution for the clock frame, the total electric field profile is,

$$E(x,y) = E_{frame}(x,y) + E_{hand}(x,y)$$

B.5: Measurement

The multiwavelength hologram was characterized using the setup shown in Fig. B4a. The samples were illuminated using a collimated supercontinuum laser (Fianium WhiteLase) whose beam was passed through a monochromator (Cornerstone™ 130 1/8 m). To reduce the beam size, a lens (AC254-200-C-ML, *f* = 200 mm) was placed in front of the device to partially focus the light. The far-field hologram images were recorded using an InGaAs NIR camera (Xeva-1.7-640).

The 3D clock hologram was characterized using a custom imaging system with a 20× objective (Mitutoyo Plan Apo, NA = 0.4) paired with a tube lens (*f* = 200 mm). The device was mounted on a translation stage and moved along the axial direction to measure the on-axis evolution of the hologram. A schematic of the characterization system is shown in Fig. B4b.

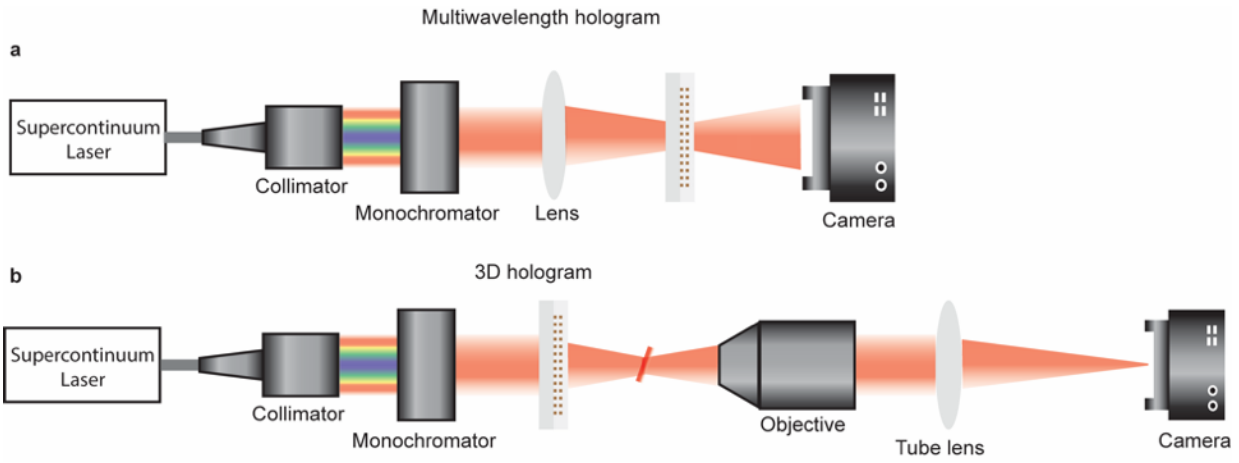

Figure B4. Schematic of the measurement setup for multiwavelength and 3D hologram characterization. (a) A collimated laser beam was passed through a monochromator and a lens was used to partially focus the beam on the metasurface. The hologram image was directly recorded by a NIR camera. (b) The metasurface was illuminated by a collimated laser beam and the on-axis image slices were captured through an objective, paired with a tube lens, on a camera.

B.6: Multilayer metasurfaces consisting of polarization sensitive nanopillars

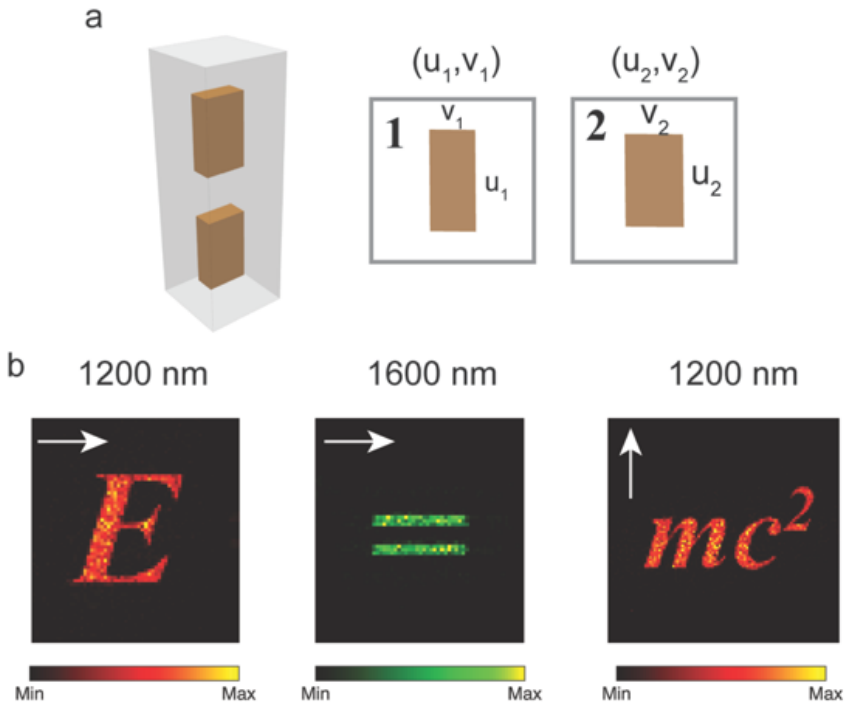

Figure B6. Multiwavelength metaoptic holograms based on polarization sensitive nanopillars. (a) Schematic of the unit cell which is composed of bilayer rectangular pillars with a height of 750 nm and a period of 600 nm. The unit cell width and length on each layer was adjusted independently for encoding addition information at the two wavelengths. (b) Simulated hologram images. The metasurface is designed to encode two hologram images at two wavelengths under *x* polarization, and a third image for *y* polarization illumination.

B.7: Transmission of the amplitude layer

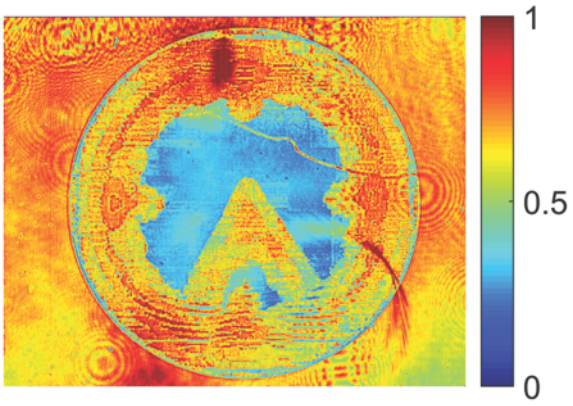

Figure B7. Transmission map of the amplitude mask.

Appendix C

Flat Optics for Image Differentiation

C.1: Simulations

The transmission spectra were calculated using the Frequency Domain (FD) solver of CST Microwave Studio. The refractive index of SiO_2 and PMMA were set to be 1.45 and 1.48, respectively, and the index of Si (3.67 at 1120 nm) was obtained using ellipsometry. The Si nanorods were modeled as a periodic unit cell on a SiO_2 substrate embedded in a PMMA cladding layer. Transmittance at other in-plane azimuthal angles is provided in Fig. C1 below.

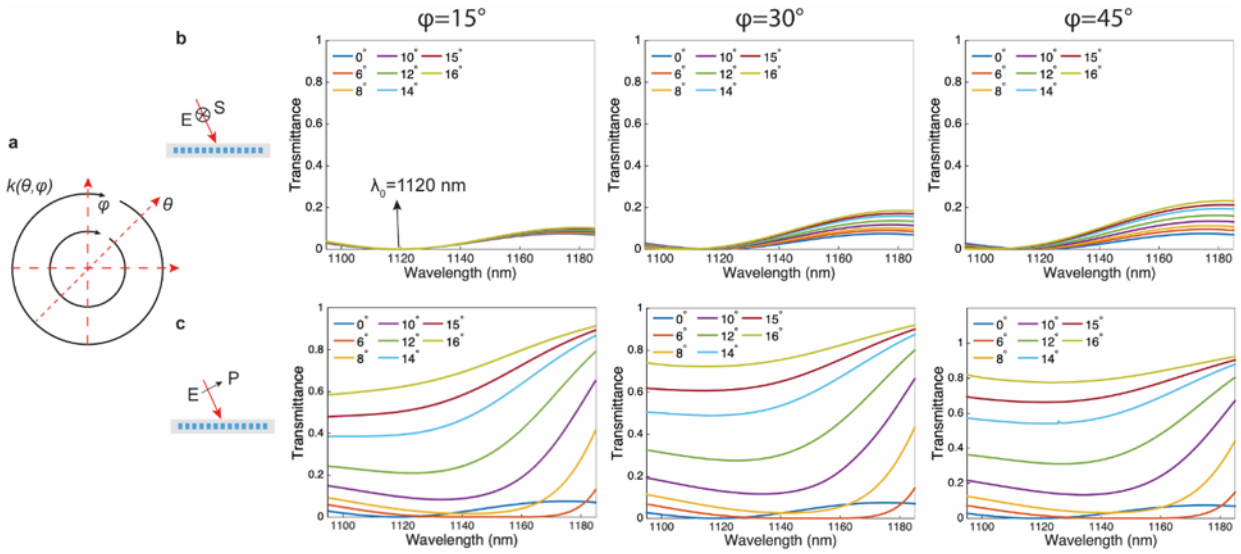

Figure C1. Transmission spectra at various azimuthal angles. (a) Angular coordinate system. φ and θ correspond to in-plane and out-of-plane azimuthal angles, respectively. (b-c) Transmission spectra for the in-plane azimuthal angle φ ranging from 15° to 45° for *s*- (b) and *p*-polarization (c) input. The near-zero transmission at $\lambda_0 = 1120$ nm for *s*-polarization indicate that no polarization conversion occurs for the transmitted light.

C.2: Large-scale fabrication using nanosphere lithography

A polystyrene nanosphere solution (D=740 nm, 10 wt %), obtained from Thermo Fisher

Scientific, was first diluted in an equal volume of ethanol by sonication. A Teflon bath was half-filled with deionized water and a tygon tube was connected to a syringe and held upright with its bevel tip just touching the water surface which allows the formation of a meniscus that helps keep the spheres from falling into the liquid. The sphere solution was then slowly injected onto the water surface at a rate of 5 μL/min by a syringe pump to form a monolayer of densely packed nanospheres. To facilitate a densely packed film, a perturbation was added during assembly through a controlled flow (5 L/min) of compressed nitrogen gas using a flat nozzle. Inside the water bath, the Si substrate was tilted at 10° to help release the stress and accommodate defects. The densely packed nanosphere film was then transferred to the Si wafer by slowly draining the bath. The entire process took less than 30 minutes to pattern a ~1 cm x 1 cm area. The illustration of defects is shown in Fig. C2 below.

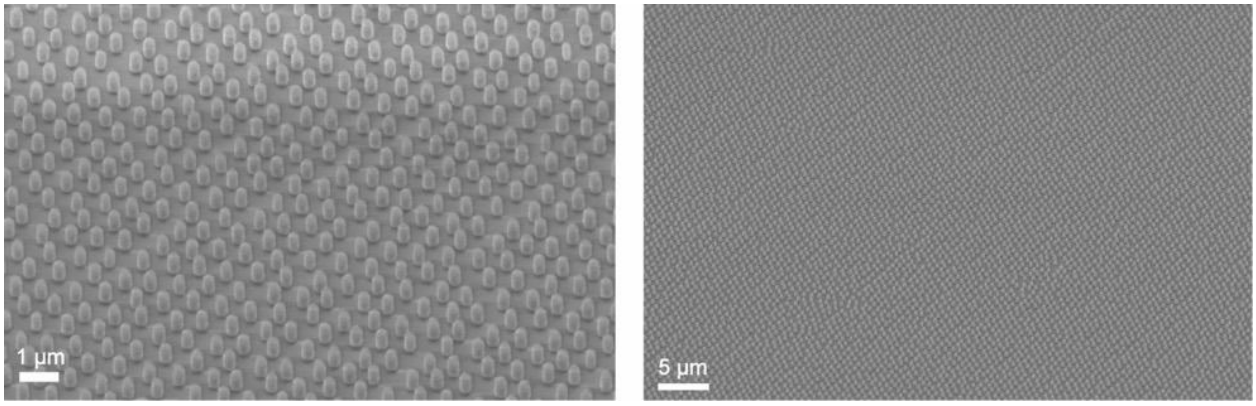

Figure C2. Illustration of defects in the large-scale image differentiator. SEM images of the large-scale differentiator fabricated using nanosphere lithography. The defects are primarily due to nanosphere size variation, resulting in different grain orientations as shown in Fig. 4.11b.

C.3: Fabrication of monolithic bilayer metaoptic

A schematic of the fabrication steps is presented in Fig. C3 below. The metalens was defined on a SiO_2 wafer with a Si device layer using electron beam lithography and reactive ion etching. The pattern was then embedded in an ultrathin polydimethylsiloxane (PDMS) layer by

spin coating. The differentiator was defined using the same procedure but before embedding in PDMS the silicon cylinders were undercut using buffered hydrogen fluoride acid by immersion of the sample for 30 s. The undercut nanorods were then encapsulated in a thicker (~50 µm) layer of PDMS, and released by mechanically peeling of the PDMS. It is worth noting that our previously demonstrated sacrificial layer based transfer techniques[105], [143] require longer solvent immersion. The transfer process used here generally only applies for uniform arrays. The two layers were then aligned and bonded together using a custom transfer and bonding system.

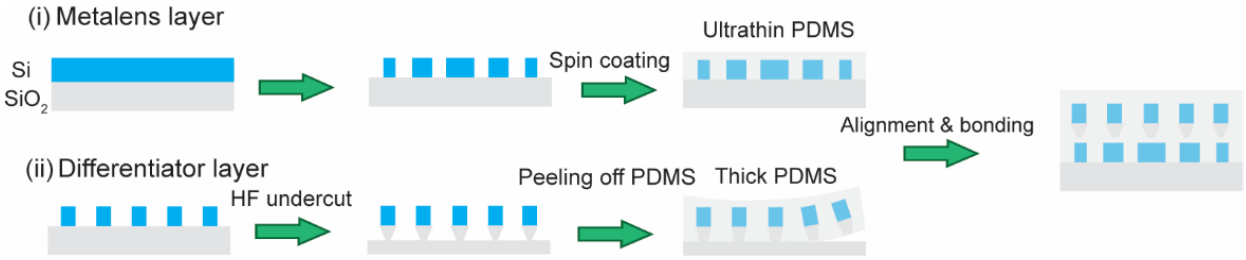

Figure C3. Bilayer fabrication technique. (i) The metalens layer was defined on a SiO_2 substrate with a Si device layer and encapsulated in a thin layer of PDMS. (ii) The differentiator layer was defined using the same procedures followed by undercutting through immersion in buffered hydrofluoric acid for 30 s. The structures were then embedded in a 50 µm thick PDMS film and transferred by mechanically peeling the PDMS from the substrate.

C.4: Differentiator efficiency

To balance the roles of NA, accuracy of the transfer function, and transmittance for image differentiation, we define the differentiation efficiency (η) as the square of transfer function ($|H(k)|^2$) at the maximum spatial frequencies that can be fitted to the desirable mathematical function (e.g. Laplacian for this work). In this regard, the efficiency can be as high as 81% at an NA of 0.315. Since the maximum NA also depends on the fitting accuracy, we can also expand the maximum fitted NA to 0.326 to achieve an efficiency of 90%, at a slight expense to the accuracy (Fig. C4 below).

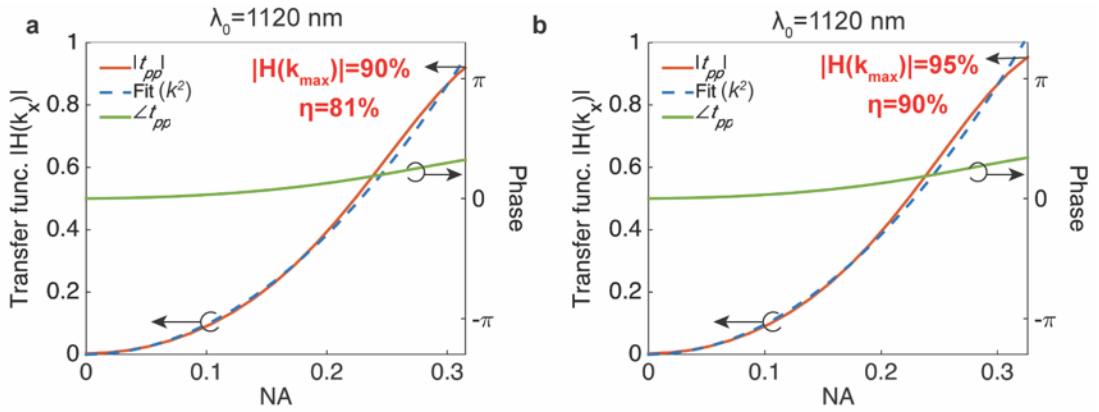

Figure C4. Differentiator efficiency. (a-b) Optical transfer function $|H(k)|$ along the Γ-X direction, and the quadratic fitting in the form of $c_{pp}k^2$. The efficiency $|H(k)|^2$ is ~81% at an NA of ~0.315 (a), and ~90% at an NA of 0.326 (b).

C.5: Differentiator bandwidth

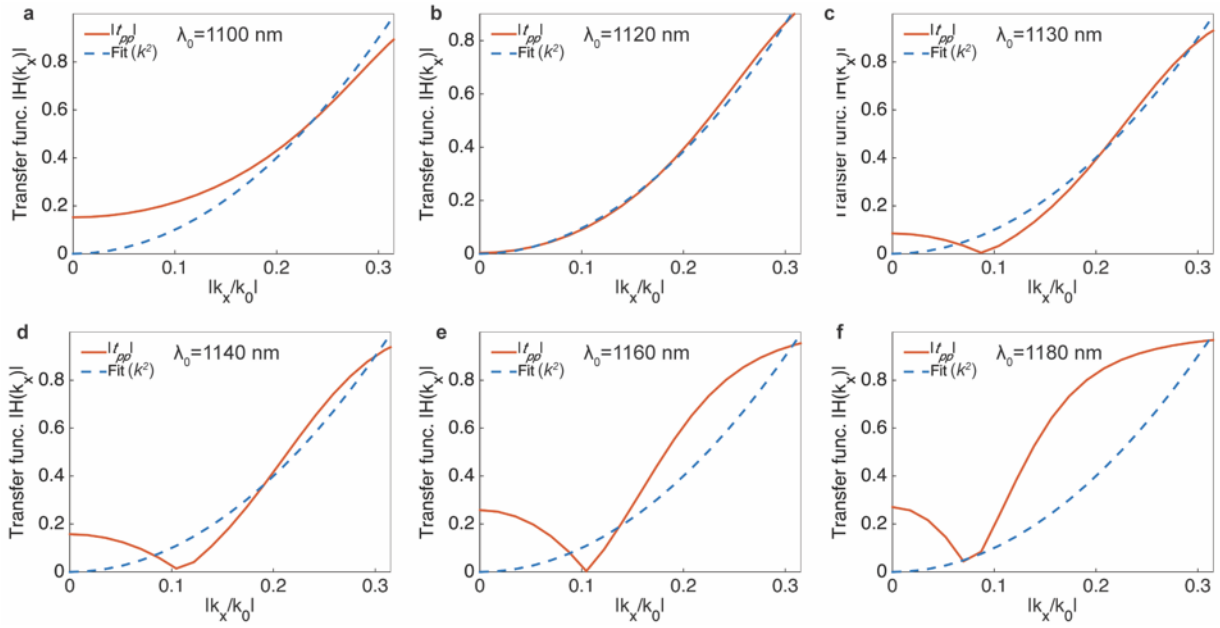

Figure C5. Differentiator bandwidth. (a-f) Modulated transfer function $|H(k)|$ and the quadratic fitting between 1100 and 1180 nm.

C.6: Differentiator with a field stop

In Fig. 4.9, the size of the differentiator is on the same order, but slightly smaller, than the objective's aperture. This could result in the differentiator acting as a beam block, allowing light at large wavevectors to pass around the edges. To exclude such an effect, a control device was made by placing a field stop around the differentiator while also placing the differentiator close to the cell sample. The results, shown in Figure C6, show that high-contrast cell boundaries are preserved, verifying that the edge enhancement is due to the transfer function of the differentiator.

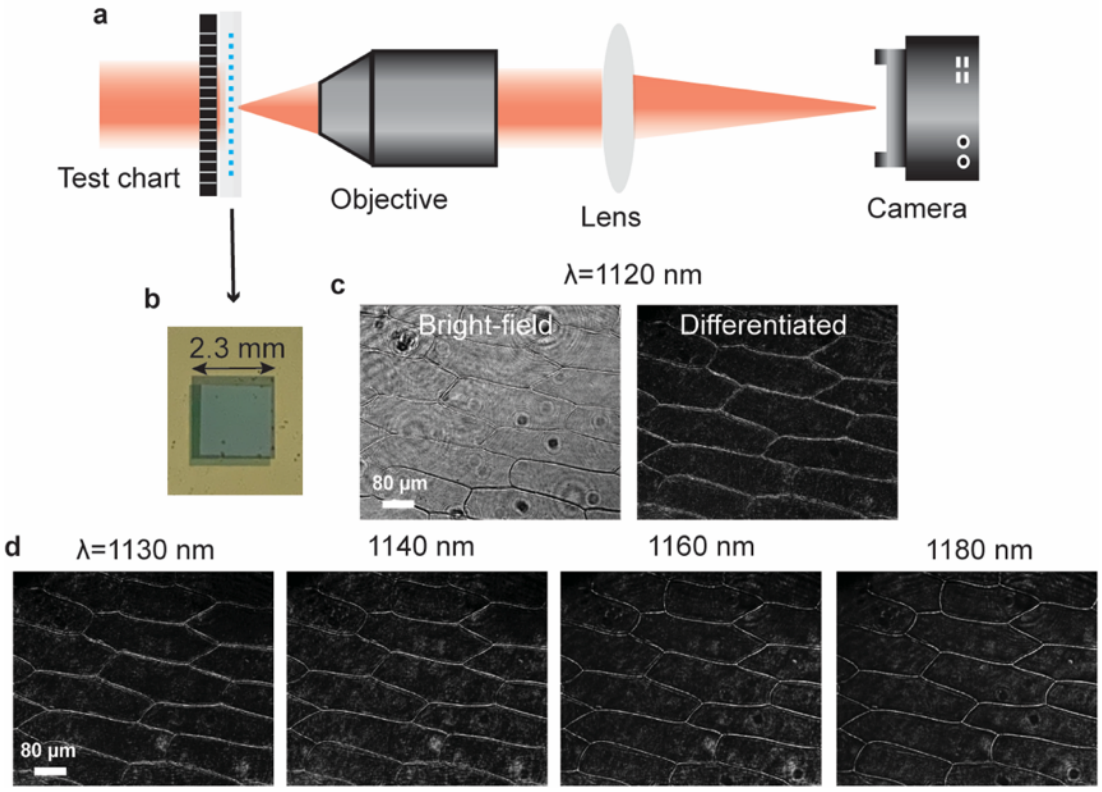

Figure C6. Control experiment using the differentiator with a field stop. (a-b) A schematic of the imaging setup. To exclude the possibility that the differentiator may serve as a beam block, the differentiator (2.3×2.3 mm^2) is covered with an aperture stop (b) and placed close to the cell sample (a). (c) Bright-field and differentiated images of the onion cells at the wavelength of 1120 nm. (d) Differentiated images at different wavelengths ranging from $\lambda_0 = 1130$ nm to 1180 nm.

C.7: Angularly dependent transmission of the large-scale differentiator

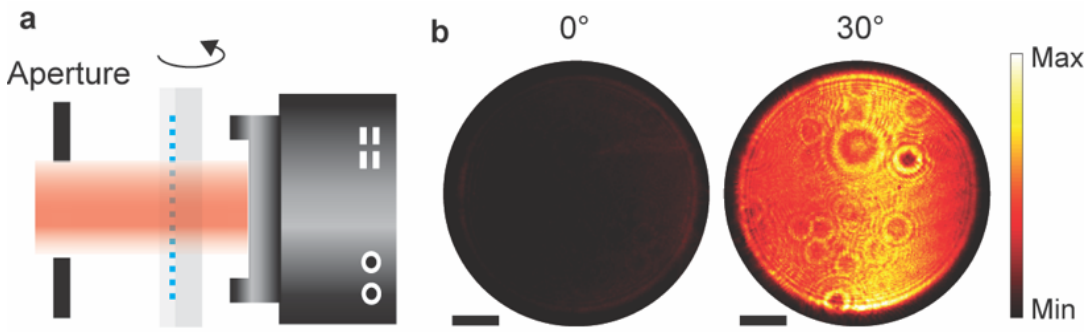

Figure C7. Transmission measurements of the large-scale differentiator. (a) Schematic of the measurement setup. The large-scale differentiator was placed directly in front of the camera for the measurements. (b) The captured intensity map when the filter is at normal and 30° incidence angle. Scale bar: 1 mm.

BIBLIOGRAPHY

[1] N. Yu *et al.*, "Light propagation with phase discontinuities: generalized laws of reflection and refraction.," *Science*, vol. 334, no. 6054, pp. 333–7, Oct. 2011.

[2] M. Khorasaninejad and F. Capasso, "Metalenses: Versatile multifunctional photonic components.," *Science*, vol. 358, no. 6367, p. eaam8100, Dec. 2017.

[3] M. Khorasaninejad, W. T. Chen, R. C. Devlin, J. Oh, A. Y. Zhu, and F. Capasso, "Metalenses at visible wavelengths: Diffraction-limited focusing and subwavelength resolution imaging.," *Science*, vol. 352, no. 6290, pp. 1190–4, Jun. 2016.

[4] A. Arbabi, Y. Horie, A. J. Ball, M. Bagheri, and A. Faraon, "Subwavelength-thick lenses with high numerical apertures and large efficiency based on high-contrast transmitarrays.," *Nat. Commun.*, vol. 6, no. 1, p. 7069, May 2015.

[5] N. Yu, F. Aieta, P. Genevet, M. A. Kats, Z. Gaburro, and F. Capasso, "A Broadband, Background-Free Quarter-Wave Plate Based on Plasmonic Metasurfaces," *Nano Lett.*, vol. 12, no. 12, pp. 6328–6333, Dec. 2012.

[6] S. Kruk, B. Hopkins, I. I. Kravchenko, A. Miroshnichenko, D. N. Neshev, and Y. S. Kivshar, "Invited Article: Broadband highly efficient dielectric metadevices for polarization control," *APL Photonics*, vol. 1, no. 3, p. 030801, Jun. 2016.

[7] M. Khorasaninejad, W. Zhu, and K. B. Crozier, "Efficient polarization beam splitter pixels based on a dielectric metasurface," *Optica*, vol. 2, no. 4, p. 376, Apr. 2015.

[8] L. Liu *et al.*, "Broadband metasurfaces with simultaneous control of phase and amplitude," *Adv. Mater.*, vol. 26, no. 29, pp. 5031–5036, 2014.

[9] S. M. Kamali, E. Arbabi, A. Arbabi, Y. Horie, M. Faraji-Dana, and A. Faraon, "Angle-multiplexed metasurfaces: encoding independent wavefronts in a single metasurface under different illumination angles," *Phys. Rev. X*, vol. 7, no. 4, pp. 1–9, Nov. 2017.

[10] S. M. Kamali, A. Arbabi, E. Arbabi, Y. Horie, and A. Faraon, "Decoupling optical function and geometrical form using conformal flexible dielectric metasurfaces," *Nat. Commun.*, vol. 7, p. 11618, May 2016.

[11] A. Arbabi, Y. Horie, M. Bagheri, and A. Faraon, "Dielectric Metasurfaces for Complete Control of Phase and Polarization with Subwavelength Spatial Resolution and High Transmission," *Nat. Nanotechnol.*, vol. 10, no. 11, pp. 937–943, Nov. 2014.

[12] M. Khorasaninejad *et al.*, "Polarization-Insensitive Metalenses at Visible Wavelengths," *Nano Lett.*, vol. 16, no. 11, pp. 7229–7234, Nov. 2016.

[13] W. T. Chen *et al.*, "Broadband Achromatic Metasurface-Refractive Optics," *Nano Lett.*, vol. 18, no. 12, pp. 7801–7808, 2018.

[14] A. Zhan, S. Colburn, R. Trivedi, T. K. Fryett, C. M. Dodson, and A. Majumdar, "Low-Contrast Dielectric Metasurface Optics," *ACS Photonics*, vol. 3, no. 2, pp. 209–214, Feb. 2016.

[15] Z. Bin Fan *et al.*, "Silicon Nitride Metalenses for Close-to-One Numerical Aperture and Wide-Angle Visible Imaging," *Phys. Rev. Appl.*, vol. 10, no. 1, p. 014005, Jul. 2018.

[16] C. Pfeiffer, N. K. Emani, A. M. Shaltout, A. Boltasseva, V. M. Shalaev, and A. Grbic, "Efficient light bending with isotropic metamaterial Huygens' surfaces," *Nano Lett.*, vol. 14, no. 5, pp. 2491–2497, May 2014.

[17] M. Decker *et al.*, "High-Efficiency Dielectric Huygens' Surfaces," *Adv. Opt. Mater.*, vol. 3, no. 6, pp. 813–820, Aug. 2015.

[18] M. I. Shalaev, J. Sun, A. Tsukernik, A. Pandey, K. Nikolskiy, and N. M. Litchinitser, "High-Efficiency All-Dielectric Metasurfaces for Ultracompact Beam Manipulation in Transmission Mode," *Nano Lett.*, vol. 15, no. 9, pp. 6261–6266, 2015.

[19] K. E. Chong *et al.*, "Efficient Polarization-Insensitive Complex Wavefront Control Using Huygens' Metasurfaces Based on Dielectric Resonant Meta-atoms," *ACS Photonics*, vol. 3,

no. 4, pp. 514–519, Apr. 2016.

[20] A. Howes, W. Wang, I. Kravchenko, and J. Valentine, “Dynamic transmission control based on all-dielectric Huygens metasurfaces,” *Optica*, vol. 5, no. 7, p. 787, Jul. 2018.

[21] S. Q. Li, X. Xu, R. M. Veetil, V. Valuckas, R. Paniagua-Domínguez, and A. I. Kuznetsov, “Phase-only transmissive spatial light modulator based on tunable dielectric metasurface,” *Science (80-.).*, vol. 364, no. 6445, pp. 1087–1090, Jun. 2019.

[22] P. Lalanne, S. Astilean, P. Chavel, E. Cambril, and H. Launois, “Blazed binary subwavelength gratings with efficiencies larger than those of conventional échelette gratings,” *Opt. Lett.*, vol. 23, no. 14, p. 1081, 1998.

[23] P. Lalanne, S. Astilean, P. Chavel, E. Cambril, and H. Launois, “Design and fabrication of blazed binary diffractive elements with sampling periods smaller than the structural cutoff,” *J. Opt. Soc. Am. A*, vol. 16, no. 5, p. 1143, May 1999.

[24] P. Lalanne, “Waveguiding in blazed-binary diffractive elements,” *J. Opt. Soc. Am. A*, vol. 16, no. 10, p. 2517, 1999.

[25] S. M. Kamali, E. Arbabi, A. Arbabi, Y. Horie, and A. Faraon, “Highly tunable elastic dielectric metasurface lenses,” *Laser Photonics Rev.*, vol. 10, no. 6, pp. 1002–1008, 2016.

[26] E. Arbabi, A. Arbabi, S. M. Kamali, Y. Horie, and A. Faraon, “Multiwavelength polarization insensitive lenses based on dielectric metasurfaces with meta-molecules,” *Optica*, vol. 3, no. 6, p. 628, Jan. 2016.

[27] A. Arbabi, E. Arbabi, S. M. Kamali, Y. Horie, S. Han, and A. Faraon, “Miniature optical planar camera based on a wide-angle metasurface doublet corrected for monochromatic aberrations,” *Nat. Commun.*, vol. 7, pp. 1–9, 2016.

[28] B. Groever, W. T. Chen, and F. Capasso, “Meta-lens doublet in the visible region,” *Nano Lett.*, vol. 17, no. 8, pp. 4902–4907, 2017.

[29] W. T. Chen, A. Y. Zhu, J. Sisler, Z. Bharwani, and F. Capasso, "A broadband achromatic polarization-insensitive metalens consisting of anisotropic nanostructures," *Nat. Commun.*, vol. 10, no. 1, 2019.

[30] W. T. Chen *et al.*, "A broadband achromatic metalens for focusing and imaging in the visible," *Nat. Nanotechnol.*, vol. 13, no. 3, pp. 220–226, Mar. 2018.

[31] M. Khorasaninejad *et al.*, "Achromatic Metalens over 60 nm Bandwidth in the Visible and Metalens with Reverse Chromatic Dispersion," *Nano Lett.*, vol. 17, no. 3, pp. 1819–1824, 2017.

[32] E. Arbabi *et al.*, "Two-Photon Microscopy with a Double-Wavelength Metasurface Objective Lens," *Nano Lett.*, vol. 18, no. 8, pp. 4943–4948, Aug. 2018.

[33] H. Kwon, E. Arbabi, S. M. Kamali, M. S. Faraji-Dana, and A. Faraon, "Single-shot quantitative phase gradient microscopy using a system of multifunctional metasurfaces," *Nat. Photonics*, vol. 14, no. 2, pp. 109–114, 2020.

[34] H. Pahlevaninezhad *et al.*, "Nano-optic endoscope for high-resolution optical coherence tomography in vivo," *Nat. Photonics*, vol. 12, no. 9, pp. 540–547, 2018.

[35] A. She, S. Zhang, S. Shian, D. R. Clarke, and F. Capasso, "Adaptive metalenses with simultaneous electrical control of focal length, astigmatism, and shift," *Sci. Adv.*, vol. 4, no. 2, 2018.

[36] E. Arbabi, A. Arbabi, S. M. Kamali, Y. Horie, M. Faraji-Dana, and A. Faraon, "MEMS-tunable dielectric metasurface lens," *Nat. Commun.*, vol. 9, no. 1, p. 812, Dec. 2018.

[37] A. She, S. Zhang, S. Shian, D. R. Clarke, and F. Capasso, "Large area metalenses: design, characterization, and mass manufacturing," *Opt. Express*, vol. 26, no. 2, p. 1573, Jan. 2018.

[38] J. S. Park *et al.*, "All-Glass, Large Metalens at Visible Wavelength Using Deep-Ultraviolet Projection Lithography," *Nano Lett.*, vol. 19, no. 12, pp. 8673–8682, Dec. 2019.

[39] L. Huang *et al.*, “Three-dimensional optical holography using a plasmonic metasurface,” *Nat. Commun.*, vol. 4, no. 1, p. 2808, Dec. 2013.

[40] L. Wang *et al.*, “Grayscale transparent metasurface holograms,” *Optica*, vol. 3, no. 12, p. 1504, 2016.

[41] J. P. Balthasar Mueller, N. A. Rubin, R. C. Devlin, B. Groever, and F. Capasso, “Metasurface Polarization Optics: Independent Phase Control of Arbitrary Orthogonal States of Polarization,” *Phys. Rev. Lett.*, vol. 118, no. 11, 2017.

[42] M. Khorasaninejad *et al.*, “Multispectral chiral imaging with a metalens,” *Nano Lett.*, vol. 16, no. 7, pp. 4595–4600, 2016.

[43] E. Arbabi, S. M. Kamali, A. Arbabi, and A. Faraon, “Full-Stokes Imaging Polarimetry Using Dielectric Metasurfaces,” *ACS Photonics*, vol. 5, no. 8, pp. 3132–3140, 2018.

[44] N. A. Rubin, G. D’Aversa, P. Chevalier, Z. Shi, W. T. Chen, and F. Capasso, “Matrix Fourier optics enables a compact full-Stokes polarization camera,” *Science (80-.).*, vol. 364, no. 6448, 2019.

[45] M. Jang *et al.*, “Wavefront shaping with disorder-engineered metasurfaces,” *Nat. Photonics*, vol. 12, no. 2, pp. 84–90, 2018.

[46] B. Wang *et al.*, “Visible-Frequency Dielectric Metasurfaces for Multiwavelength Achromatic and Highly Dispersive Holograms,” *Nano Lett.*, vol. 16, no. 8, pp. 5235–5240, 2016.

[47] F. Aieta, M. A. Kats, P. Genevet, and F. Capasso, “Multiwavelength achromatic metasurfaces by dispersive phase compensation,” *Science (80-.).*, vol. 347, no. 6228, pp. 1342–1345, Mar. 2015.

[48] Y. W. Huang *et al.*, “Aluminum plasmonic multicolor meta-Hologram,” *Nano Lett.*, vol. 15, no. 5, pp. 3122–3127, 2015.

[49] W. Zhao, B. Liu, H. Jiang, J. Song, Y. Pei, and Y. Jiang, "Full-color hologram using spatial multiplexing of dielectric metasurface," *Opt. Lett.*, vol. 41, no. 1, p. 147, 2016.

[50] D. Lin *et al.*, "Photonic Multitasking Interleaved Si Nanoantenna Phased Array," *Nano Lett.*, vol. 16, no. 12, pp. 7671–7676, 2016.

[51] D. Sell, J. Yang, S. Doshay, and J. A. Fan, "Periodic Dielectric Metasurfaces with High-Efficiency, Multiwavelength Functionalities," *Adv. Opt. Mater.*, vol. 5, no. 23, p. 1700645, Dec. 2017.

[52] E. Arbabi, A. Arbabi, S. M. Kamali, Y. Horie, and A. Faraon, "Multiwavelength polarization-insensitive lenses based on dielectric metasurfaces with," *Optica*, vol. 3, no. 6, pp. 628–633, 2016.

[53] O. Avayu, E. Almeida, Y. Prior, and T. Ellenbogen, "Composite functional metasurfaces for multispectral achromatic optics," *Nat. Commun.*, vol. 8, pp. 1–7, 2017.

[54] J. Ding, S. An, B. Zheng, and H. Zhang, "Multiwavelength Metasurfaces Based on Single-Layer Dual-Wavelength Meta-Atoms: Toward Complete Phase and Amplitude Modulations at Two Wavelengths," *Adv. Opt. Mater.*, vol. 5, no. 10, pp. 1–8, 2017.

[55] B. Wang *et al.*, "Polarization-controlled color-tunable holograms with dielectric metasurfaces," *Optica*, vol. 4, no. 11, p. 1368, 2017.

[56] W. Wan, J. Gao, and X. Yang, "Full-Color Plasmonic Metasurface Holograms," *ACS Nano*, vol. 10, no. 12, pp. 10671–10680, 2016.

[57] X. Zhang *et al.*, "All-Dielectric Meta-Holograms with Holographic Images Transforming Longitudinally," *ACS Photonics*, vol. 5, no. 2, pp. 599–606, 2018.

[58] J. Deng *et al.*, "Spatial Frequency Multiplexed Meta-Holography and Meta-Nanoprinting," *ACS Nano*, vol. 13, no. 8, pp. 9237–9246, 2019.

[59] X. Zang *et al.*, "Polarization Encoded Color Image Embedded in a Dielectric Metasurface,"

Adv. Mater., vol. 30, no. 21, p. 1707499, May 2018.

[60] E. Heydari, J. R. Sperling, S. L. Neale, and A. W. Clark, "Plasmonic Color Filters as Dual-State Nanopixels for High-Density Microimage Encoding," *Adv. Funct. Mater.*, vol. 27, no. 35, pp. 1–6, 2017.

[61] A. Tittl *et al.*, "Imaging-based molecular barcoding with pixelated dielectric metasurfaces," *Science (80-.).*, vol. 360, no. 6393, pp. 1105–1109, Jun. 2018.

[62] A. Leitis *et al.*, "Angle-multiplexed all-dielectric metasurfaces for broadband molecular fingerprint retrieval," *Sci. Adv.*, vol. 5, no. 5, p. eaaw2871, May 2019.

[63] D. Sell, J. Yang, S. Doshay, R. Yang, and J. A. Fan, "Large-Angle, Multifunctional Metagratings Based on Freeform Multimode Geometries," *Nano Lett.*, vol. 17, no. 6, pp. 3752–3757, 2017.

[64] J. S. Jensen and O. Sigmund, "Topology optimization for nano-photonics," *Laser Photonics Rev.*, vol. 5, no. 2, pp. 308–321, 2011.

[65] C. M. Lalau-Keraly, S. Bhargava, O. D. Miller, and E. Yablonovitch, "Adjoint shape optimization applied to electromagnetic design," *Opt. Express*, vol. 21, no. 18, p. 21693, 2013.

[66] Z. Liu, D. Zhu, S. P. Rodrigues, K. T. Lee, and W. Cai, "Generative Model for the Inverse Design of Metasurfaces," *Nano Lett.*, vol. 18, no. 10, pp. 6570–6576, 2018.

[67] Z. Lin, B. Groever, F. Capasso, A. W. Rodriguez, and M. Lončar, "Topology-Optimized Multilayered Metaoptics," *Phys. Rev. Appl.*, vol. 9, no. 4, p. 044030, Apr. 2018.

[68] T. Phan *et al.*, "High-efficiency, large-area, topology-optimized metasurfaces," *Light Sci. Appl.*, vol. 8, no. 1, p. 48, Dec. 2019.

[69] J. Lu and J. Vuckovic, "Nanophotonic Computational Design," vol. 21, no. 11, pp. 7748–7759, 2013.

[70] A. L. A. N. Z. Han, T. A. K. F. Ryett, and S. H. C. Olburn, “Inverse design of optical elements based on arrays of dielectric spheres,” vol. 57, no. 6, 2018.

[71] S. Molesky, Z. Lin, A. Y. Piggott, W. Jin, J. Vucković, and A. W. Rodriguez, “Inverse design in nanophotonics,” *Nature Photonics*, vol. 12, no. 11. Nature Publishing Group, pp. 659–670, 26-Nov-2018.

[72] A. S. Backer, “Computational inverse design for cascaded systems of metasurface optics.”

[73] F. Callewaert, V. Velev, P. Kumar, A. V. Sahakian, and K. Aydin, “Inverse-Designed Broadband All-Dielectric Electromagnetic Metadevices,” *Sci. Rep.*, vol. 8, no. 1, pp. 1–8, 2018.

[74] J. Lu and J. Vučković, “Nanophotonic computational design,” *Opt. Express*, vol. 21, no. 11, p. 13351, 2013.

[75] G. Kim, J. A. Domínguez-Caballero, and R. Menon, “Design and analysis of multi-wavelength diffractive optics,” *Opt. Express*, vol. 20, no. 3, p. 2814, 2012.

[76] B. Shen, P. Wang, R. Polson, and R. Menon, “Ultra-high-efficiency metamaterial polarizer,” *Optica*, vol. 1, no. 5, p. 356, 2014.

[77] B. Shen, P. Wang, R. Polson, and R. Menon, “An integrated-nanophotonics polarization beamsplitter with 2.4×2.4μm 2 footprint,” *Nat. Photonics*, vol. 9, no. 6, pp. 378–382, 2015.

[78] A. S. Backer, “Computational inverse design for cascaded systems of metasurface optics,” *Opt. Express*, vol. 27, no. 21, p. 30308, Jun. 2019.

[79] Y. Elesin, B. S. Lazarov, J. S. Jensen, and O. Sigmund, “Design of robust and efficient photonic switches using topology optimization,” *Photonics Nanostructures - Fundam. Appl.*, vol. 10, no. 1, pp. 153–165, Jan. 2012.

[80] Z. Lin, M. Lončar, and A. W. Rodriguez, “Topology optimization of multi-track ring resonators and 2D microcavities for nonlinear frequency conversion,” *Opt. Lett.*, vol. 42,

no. 14, p. 2818, Jul. 2017.

[81] K. Y. Yang *et al.*, "Inverse-designed photonic circuits for fully passive, bias-free Kerr-based nonreciprocal transmission and routing," May 2019.

[82] A. Regensburger, C. Bersch, M. A. Miri, G. Onishchukov, D. N. Christodoulides, and U. Peschel, "Parity-time synthetic photonic lattices," *Nature*, vol. 488, no. 7410, pp. 167–171, Aug. 2012.

[83] L. Lu, J. D. Joannopoulos, and M. Soljačić, "Topological photonics," *Nature Photonics*, vol. 8, no. 11. Nature Publishing Group, pp. 821–829, 05-Nov-2014.

[84] H. Men, K. Y. K. Lee, R. M. Freund, J. Peraire, and S. G. Johnson, "Robust topology optimization of three-dimensional photonic-crystal band-gap structures," *Opt. Express*, vol. 22, no. 19, p. 22632, Sep. 2014.

[85] Y. E. Lee, O. D. Miller, M. T. Homer Reid, S. G. Johnson, and N. X. Fang, "Computational inverse design of non-intuitive illumination patterns to maximize optical force or torque," *Opt. Express*, vol. 25, no. 6, p. 6757, Mar. 2017.

[86] O. D. Miller, S. G. Johnson, and A. W. Rodriguez, "Shape-Independent Limits to Near-Field Radiative Heat Transfer," *Phys. Rev. Lett.*, vol. 115, no. 20, p. 204302, Nov. 2015.

[87] W. Jin, R. Messina, and A. W. Rodriguez, "Overcoming limits to near-field radiative heat transfer in uniform planar media through multilayer optimization," *Opt. Express*, vol. 25, no. 13, p. 14746, Jun. 2017.

[88] S. Bhargava and E. Yablonovitch, "Lowering HAMR near-field transducer temperature via inverse electromagnetic design," *IEEE Trans. Magn.*, vol. 51, no. 4, Apr. 2015.

[89] A. Silva, F. Monticone, G. Castaldi, V. Galdi, A. Alù, and N. Engheta, "Performing mathematical operations with metamaterials," *Science (80-.).*, vol. 343, no. 6167, pp. 160–163, 2014.

[90] T. Zhu *et al.*, “Plasmonic computing of spatial differentiation,” *Nat. Commun.*, vol. 8, no. May, pp. 1–6, 2017.

[91] D. A. Bykov, L. L. Doskolovich, E. A. Bezus, and V. A. Soifer, “Optical computation of the Laplace operator using phase-shifted Bragg grating,” *Opt. Express*, vol. 22, no. 21, p. 25084, 2014.

[92] C. Guo, M. Xiao, M. Minkov, Y. Shi, and S. Fan, “Photonic crystal slab Laplace operator for image differentiation,” *Optica*, vol. 5, no. 3, p. 251, 2018.

[93] A. Cordaro, H. Kwon, D. Sounas, A. F. Koenderink, A. Alù, and A. Polman, “High-Index Dielectric Metasurfaces Performing Mathematical Operations,” *Nano Lett.*, vol. 19, no. 12, pp. 8418–8423, Mar. 2019.

[94] E. Arbabi, A. Arbabi, S. M. Kamali, Y. Horie, and A. Faraon, “Multiwavelength metasurfaces through spatial multiplexing,” *Sci. Rep.*, vol. 6, pp. 1–8, 2016.

[95] P. Moitra, Y. Yang, Z. Anderson, I. I. Kravchenko, D. P. Briggs, and J. Valentine, “Realization of an all-dielectric zero-index optical metamaterial,” *Nat. Photonics*, vol. 7, no. 10, pp. 791–795, 2013.

[96] A. Arbabi, E. Arbabi, Y. Horie, S. M. Kamali, and A. Faraon, “Planar metasurface retroreflector,” *Nat. Photonics*, vol. 11, no. 7, pp. 415–420, 2017.

[97] E. Arbabi, A. Arbabi, S. M. Kamali, Y. Horie, and A. Faraon, “Controlling the sign of chromatic dispersion in diffractive optics with dielectric metasurfaces,” *Optica*, vol. 4, no. 6, p. 625, Jun. 2017.

[98] S. Wang *et al.*, “A broadband achromatic metalens in the visible,” *Nat. Nanotechnol.*, vol. 13, no. 3, pp. 227–232, 2018.

[99] E. Sugawara and H. Nikaido, “Properties of AdeABC and AdeIJK efflux systems of Acinetobacter baumannii compared with those of the AcrAB-TolC system of Escherichia coli.,” *Antimicrob. Agents Chemother.*, vol. 58, no. 12, pp. 7250–7, Dec. 2014.

[100] M. Khorasaninejad *et al.*, "Achromatic Metasurface Lens at Telecommunication Wavelengths," *Nano Lett.*, vol. 15, no. 8, pp. 5358–5362, 2015.

[101] A. F. Oskooi, D. Roundy, M. Ibanescu, P. Bermel, J. D. Joannopoulos, and S. G. Johnson, "Meep: A flexible free-software package for electromagnetic simulations by the FDTD method," *Comput. Phys. Commun.*, vol. 181, no. 3, pp. 687–702, 2010.

[102] B. Han Chen *et al.*, "GaN Metalens for Pixel-Level Full-Color Routing at Visible Light," *Nano Lett*, vol. 17, no. 10, pp. 6345–6352, 2017.

[103] C. Pfeiffer and A. Grbic, "Bianisotropic metasurfaces for optimal polarization control: Analysis and synthesis," *Phys. Rev. Appl.*, vol. 2, no. 4, pp. 1–11, 2014.

[104] C. Pfeiffer, C. Zhang, V. Ray, L. J. Guo, and A. Grbic, "High performance bianisotropic metasurfaces: Asymmetric transmission of light," *Phys. Rev. Lett.*, vol. 113, no. 2, pp. 1–5, 2014.

[105] Y. Zhou, I. I. Kravchenko, H. Wang, J. R. Nolen, G. Gu, and J. Valentine, "Multilayer Noninteracting Dielectric Metasurfaces for Multiwavelength Metaoptics," *Nano Lett.*, vol. 18, no. 12, pp. 7529–7537, Dec. 2018.

[106] A. Overvig, S. Shrestha, C. Zheng, and N. Yu, "High-Efficiency Amplitude-Phase Modulation Holograms Based on Dielectric Metasurfaces," vol. 1, no. c, pp. 4–5, 2017.

[107] X. Song *et al.*, "Selective Diffraction with Complex Amplitude Modulation by Dielectric Metasurfaces," *Adv. Opt. Mater.*, vol. 6, no. 4, pp. 1–8, 2018.

[108] G. Y. Lee *et al.*, "Complete amplitude and phase control of light using broadband holographic metasurfaces," *Nanoscale*, vol. 10, no. 9, pp. 4237–4245, 2018.

[109] R. W. Gerchberg and W. O. Saxton, "A Practical Algorithm for the Determination of Phase from Image and Diffraction Plane Pictures," *Optik (Stuttg).*, vol. 2, no. 352, pp. 237–246, 1969.

[110] M. Decker *et al.*, "High-efficiency light-wave control with all-dielectric optical Huygens' metasurfaces," 2014.

[111] P. Moitra, B. A. Slovick, Z. Gang Yu, S. Krishnamurthy, and J. Valentine, "Experimental demonstration of a broadband all-dielectric metamaterial perfect reflector," *Appl. Phys. Lett.*, vol. 104, no. 17, p. 171102, Apr. 2014.

[112] B. A. Slovick *et al.*, "Metasurface polarization splitter," *Philos. Trans. R. Soc. A Math. Phys. Eng. Sci.*, vol. 375, no. 2090, pp. 1–9, 2017.

[113] A. Kovalskiy *et al.*, "Chalcogenide glass e-beam and photoresists for ultrathin grayscale patterning," *J. Micro/Nanolithography, MEMS, MOEMS*, vol. 8, no. 4, p. 043012, Oct. 2009.

[114] E.-B. Kley, M. Cumme, L.-C. Wittig, and C. Wu, "Adapting existing e-beam writers to write HEBS-glass gray-scale masks," in *Diffractive and Holographic Technologies, Systems, and Spatial Light Modulators VI*, 1999, vol. 3633, pp. 35–45.

[115] Y. Zhou, H. Zheng, I. I. Kravchenko, and J. Valentine, "Flat optics for image differentiation," *Nat. Photonics*, pp. 1–8, 2020.

[116] D. Ma, "Theory of edge detection," 1980.

[117] J. CANNY, "A Computational Approach to Edge Detection," in *Readings in Computer Vision*, Elsevier, 1987, pp. 184–203.

[118] M. Mainberger and J. Weickert, "Edge-Based Image Compression with Homogeneous Diffusion," Springer, Berlin, Heidelberg, 2009, pp. 476–483.

[119] H.-S. Hsu and W.-H. Tsai, "Moment-preserving edge detection and its application to image data compression," *Opt. Eng.*, vol. 32, no. 7, p. 1596, 1993.

[120] T. Brosnan and D.-W. Sun, "Improving quality inspection of food products by computer vision—a review," *J. Food Eng.*, vol. 61, no. 1, pp. 3–16, Jan. 2004.

[121] S. Fürhapter, A. Jesacher, S. Bernet, and M. Ritsch-Marte, "Spiral phase contrast imaging in microscopy," *Opt. Express*, vol. 13, no. 3, p. 689, 2005.

[122] T. Gebäck and P. Koumoutsakos, "Edge detection in microscopy images using curvelets," *BMC Bioinformatics*, vol. 10, no. 1, p. 75, Dec. 2009.

[123] R. A. Cardullo, "Fundamentals of Image Processing in Light Microscopy," vol. 72, pp. 217–242, 2004.

[124] R. M. Haralick and L. G. Shapiro, "Computer and Robot Vision," *IEEE Robot. Autom. Mag.*, vol. 1, pp. 28–48, 1991.

[125] D. R. Solli and B. Jalali, "Analog optical computing," *Nat. Photonics*, vol. 9, no. 11, pp. 704–706, Nov. 2015.

[126] N. Yu *et al.*, "Light propagation with phase discontinuities: generalized laws of reflection and refraction.," *Science*, vol. 334, no. 6054, pp. 333–7, Oct. 2011.

[127] J. D. Joannopoulos, P. R. Villeneuve, and S. Fan, "Photonic crystals putting a new twist on light," *Nature*, vol. 386, no. 6621, pp. 143–149, 1997.

[128] A. Alù and N. Engheta, "Performing Methematical Operations with Metamaterials," *Science (80-.).*, no. January, pp. 160–164, 2014.

[129] H. Kwon, D. Sounas, A. Cordaro, A. Polman, and A. Alù, "Nonlocal Metasurfaces for Optical Signal Processing," *Phys. Rev. Lett.*, vol. 121, no. 17, p. 173004, 2018.

[130] T. Zhu *et al.*, "Generalized Spatial Differentiation from the Spin Hall Effect of Light and Its Application in Image Processing of Edge Detection," *Phys. Rev. Appl.*, vol. 11, no. 3, p. 1, 2019.

[131] J. Zhou *et al.*, "Optical edge detection based on high-efficiency dielectric metasurface," *Proc. Natl. Acad. Sci.*, vol. 116, no. 23, pp. 11137–11140, Jun. 2019.

[132] R. N. Bracewell, “The Fourier Transform and applications,” *McGraw Hill*, pp. 1–10, 2000.

[133] V. I. Krivenkov, “Guided modes in photonic crystal fibers,” *Dokl. Phys.*, vol. 48, no. 8, pp. 414–417, 2003.

[134] S. Fan and J. D. Joannopoulos, “Analysis of guided resonances in photonic crystal slabs,” *Phys. Rev. B - Condens. Matter Mater. Phys.*, vol. 65, no. 23, pp. 1–8, Jun. 2002.

[135] W. Zhou *et al.*, “Progress in 2D photonic crystal Fano resonance photonics,” *Prog. Quantum Electron.*, vol. 38, no. 1, pp. 1–74, 2014.

[136] Z. S. Liu, S. Tibuleac, D. Shin, P. P. Young, and R. Magnusson, “High-efficiency guided-mode resonance filter,” *Opt. Lett.*, vol. 23, no. 19, p. 1556, 1998.

[137] W. Suh, M. F. Yanik, O. Solgaard, and S. Fan, “Displacement-sensitive photonic crystal structures based on guided resonance in photonic crystal slabs,” *Appl. Phys. Lett.*, vol. 82, no. 13, pp. 1999–2001, 2003.

[138] J. N. Winn, Y. Fink, S. Fan, and J. D. Joannopoulos, “Omnidirectional reflection from a one-dimensional photonic crystal,” *Opt. Lett.*, vol. 23, no. 20, p. 1573, 1998.

[139] C. W. Hsu, B. Zhen, A. D. Stone, J. D. Joannopoulos, and M. Soljačić, “Bound States in the Continuum.”

[140] L. Xu *et al.*, “Dynamic Nonlinear Image Tuning through Magnetic Dipole Quasi-BIC Ultrathin Resonators,” *Adv. Sci.*, vol. 6, no. 15, p. 1802119, May 2019.

[141] J. Lee *et al.*, “Observation and differentiation of unique high-Q optical resonances near zero wave vector in macroscopic photonic crystal slabs,” *Phys. Rev. Lett.*, vol. 109, no. 6, Aug. 2012.

[142] P. Moitra *et al.*, “Large-Scale All-Dielectric Metamaterial Perfect Reflectors,” *ACS Photonics*, vol. 2, no. 6, pp. 692–698, Jun. 2015.

[143] Y. Zhou, I. I. Kravchenko, H. Wang, H. Zheng, G. Gu, and J. Valentine, "Multifunctional metaoptics based on bilayer metasurfaces," *Light Sci. Appl. 2019 81*, vol. 8, no. 1, pp. 1–9, Sep. 2019.

[144] V. Liu and S. Fan, "S4: A free electromagnetic solver for layered periodic structures," *Comput. Phys. Commun.*, vol. 183, no. 10, pp. 2233–2244, 2012.

[145] A. Castellanos-Gomez *et al.*, "Deterministic transfer of two-dimensional materials by all-dry viscoelastic stamping," *2D Mater.*, vol. 1, no. 1, p. 011002, Apr. 2014.